


12-5-2018

# Turbulent and Electromagnetic Signature of Small- and Fine-scale Biological and Oceanographic Processes

Cayla Whitney Dean  
cd821@nova.edu

Follow this and additional works at: [https://nsuworks.nova.edu/occ\\_stuetd](https://nsuworks.nova.edu/occ_stuetd)

 Part of the [Marine Biology Commons](#), and the [Oceanography and Atmospheric Sciences and Meteorology Commons](#)

## Share Feedback About This Item

---

### NSUWorks Citation

Cayla Whitney Dean. 2018. *Turbulent and Electromagnetic Signature of Small- and Fine-scale Biological and Oceanographic Processes*. Doctoral dissertation. Nova Southeastern University. Retrieved from NSUWorks, . (492)  
[https://nsuworks.nova.edu/occ\\_stuetd/492](https://nsuworks.nova.edu/occ_stuetd/492).

This Dissertation is brought to you by the HCNSO Student Work at NSUWorks. It has been accepted for inclusion in HCNSO Student Theses and Dissertations by an authorized administrator of NSUWorks. For more information, please contact [nsuworks@nova.edu](mailto:nsuworks@nova.edu).

---

Dissertation of  
Cayla Whitney Dean

Submitted in Partial Fulfillment of the Requirements for the Degree of

Doctorate of Philosophy  
Ph.D. Oceanography/Marine Biology

Nova Southeastern University  
Halmos College of Natural Sciences and Oceanography

December 2018

Approved:  
Dissertation Committee

Major Professor: Alexander Soloviev, Ph.D.

Committee Member: Tracey Sutton, Ph.D.

Committee Member: John Holmes, Ph.D.

Committee Member: Tamay Ozgokmen, Ph.D.

HALMOS COLLEGE OF NATURAL SCIENCES AND OCEANOGRAPHY

TURBULENT AND ELECTROMAGNETIC SIGNATURE OF SMALL-  
AND FINE-SCALE BIOLOGICAL AND OCEANOGRAPHIC  
PROCESSES

By

Cayla Whitney Dean

Submitted to the Faculty of  
Halmos College of Natural Sciences and Oceanography  
in partial fulfillment of the requirements for  
the degree of Doctorate of Philosophy

Nova Southeastern University

December 2018

## Abstract

Small- and fine-scale biological and oceanographic processes may have a measurable electromagnetic signature. These types of processes inherently involve turbulence and three-dimensional dynamics. Traditional models of the electromagnetic signature of oceanographic processes are of an analytical nature, do not account for three-dimensional boundary layer dynamics or turbulence, self-inductance, and may not describe the variety of the environmental conditions occurring in the ocean. In order to address this problem, I have implemented magnetohydrodynamic (MHD) computational fluid dynamics (CFD) tools, which has allowed for the evaluation of the electromagnetic signature of a number of small- and fine-scale biological and oceanographic processes in the ocean. The suite of computational tools has included the commercial models *ANSYS Fluent*, coupled with the MHD module, and *ANSYS Maxwell*. These computational tools have been well-established in fluid and electromagnetic engineering. The application of CFD and MHD tools in oceanography is new but is undergoing rapid development. In this work, substantial effort was made toward the CFD, MHD, and magnetostatic model verification and identification of model limitations. Verifications of the CFD, MHD, and magnetostatic models were conducted by successfully comparing their results with the field measurements and laboratory experiments.

Comparison with the traditional (analytical) models for surface and internal waves, has revealed their limitations related to bottom boundary layer physics, effect of self-inductance, and, to a lesser extent, the magnetic permeability difference at the air-sea interface. These limitations become important for shallow water internal waves. As a result, the traditional models significantly overestimate the magnetic signature of internal waves observed at the Electromagnetic Observatory.

After model verification with the field and laboratory data, the computational models were then applied to evaluate the magnetic signature of diel vertical migration (DVM) of zooplankton, surface waves, internal wave solitons, freshwater lens spreading, and Langmuir circulation. The quantitative estimates have been made for typical environmental conditions. In other environmental conditions, their magnetic signature may be somewhat different. The suite of computational models developed in this dissertation work allows for the estimation of the magnetic signature of fine- and small-scale oceanographic processes in virtually any environmental conditions (*e.g.*, in oil emulsions). I anticipate the result of this study will have Naval, environmental, and oil exploration applications.

Keywords: computational fluid dynamics, magnetohydrodynamics, turbulence, electromagnetics, diel vertical migration, internal wave, surface wave

## TABLE OF CONTENTS

1. Introduction .....	11
1.1. Diel vertical migration .....	12
1.2. Surface and internal waves .....	18
1.3. Freshwater lenses .....	22
1.4. Coherent structures .....	23
1.5. Magnetic signature of small-scale oceanographic processes .....	26
1.6. Goal .....	28
2. Numerical models .....	29
2.1. Computational fluid dynamics model .....	29
2.2. Magnetohydrodynamic model .....	31
2.3. Magnetostatic model .....	34
3. Model verifications .....	36
3.1. Comparison of magnetohydrodynamic model with known analytical solutions of surface waves .....	36
3.2. Comparison of magnetohydrodynamic model with known analytical solutions of internal waves .....	41
3.3. Boundary effects .....	45
3.4. Model verification in oceanic conditions .....	48
3.5. Verifications of the magnetohydrodynamic and magnetostatic models with laboratory experiment .....	59
3.6. Summary .....	66
4. Magnetic signature of DVM .....	67
4.1. Modeling of DVM in the Straits of Florida .....	67
4.2. Modeling of DVM in Saanich Inlet .....	75
4.3. Modeling of DVM in the Gulf of Mexico .....	79
4.4. Modeling of magnetic signature of DVM .....	81
5. Comparison of magnetic signature of DVM to magnetic signature of other fine-scale oceanographic processes .....	83
5.1. Idealized surface waves .....	83
5.2. Internal wave soliton breaking on the continental slope .....	85

5.3. Freshwater lens spreading.....	87
5.4. Langmuir circulation and ramp-like structures.....	89
5.5. Comparison of magnetic signature of different processes.....	92
6. Conclusions .....	93
7. Acknowledgements .....	96
8. References .....	97
9. Appendix .....	104

## List of Figures

<b>Figure 1.</b> Acoustic backscatter from bottom-mounted ADCP for a subset of an 11-month data set in the Straits of Florida. (After Dean et al. 2016a.).....	13
<b>Figure 2.</b> Acoustic backscatter from bottom-mounted ADCP for a subset of an 11-month data set with sunrise times indicated by a solid white line, sunset by a dashed white line, new moon by a solid black line, and full moon by a dashed black line. Near surface bins have been removed due to multiple reflections. (After Dean et al. 2016a.).....	14
<b>Figure 3.</b> Flow visualization from particle image velocimetry experiment showing zooplankton swimming creates turbulent motions on scales larger than individual organisms. (After Wilhelmus and Dabiri 2014.).....	15
<b>Figure 4.</b> Turbulence signature of DVM of krill in Saanich Inlet. (Top) Acoustic backscatter data from a 200-kHz echosounder reveals vertical migration of the backscatter layer. (Bottom) Profiles of the vertical microstructure profiler. Red indicates the increase of dissipation rate of turbulent kinetic energy over background levels. (After Kunze et al. 2006.).....	16
<b>Figure 5.</b> Measurement of DVM in the San Diego Trough. (Top) Migration of animals up to surface waters at sunset and down at sunrise. (Bottom) Sound associated with migration (outlined by rectangles). (After Baumann-Pickering et al. 2016.).....	17
<b>Figure 6.</b> Magnetic signature of internal waves. (Top) ANSYS Fluent simulation of internal wave. (Bottom) Naval Research Laboratory magneto-static model.....	28
<b>Figure 7.</b> Orbital velocity of 5 s period surface waves (under the assumption of a flat surface) following Weaver (1965). a) Contour plot on the center plane of the numerical domain of u and b) w velocities in the water layer applied for the initialization of the Fluent MHD model.....	39
<b>Figure 8.</b> The amplitude of velocity components calculated from the values on center plane of the numerical domain of a) u and b) w orbital velocities of a 5 s period surface waves compared to Equation (37).....	39
<b>Figure 9.</b> Magnetic signature of 5 s surface wave from the center plane of the Fluent MHD model compared to Weaver (1965) analytical solution zoomed to the depth/altitude near the air-sea interface on a linear scale.....	40
<b>Figure 10.</b> Orbital velocity of 50 m long internal wave. (under the assumption of a flat interface) following Beal and Weaver (1970) a) Contour plot on the center plane of the numerical domain of u and b) w velocities in the water layer applied for the initialization of the Fluent MHD model.....	42
<b>Figure 11.</b> The amplitude of velocity components calculated from the values on center plane of the numerical domain of a) u and b) w orbital velocities of a 50 m long internal wave compared to Equations (40) – (41).....	43

**Figure 12.** Magnetic signature of 50 m internal wave from the center plane of the compared to Beal and Weaver (1970) analytical solution. a) Zoomed into the area of the internal wave interface on a linear scale, b) zoomed near the internal wave interface on a semi log scale. The horizontal line indicates the wave interface.....44

**Figure 13.** (a) Magnetic signature of 500 m long internal wave with different seafloor and boundary conditions from the center plane of the *Fluent* MHD in comparison with Beal and Weaver’s (1970) analytical model, (b) near-bottom area shown in more detail. Note that the traditional Beal and Weaver (1970) model does not appear to be consistent with the measurements (Section 3.4).....47

**Figure 14.** (a) Magnetic signature of 1000 m long internal wave with different seafloor and boundary conditions from the center plane of the *Fluent* MHD compared to the Beal and Weaver (1970) analytical solution, (b) near-bottom area shown in more detail.....48

**Figure 15.** Example of wavenumber calculation from 30 April 2017 Node 1 ADCP northward velocity during internal wave soliton passing. The dashed lines are the initial data, the solid lines are the 7th order polynomial fit to the data. The red lines are from the time that the wave crest passed over the ADCP. The blue lines are when the trough passed over the ADCP, and the black lines are the linear interpolations used to calculate wavenumber.....50

**Figure 16.** The velocity field on 30 April 2017 during the Ambient Weather Experiment measured by NSWCCD. The top, middle, and bottom plots show northward, eastward, and vertical velocity components, respectively. All scales are in mm/s.....52

**Figure 17.** Contour plot on the center plane of the velocity field initialization of the model on 30 April from the field measurements. The domain includes air and seafloor layers. The top, middle, and bottom plots show northward, eastward, and vertical velocity components, respectively. The horizontal line indicates the air-sea interface.....53

**Figure 18.** Contour plot on the center plane of the magnitude of the modeled magnetic field fluctuations induced by the velocity field on 30 April shown in log scale. The horizontal black line indicates the air-sea interface.....53

**Figure 19.** a) Vertical current velocity on 30 April showing the passing of an internal wave soliton. b) Comparison of total magnetic field calculated by the model (5 m off the bottom in the center of the domain in the y-direction), measured during the Ambient Weather Experiment on 30 April, and the Beal and Weaver (1970) analytical model....55

**Figure 20.** The velocity field on 3 May 2017, during the Ambient Weather Experiment measured by NSWCCD. The top, middle, and bottom plots show northward, eastward, and vertical velocity components, respectively. All scales are in mm/s.....56

**Figure 21.** Contour plot on the center plane of the velocity field initialization of the model on 3 May from the field measurements. The domain includes air and seafloor



layers. The top, middle, and bottom plots show northward, eastward, and vertical velocity components, respectively.....57

**Figure 22.** Contour plot on the center plane of the magnitude of the modeled magnetic field fluctuations induced by the velocity field on 3 May shown in log scale. The horizontal black lines indicate the air-sea interface and the sea-bottom interface.....58

**Figure 23.** a) Vertical current velocity on 3 May showing the passing of an internal wave soliton. b) Comparison of total magnetic field calculated by the model (5 m off the bottom in the center of the domain in the y-direction), measured during the Ambient Weather Experiment on 3 May, and the Beal and Weaver (1970) analytical model.....58

**Figure 24.** Setup of magnetometer pair during SUSTAIN laboratory experiment to measure the magnetic signature of surface waves. 1) Two magnetometers placed on the side of the tank near the water level. 2) Sensors placed above the tank on two tripods. 3) One magnetometer on tripod and one on the glass. 4) Acoustic transducer.....60

**Figure 25.** Spectra from surface waves magnetic signature time series. The red solid line shows the spectrum from the master magnetometer, the blue line indicates the spectrum from the slave magnetometer, and the green represents the difference spectrum calculated by taking the difference between the master and slave magnetometers time series. The dashed lines indicate the confidence intervals of the spectra (After Kluge et al. 2018)...60

**Figure 26.** Center plane contour plot of initial velocity U (top) and W (bottom) produced by 0.1 m amplitude 0.56 Hz linear surface wave in SUSTAIN tank in the ANSYS *Fluent* CFD model.....61

**Figure 27.** Center plane contour plot of initial velocity U (top) and W (bottom) produced by 0.1 m amplitude 0.56 Hz non-linear surface wave in SUSTAIN tank in the ANSYS *Fluent* CFD model after 2.5 s of simulation.....62

**Figure 28.** ANSYS *Fluent* MHD simulation of laboratory experiment with (a) linear surface waves and (b) nonlinear waves. Contour plot shows magnetic field fluctuations for the z-component.....63

**Figure 29.** ANSYS *Maxwell* simulation of laboratory experiment with linear surface waves. Contour plot shows total magnetic field fluctuations.....65

**Figure 30.** Comparison of traditional model, measurements, and magnetohydrodynamic (linear and non-linear wave), and magnetostatic models of the amplitude of the magnetic signature of surface waves.....65

**Figure 31.** Straits of Florida CFD model setup: (a) numerical domain; (b) initial density profile; (c) measured current velocity profile compared to the linearized average profile initiated in the model.....68

**Figure 32.** Modeling turbulence produced by DVM of zooplankton in the Straits of Florida by injecting 10,000 positively buoyant particles with 0.01 m diameter at 100 m:

(a) particle locations at five-minute intervals; (b) contour plots of vertical velocity ( $\text{m s}^{-1}$ ); (c) average profiles of dissipation rate  $\epsilon$  ( $\text{W kg}^{-1}$ ). Background turbulence dissipation rate in the Straits of Florida is set at  $10^{-8} \text{ W kg}^{-1}$  following measurements by Gregg et al. (1999). In the upper few meters, dissipation rate exceeded  $10^{-8} \text{ W kg}^{-1}$  due to surface wind stress and has been removed.....69

**Figure 33.** Same as in Fig. 32, but by injecting 5000 particles  $\text{m}^{-3}$ .....70

**Figure 34.** Same as in Fig. 32, but by injecting 1000 particles  $\text{m}^{-3}$ .....71

**Figure 35.** Average ADCP northward current velocity profiles in full 11-month data set during migration compared to before migration from ADCP. The velocity profile during migration was calculated as an hour-long average around sunrise/sunset and the before migration velocity profile was calculated as an hour-long average, three hours prior to and after sunrise/sunset. a) Average velocity profile. b) Difference between during migration and  $\pm 3$  hours using a 67% confidence interval (dashed lines).....72

**Figure 36.** Average model current velocity in Straits of Florida in extreme concentration case ( $10,000 \text{ org/m}^3$ ). a) Average current velocity profiles in particles and no particles cases. b) No particles case at 25 minutes after injection minus particles case at same time. Particles representing zooplankton were released at 100 m depth.....73

**Figure 37.** Average model current velocity in Straits of Florida in case with low concentration of particles ( $1000 \text{ org/m}^3$ ). a) Average current velocity profiles in particles and no particles cases. b) No particles case at 25 minutes after injection minus particles case at same time. Particles representing zooplankton were released at 100 m depth....74

**Figure 38.** Comparison of effect of DVM of zooplankton on current velocity in the model with a low concentration of particles and observations.....74

**Figure 39.** Saanich Inlet model setup: a) numerical domain; b) measured potential density profile compared to the linearized average profile initiated in the model; c) initial current velocity average profile. (After Dean et al. 2016a.).....75

**Figure 40.** Modelling the turbulence produced by DVM of zooplankton in Saanich Inlet by injecting  $10,000 \text{ m}^{-3}$  positively buoyant particles with 0.01 m diameter at 100 m: a) particle locations at five minute intervals; b) contours of vertical velocity; c) average profiles of dissipation rate  $\epsilon$  ( $\text{W kg}^{-1}$ ). Background turbulence dissipation rate in Saanich Inlet is set at  $10^{-9} \text{ W kg}^{-1}$  following measurements by Kunze et al. (2006). In the upper few meters dissipation rate exceeded  $10^{-9} \text{ W kg}^{-1}$  due to surface wind stress and has been removed.....76

**Figure 41.** Same as in Figure 40, but by injecting 5000 particles  $\text{m}^{-3}$ .....77

**Figure 42.** Same as in Figure 40, but by injecting 1000 particles  $\text{m}^{-3}$ .....78

**Figure 43.** Gulf of Mexico CFD model setup. The domain was a 50 x 50 x 250 m box representing a section of the Gulf of Mexico. Initial density and velocity profiles were determined from interpolated profiles of ARGO floats.....80

**Figure 44.** Modeling turbulence produced by DVM of zooplankton in the Gulf of Mexico by injecting 10,000 positively buoyant particles with 0.01 m diameter at 100 m: (a) particle locations at five-minute intervals; (b) contour plots of vertical velocity ( $\text{m s}^{-1}$ ); (c) average profiles of dissipation rate  $\epsilon$  ( $\text{W kg}^{-1}$ ). Background turbulence dissipation rate in the Straits of Florida is set at  $10^{-9} \text{ W kg}^{-1}$  following measurements by Kunze et al. (2006).....81

**Figure 45.** Magnetic signature of bio-turbulence 20 min after injecting positively buoyant particles with 0.01 m diameter at 100 m: (Left) Magnetic signature of extreme concentration of zooplankton and particle location 20 min after injection; (b) magnetic signature of low concentration of zooplankton and particle location 20 min after injection.....82

**Figure 46.** Electric signature of bio-turbulence 20 min after injecting positively buoyant particles with 0.01 m diameter at 100 m: (Left) Electric signature of extreme concentration of zooplankton and particle location 20 min after injection; (b) electric signature of low concentration of zooplankton and particle location 20 min after injection.....83

**Figure 47.** CFD simulation of 2 m amplitude, 36 m long surface waves. Contour plots of U velocity (left) and W velocity (right) with an isosurface of density showing the air-sea interface.....84

**Figure 48.** Magnetic signature of surface waves. (Left) Center plane, side-view contour plot of the magnetic signature,  $B_0$ , produced by surface waves. (Right) Amplitude of the magnetic signature of surface waves.....85

**Figure 49.** Initial condition for the internal wave breaking on the continental slope. (Top) Center plane contour plot of the initial density anomaly; (bottom) center plane contour plot of density at the time of the MHD simulation.....86

**Figure 50.** Center plane contour plot at 1500 s of (top) magnitude of the magnetic field fluctuations and (bottom) magnitude of the electric field fluctuations due to an internal wave breaking on the continental slope.....87

**Figure 51.** Model setup of freshwater lens simulation. Top shows the density center plane contour plot at the model initialization. Bottom shows the density center plane contour after the freshwater lens has spread for 660 s.....88

**Figure 52.** Magnetic signature of freshwater lens after 660 s of propagation. Center plane contour plot of a) temperature, b) magnitude of the magnetic signature of the freshwater lens spreading, and c) electric signature of the lens spreading.....89

**Figure 53.** CFD simulation of Langmuir cells and ramp-like structures. Contour plots of U velocity after 10,000 s.....91

**Figure 54.** Magnetic signature of Langmuir circulation. (Top) Contour plot at 10 m depth (top view) of the magnetic signature of Langmuir circulation. (Bottom) Contour plot in the center plane of the domain (side view) of the magnetic signature of Langmuir circulation.....92

**List of Tables**

**Table 1.** Wave number calculation for internal wave solitons observed during the 2017 Ambient Weather Experiment.....51

**Table 2.** Comparison of the typical magnetic signature produced by different small-scale oceanographic processes as produced by the verified MHD model.....93

## 1. Introduction

Seawater is a conductive medium and when it moves in the Earth's magnetic field, it induces eddy currents that flow through the seawater, thereby generating electromagnetic signatures representative of the velocity field in the ocean (Faraday 1832). As we continue to understand and exploit the marine environment, electromagnetic effects are becoming widely applicable (<https://www.marelec.co.uk/>). Electromagnetics in the ocean, including small- and fine-scale processes, are relevant to a growing number of applications including oil and mineral exploration, maritime sensing, influences on marine life, etc. The magnetic signature of the oceanographic processes can be viewed as electromagnetic noise from the perspective of underwater monitoring. The quantification of this ambient noise in the ocean environment could help to establish the limits of underwater electromagnetic background sensing. Additionally, some biological organisms can produce a turbulent wake, which may have a measurable magnetic signature. In particular, diel vertical migration (DVM) of zooplankton has been found to produce turbulence when large concentrations of zooplankton are undergoing migration (Dean et al. 2016a). This dissertation explores the effect of the concentration of zooplankton on the turbulence generation and its respective electromagnetic signature produced during migration.

The small- and fine-scale processes inherently involve three-dimensional (3D) dynamics. In the oceanographic literature, the term fine-scale structure refers to inhomogeneities relating to stratification (layering), while the term small-scale structure (or microstructure) has often been applied to 3D inhomogeneities associated with turbulence (Gregg 1975, Soloviev and Lukas 2014). Understanding 3D fluid dynamics, including biophysical interactions, in the ocean is essential in quantifying the electromagnetic signatures.

Since the 1950s, the models based on Maxwell's electromagnetic theory were developed to predict the magnetic signature of surface and internal ocean waves (Weaver 1965, Beal and Weaver 1970, Podney 1975, Lilley et al. 2004). These traditional models of the electromagnetic signatures of oceanographic processes were of an analytical nature, did not account for three-dimensional dynamics or turbulence, and were not able

to describe the variety of the environmental conditions occurring in the ocean. Furthermore, none of these models have been confidently validated with field or laboratory data. This dissertation aims to quantify the magnetic signature of small- and fine-scale oceanographic processes using computational fluid dynamics (CFD), magnetohydrodynamic (MHD), and magnetostatic model tools verified with analytical solutions and laboratory and field data.

In this introduction chapter, Section 1.1 reviews DVM of zooplankton; while, Section 1.2, surface and internal waves, Section 1.3, freshwater lenses, and Section 1.4, coherent structures. Section 1.5 discusses the theory behind small-scale oceanographic processes producing a magnetic signature. Section 1.6 states the main research hypotheses and the objectives of this dissertation, and outlines the work conducted.

### **1.1. Diel vertical migration (DVM)**

DVM of zooplankton is the largest animal migration on Earth (Andersen and Nival 1991) with approximately 15% of all zooplankton biomass undergoing DVM (Ianson et al. 2004). In certain nutrient-rich areas, such as coastal areas and the Southern Ocean, very large concentrations of zooplankton can undergo migrations; in particular, concentrations of up to 30,000 organisms/m<sup>3</sup> have been reported (Hamner 1984).

DVM is thought to be a predator avoidance behavior. This migratory behavior is based on the abundance of predators, food, and level of satiation (Gliwicz 1986, Lampert 1989, De Robertis et al. 2003). The amount of food in deep waters is not sufficient to meet the metabolic energy requirements for many zooplankton so these organisms must migrate to the surface waters to feed (Stich and Lampert 1981). However, visually oriented predators are more likely to be able to see their prey during the daylight hours, which leads to zooplankton remaining in darker, deeper waters during the day and migrating toward the surface waters in the evening (Enright 1977).

DVM of zooplankton can be observed with acoustic instruments as a deep scattering layer. This migration has been observed in the Straits of Florida with an acoustic Doppler current profiler (ADCP) Workhorse Longranger 75 kHz for an 11-month period (Dean et al. 2016a). The 75 kHz ADCP responds to particles or aggregates of particles 8 mm or

larger. The contour plot of acoustic backscatter signal from the ADCP clearly shows a periodic pattern with high backscatter in the surface water at night, followed by high backscatter in the mid-depths during the day (Fig. 1). Sunrise and sunset times have been superimposed on the same plot where sunrise is indicated by a solid white line, and sunset as a dashed white line (Fig. 2). Sunrise and sunset times clearly coincide with the changes in the backscatter signal in the upper ocean, suggesting the presence of a DVM cycle.

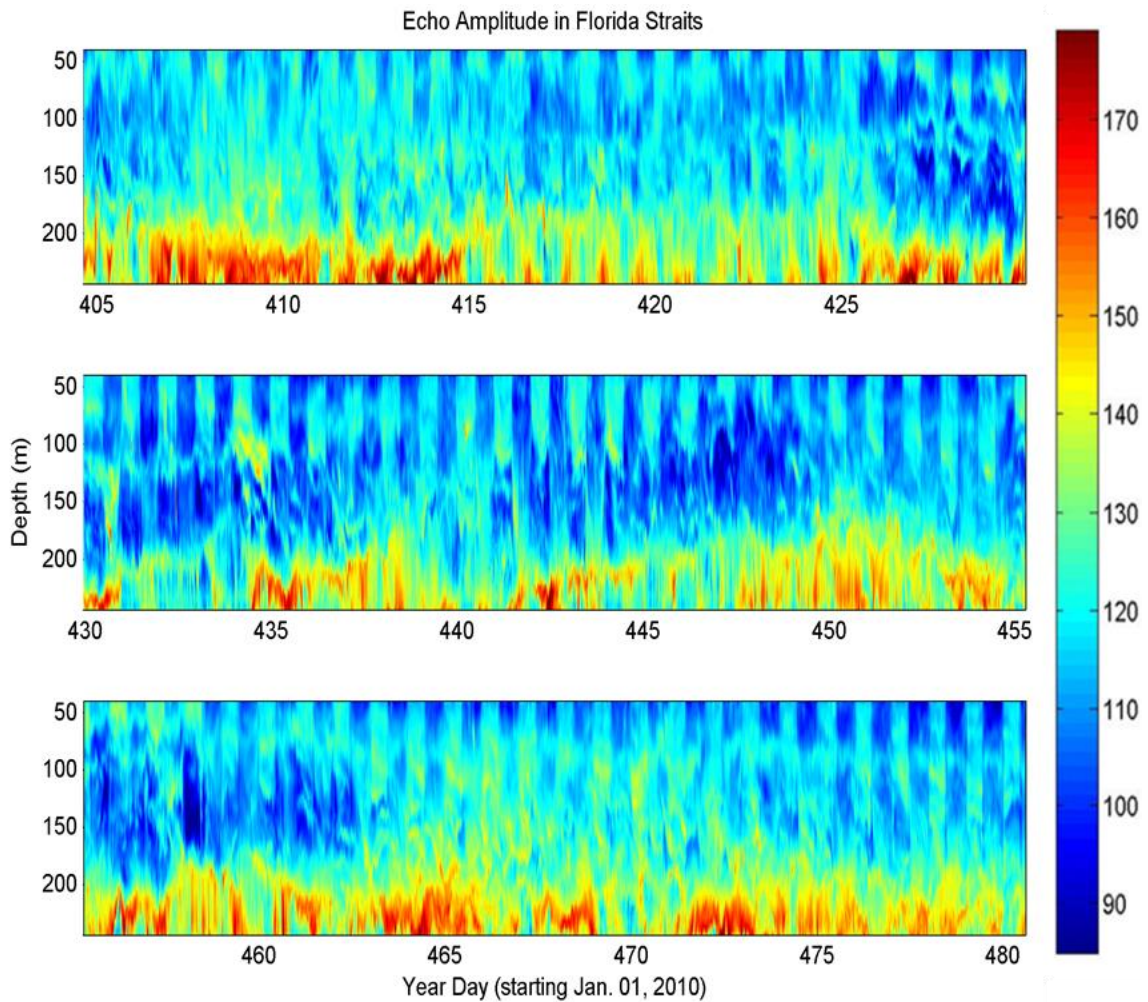


**Figure 1.** Acoustic backscatter from bottom-mounted ADCP for a subset of an 11-month data set in the Straits of Florida. (After Dean et al. 2016a.)

Munk (1966) first proposed the term biological mixing, also known as biomixing, in jest, suggesting that biological mixing may contribute to the ocean energy budget to some extent. Since then, there have been a number of studies that indicated biology may, in

fact, increase mixing in the ocean (see *e.g.*, Dewar et al. 2006, Kunze et al. 2006, Wilhelmus and Dabiri 2014). Dewar et al. (2006) used three methods to calculate the impact of the biology on the global ocean energy budget, and all three indicated that the biosphere input approximately 1 TW of energy into this budget. Migrating organisms can transport cold water from the deep ocean toward the surface and warm water from the near-surface toward deep layers of the ocean, which may have an effect on global circulation (Dewar et al. 2006). This cooler, nutrient-rich water may enhance primary production in the near-surface layers of the ocean (Jenkins and Doney 2003).

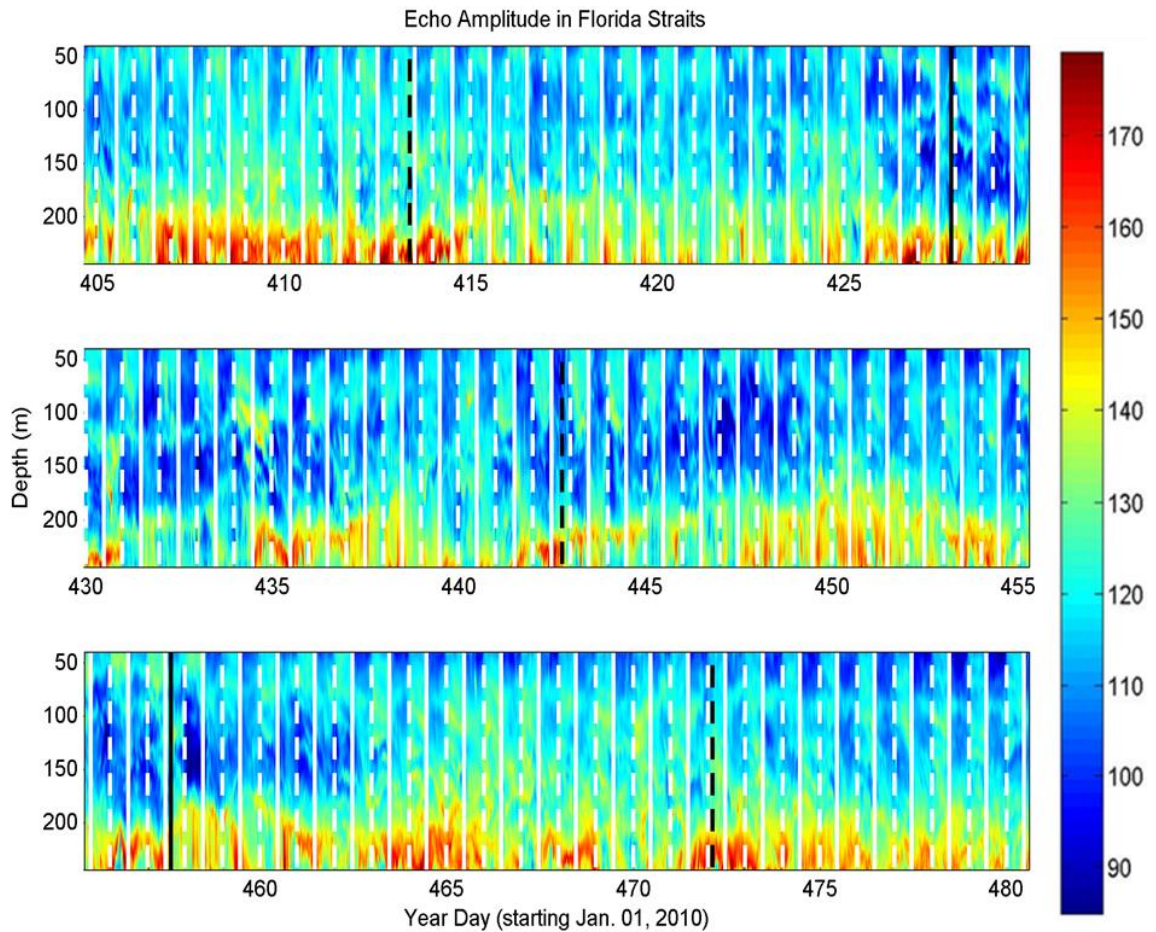


**Figure 2.** Acoustic backscatter from bottom-mounted ADCP for a subset of an 11-month data set with sunrise times indicated by a solid white line, sunset by a dashed white line, new moon by a solid black line, and full moon by a dashed black line. Near surface bins have been removed due to multiple reflections. (After Dean et al. 2016a.)



Swimming-induced turbulence is caused by the migration of zooplankton through the water column (Huntley and Zhou 2004), which has been confirmed in laboratory studies (Catton et al. 2011, Wilhelmus and Dabiri 2014). Wilhelmus and Dabiri (2014) artificially induced DVM of *Artemia salina*, a brine shrimp, in a tank and used particle image velocimetry technology to visualize the flow field (Fig. 3). These results indicated that DVM caused eddy-like structures with length scales larger than individual organisms. Swimming organisms in schools or swarms can generate dissipation rate of turbulent kinetic energy on the order of  $10^{-5} \text{ W kg}^{-1}$ , which is several orders of magnitude higher than average dissipation rates of turbulent kinetic energy in the stratified ocean (Huntley and Zhou 2004, Dewar et al. 2006). This increase in dissipation is comparable with that associated with major storms (MacKenzie and Leggett 1993). Hence, biomixing may be a source of fine-scale turbulent mixing on local spatial and temporal scales.

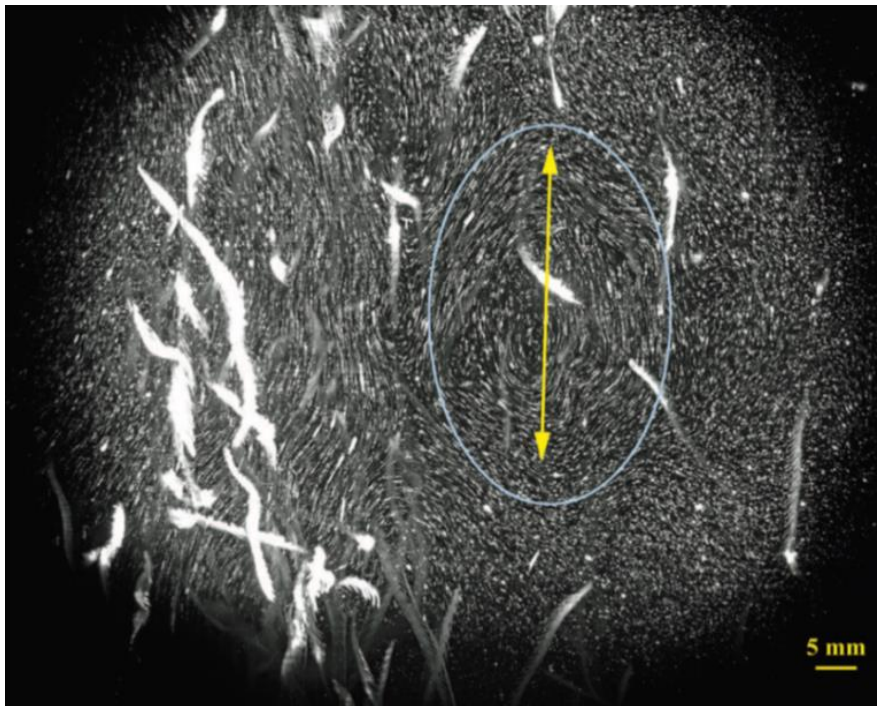


**Figure 3.** Flow visualization from particle image velocimetry experiment showing zooplankton swimming creates turbulent motions on scales larger than individual organisms. (After Wilhelmus and Dabiri 2014.)

Kunze et al. (2006) observed a spatially localized increase in dissipation rate of turbulent kinetic energy of four to five orders of magnitude over background turbulence

in the wake of a school of vertically migrating krill, *Euphausia pacifica* (Fig. 4). The DVM and associated elevated levels of turbulence were short in duration but resulted in an increase in the daily-averaged turbulent eddy diffusivities by two to three orders of magnitude. In schools or swarms of swimming organisms, the small-scale turbulence generated from an individual organism does not have time to decay before being encountered by another organism, causing an increase in the turbulence length and temporal scale (Gregg and Horne 2009).

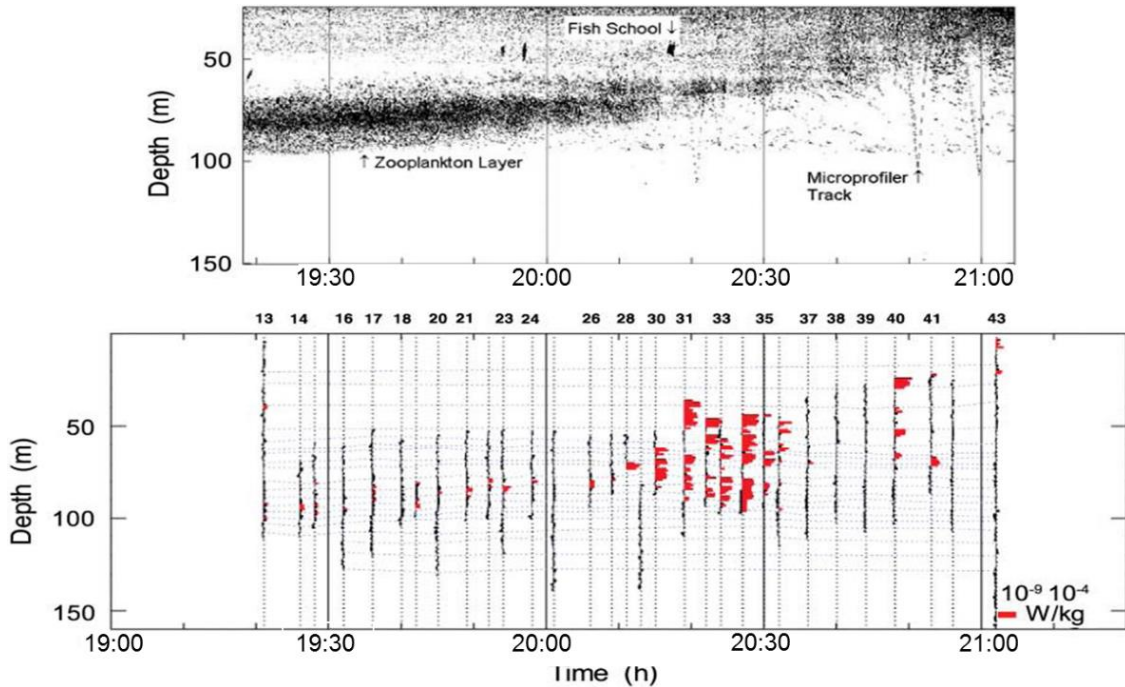


**Figure 4.** Turbulence signature of DVM of krill in Saanich Inlet. (Top) Acoustic backscatter data from a 200-kHz echosounder reveals vertical migration of the backscatter layer. (Bottom) Profiles of the vertical microstructure profiler. Red indicates the increase of dissipation rate of turbulent kinetic energy over background levels. (After Kunze et al. 2006.)

New research has shown that organisms undergoing DVM produce a distinctive low-frequency humming or buzzing sound. Baumann-Pickering et al. (2016) observed DVM cycles in the San Diego Trough through a calibrated multiple-frequency split-beam echosounder. Sound produced by organisms undergoing DVM were recorded using a high-frequency recording package (10 Hz to 100 kHz). The organisms produced sound with a frequency ranging from 300 and 900 Hz that was three to six decibels louder than

background noise and lasted for one to two hours close to the time of DVM (Fig. 5). It is still uncertain why this noise is produced. It could be due to turbulence generated by DVM of zooplankton or it could simply be used for communication between organisms. Note that turbulence can produce sound through vortex shedding (White and Neph 2003). If this sound is indeed coming from turbulence generation, this finding could potentially provide an alternative method of detection of the turbulence generated by DVM.

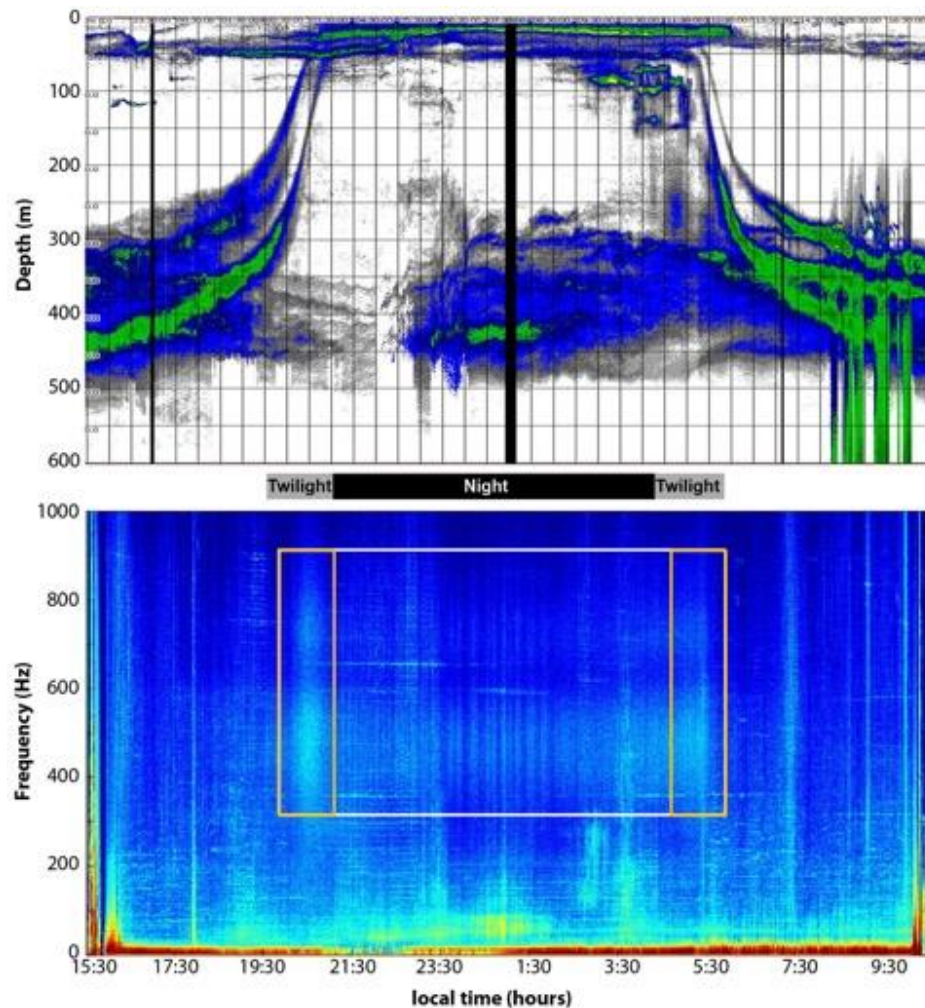


**Figure 5.** Measurement of DVM in the San Diego Trough. (Top) Migration of animals up to surface waters at sunset and down at sunrise. (Bottom) Sound associated with migration (outlined by rectangles). (After Baumann-Pickering et al. 2016.)

Other physical oceanographic features like density differences due to freshwater lenses can affect DVM of zooplankton. Freshwater lenses in the near-surface layer of the ocean produced by convective rains or river runoff are usually localized in space and

typically involve both salinity and temperature anomalies. Zooplankton which undergo DVM tend to be in larger concentrations in freshwater lenses produced by river runoff due to higher nutrient levels (Diaz et al. 2008, Nicolle et al. 2009).

During oil spills, emulsions can form. The viscosity of oil emulsions can be considerably greater than the viscosity of either the oil or water because of non-Newtonian behavior (PetroWiki 2015). The high viscosity of emulsions may act as a barrier to DVM of zooplankton. If zooplankton do encounter oil and dispersants in the water column during migration, that can have an impact on the vertical transport of the anthropogenic pollutants through the water column. Moreover, anthropogenic pollutants such as oil spills and dispersants may also affect behavioral patterns of zooplankton, including DVM, with largely unknown but possibly dramatic, or even lethal effects on marine ecosystems. The study of DVM of zooplankton can help to improve the understanding of how marine ecosystems will respond to potential oil spill events (*e.g.*, in the Gulf of Mexico and the Straits of Florida).

## **1.2. Surface and internal waves**

In the ocean, wave-type disturbances can take the form of surface waves or internal waves. The large density difference between air and water prevents the surface waves from becoming too high. However, the density differences within the ocean are much smaller and much less energy is required to move the water vertically. Therefore, amplitudes of internal waves can be quite large.

The study of surface gravity waves is one of the oldest areas of fluid dynamics. In particular, the motion of waves was one of the earliest applications of classical potential theory, which is a good approximation for surface waves. The fluid can be assumed to be inviscid and the motion irrotational.

In linear wave theory (Phillips 1977), the wave amplitude is small compared to the wavelength. Here a sinusoidal disturbance is considered. This theory can easily be expanded to account for a more complicated wave field since, by Fourier's theorem, any arbitrary disturbance can be viewed as a superposition of elementary waves. In this case, the surface displacement of the 2D plane harmonic waves is described as follows:

$$\eta = a \cos(kx - \omega t) \quad (1)$$

and the associated velocity potential for linear waves is

$$\phi = \frac{\omega a \cosh k(z+h)}{k \sinh kh} \sin(kx - \omega t) \quad (2)$$

where  $\omega$  is the wave frequency,  $k$  is the wave number,  $a$  is the amplitude,  $h$  is the height of the water column, and  $z$  is the depth. The wave frequency and wavenumber are related through the dispersion relation as follows:

$$\omega(k) = \left[ (gk + \sigma_s k^3 / \rho) \tanh kh \right]^{1/2} \quad (3)$$

where  $g$  is the acceleration due to gravity and  $\sigma_s$  is the surface tension (Soloveiv and Lukas 2014). The phase velocity of the wave is  $c = \left( \frac{\omega}{k} \vec{l} \right)$ , where  $\vec{l} = \frac{\vec{k}}{k}$  is the unit vector in the direction of the wavenumber. The group velocity is  $c_g = \nabla_k \omega(k)$ , where  $\nabla_k$  is the gradient operator in wavenumber space (Phillips 1977).

Deep water waves are defined as  $kh \gg 1$ . In this special case, Equation (2) reduces to

$$\phi = k^{-1} a \omega e^{kz} \sin(kx - \omega t) \quad (4)$$

with the dispersion relation

$$\omega(k) = (gk + \sigma_s k^3 / \rho)^{1/2}. \quad (5)$$

Following Equation (5), the phase speed becomes

$$c = \frac{\omega}{k} = \left( \frac{g}{k} + \frac{\sigma_s k}{\rho} \right)^{1/2}. \quad (6)$$

The phase speed of gravity waves increases with wavelength or with decreasing wave number.

In reality, however, surface waves are not always as simple as described above. The waves are not necessarily deep water waves (see Equations (7)-(11)). When the ratio of wave amplitude to wavelength increases, waves are deformed, become nonlinear (*e.g.*, see Equation (13) for the Kortweg-de Vries (KdV) theory) and unstable, and eventually break. Waves that break disrupt the sea surface and entrain air in the ocean in the form of whitecaps, bubbles, and spray droplets. In this way surface waves play an important role in the transport of energy from the atmosphere (Melville 1996).

Internal waves are gravity waves moving through a continuously stratified fluid, while interfacial waves are gravity waves at the interface of two water layers of different constant densities. Typical wavelengths of internal waves range from hundreds of meters to tens of kilometers, and have periods ranging from minutes to hours. Maximum orbital velocities occur at the pycnocline and decrease in both directions away from the pycnoclines (Massel 2015).

A simplified two-layer model of internal waves can prove useful for describing some internal waves, such as those in coastal regions or where well-mixed oceanic water overlies deeper water, creating a sharp thermocline. In this model, a layer of water with depth  $h_1$  and uniform density  $\rho_1$  lies on top of a water layer with height  $h_2$  and uniform density  $\rho_2$ , where  $\rho_2 > \rho_1$ . The total water depth is  $h = h_1 + h_2$ . The internal wave with frequency  $\omega$  and wavenumber  $k$  propagates at the interface between the two layers. It is assumed that  $\omega^2 \gg f^2$  so that the Earth's rotation can be ignored. For this model, the velocity potentials are as follows:

$$\begin{aligned}\phi_1(x, z, t) &= -\frac{\omega}{k} A \frac{\cosh(kz)}{\sinh(kh_1)} \sin(kx - \omega t) \text{ and} \\ \phi_2(x, z, t) &= \frac{\omega}{k} A \frac{\cosh[k(z+h)]}{\sinh(kh_2)} \sin(kx - \omega t)\end{aligned}\tag{7}$$

for the upper and lower layers, respectively. The dispersion relation is defined as

$$\omega^2 = \frac{gk(\rho_2 - \rho_1)}{\rho_1 \coth(kh_1) + \rho_2 \coth(kh_2)}\tag{8}$$

and the phase velocity is

$$C_0 = \frac{\omega}{k} = \sqrt{\frac{g}{k} \frac{(\rho_2 - \rho_1)}{\rho_1 \coth(kh_1) + \rho_2 \coth(kh_2)}}. \quad (9)$$

The orbital velocities  $u$  and  $w$  are determined from Equation (7) as follows

$$\begin{aligned} u_1(x, y, z, t) &= \frac{\partial \phi_1}{\partial x} = -\omega A \frac{\cosh(kz)}{\sinh(kh_1)} \cos(kx - \omega t) \\ w_1(x, y, z, t) &= \frac{\partial \phi_1}{\partial z} = -\omega A \frac{\sinh(kz)}{\sinh(kh_1)} \sin(kx - \omega t) \end{aligned} \quad (10)$$

in the upper layer and

$$\begin{aligned} u_2(x, y, z, t) &= \frac{\partial \phi_2}{\partial x} = \omega A \frac{\cosh[k(z+h)]}{\sinh(kh_2)} \cos(kx - \omega t) \\ w_2(x, y, z, t) &= \frac{\partial \phi_2}{\partial z} = \omega A \frac{\sinh[k(z+h)]}{\sinh(kh_2)} \sin(kx - \omega t) \end{aligned} \quad (11)$$

in the lower layer.

If the wavelength of the internal wave is longer than the ocean depth and the amplitude is small, these waves can be treated as the weakly nonlinear waves with steepening crests. Kortweg-de Vries (KdV) theory can describe these types of waves (Korteweg and de Vries 1895, Miles 1981). The KdV theory has a balance between nonlinearity and dispersion and is parameterized by the following:

$$\alpha = \frac{A}{h}, \quad \beta = \left(\frac{h}{l}\right)^2 \quad (12)$$

where  $A$  is the wave amplitude and  $l$  is the length scale. Both of these parameters must be small and of the same order. When these two effects are balanced, the solution to the KdV equation can result in solitary internal waves, also known as solitons. For these solitary waves the classical KdV equation is

$$\frac{\partial \zeta}{\partial t} + C_0 \frac{\partial \zeta}{\partial x} + \alpha \zeta \frac{\partial \zeta}{\partial x} + \beta \frac{\partial^3 \zeta}{\partial x^3} \quad (13)$$

where  $\zeta$  is the displacement of the interfacial wave,  $C_0$  is the linear phase velocity,

$\alpha = \frac{3}{2} C_0 \frac{h_1 - h_2}{h_1 h_2}$ , and  $\beta = \frac{C_0}{6} h_1 h_2$ . The solitary wave speed is

$$U = C_0 \left( 1 + \frac{1}{2} \frac{h_1^2 - h_2^2}{h_1 h_2} \frac{A}{h_2} \right) \quad (14)$$

and the shape of the wave is

$$\zeta(x, t) = A \cosh^{-2} \left[ \sqrt{\frac{3A}{4h_r^3}} (x - Ut) \right] \quad (15)$$

where the characteristic water depth  $h_r^3 = h h_2^2 \left[ 1 - \left( \frac{h_2}{h_1} \right)^2 \right]^{-1}$ .

Internal waves can play an important role in mixing the ocean. They contribute to the vertical velocity in the ocean, which helps to support the global thermohaline circulation (Munk 1966, Massel 2015). Internal waves can also have an impact on biological productivity. The mixing produced by the waves can increase the nutrient concentration locally, increasing primary production (Kahru 1983). Additionally, internal waves can transport planktonic larvae from remote larval pools, enhancing genetic variability (Botsford et al. 1994). Internal wave solitons also have a prominent magnetic signature.

### 1.3. Freshwater lenses

The upper ocean turbulent boundary layer is a dynamically active zone of the ocean. Fluxes of momentum, mass, heat and kinetic energy at the air-sea interface result in a variety of turbulent and organized structures developing in the near-surface layer of the ocean. These structures are inherently three-dimensional.

Convective rains and/or river runoff produce freshwater lenses. These lenses of freshened water in the near surface layer of the ocean are localized in space and typically



involve both salinity and temperature anomalies. The significant density anomalies created by these freshwater lenses produce horizontal pressure gradients in the near-surface layer of the ocean. As a result, these lenses can spread and propagate as classical gravity currents, producing a typical gravity current "head". These structures resemble a complex pattern of three-dimensional water flow motions in the leading edge of the gravity current and trailing fluid, previously reported by Ozgökmen et al. (2004) and Soloviev et al. (2015b). There is some asymmetry of the lens edges due to the effect of the wind (Soloviev and Lukas 1997). An interesting phenomenon is the development of coherent structures at the frontal edge of the spreading freshwater lens, which apparently intensifies mixing. The patterns in gravity currents are inherently three dimensional.

The freshwater lens can either completely mix with the environment or achieve a compensated state when temperature and salinity anomalies compensate each other in the density field. At this stage, the horizontal pressure gradients diminish and lateral spreading ceases. The compensated lenses are then subject to erosion by double diffusion and cabbeling (Dean et al. 2016b).

The dynamics of freshwater lens spreading can be linked to the formation of the barrier layer (Lukas and Lindstrom 1991) and sharp frontal interfaces (Soloviev and Lukas 1997), thus influencing large scale oceanographic processes. Freshwater lens spreading has a number of practical applications including pollution propagation in coastal waters (*e.g.*, oil spills), open ocean dynamics (*e.g.*, Madden-Julian Oscillation), and interpretation of Aquarius and SMOS sea surface salinity satellite measurements. The lens spreading also plays an important component of the tropical ocean environment in the Intertropical Convergence Zone (*e.g.*, Wijesekera et al., 1999).

#### **1.4. Coherent structures**

The ocean temperature-salinity structure, circulation, and mass exchanges (including greenhouse gases and pollutants) depend on turbulent mixing and non-local transport in the near-surface layer of the ocean. Spatially coherent organized motions have been recognized as an important part of turbulent boundary layer processes (Thorpe 1985; Thorpe et al. 2003). Langmuir cells and ramp-like structures are believed to vertically

transfer an appreciable portion of the momentum, heat, gases, pollutants (*e.g.*, oil), and other substances in the upper layer of the ocean. The free surface of the ocean significantly complicates the analysis of turbulent exchanges at the air-sea interface and the coherent structures are not yet completely understood.

Langmuir cells are parallel and oriented nearly downwind in developed seas, with alternating longitudinal vorticity, producing convergence and divergence zones (Pollard 1977). The convergence zones are substantially narrower than the divergence zones. The spacing between the Langmuir vortices ranges from a few meters to a few hundred meters. Langmuir circulation can be seen on the sea surface due to the collection of flotsam or foam from breaking waves in convergence zones and appear to be transient in nature. For fully developed local seas, the orientation of wind, wave, and Langmuir cells is practically the same. In general, however, they do not necessarily coincide.

The atmospheric boundary layer above land exhibits spatially coherent organized motions in the form of “ramps” (Antonia et al. 1979; Phong-Anant et al. 1980). Ramp-like structures are discovered to be a widespread feature in the upper ocean as well and have been found under both stable (Thorpe and Hall 1987) and unstable (Soloviev 1990) stratification.

Wijesekera et al (1999) collected large statistics on ramp-like structures during TOGA COARE. These data suggested that the direction of frontal interfaces produced by ramp-like structures is approximately perpendicular to the wind direction.

According to the field study performed by Thorpe et al. (2003) using an autonomous underwater vehicle, both types of coherent structures, Langmuir cells and ramp-like structures coexist. Vortices associated with ramp-like structures have transverse axes, while Langmuir circulations have longitudinal axes, relative to the wind direction.

In traditional models, Langmuir circulation is driven by the Stokes vortex force (Leibovich 1983), which in the case of aligned winds and waves is as follows:

$$F_S = \vec{u}_S \times (\nabla \times \vec{U}) = \vec{j}\vec{u}_S (\partial_y u - \partial_x v) + \vec{k}\vec{u}_S \partial_z u \quad (16)$$

where  $\vec{u}_s$  is the Stokes drift velocity vector and  $\bar{u}_s$  is its component along the wave direction,  $\vec{U}$  the water velocity vector,  $u$  and  $v$  the horizontal velocity components in the wind stress and across wind stress direction, respectively;  $\vec{j}$  and  $\vec{k}$  are the unit vectors in the horizontal and vertical direction, respectively.

Kudryavtsev et al. (2008) found the velocity gradients beneath the sea surface to be 2 to 5 times weaker than in the “wall” (logarithmic) boundary layer. The near-surface ocean is almost uniform due to wave-breaking stirring. Furthermore, Terray et al. (1999) concluded that due to wave stirring, the near surface layer becomes like a “slab” layer (Fig. 3c). As a result,

$$\partial u / \partial z \rightarrow 0. \quad (17)$$

Thus, the vertical component of the vortex force  $\vec{F}_v = \vec{k}\bar{u}_s\partial_z u$  may vanish in that layer due to wave-breaking mixing (Terray et al. unpublished manuscript). The horizontal component of the vortex force  $F_h = \vec{j}\bar{u}_s(\partial_y u - \partial_x v)$  is associated with the vertical component of vorticity  $\eta = (\partial_y u - \partial_x v)$ , which is of a fluctuational nature. There are significant fluctuations of  $\eta$  in the wave-breaking layer (see, *e.g.*, Sullivan et al. 2007). However, these fluctuations are random and, thus, uncorrelated with the Stokes drift velocity  $\bar{u}_s$ , which is an average over many wave periods. As a result, the horizontal component of the vortex force  $F_h$  can produce only random convergence-divergence zones, resulting in “fish scale”- like patterns on the sea surface but not in spatially-coherent organized motion typical for Langmuir circulation. There is no mechanism which could couple and synchronize Stokes drift with the near-surface turbulence in the wave-breaking layer.

Li et al. (2013) simulated the observations collected at the Martha’s Vineyard Coastal Observatory’s Air-Sea Interaction Tower during the CBLAST experiment in 2003 using an LES model. The model showed that breaking waves dominated turbulence generation near the ocean surface over the Stokes term production. In fact, diagnostic analysis of the TKE budget in the model of Li et al. (2013) shows a dominant balance between turbulent

transport and dissipation near the surface and a dominant balance between shear production and dissipation at deeper depths. Although the Stokes production is a significant term in the TKE budget balance near the surface, it is smaller than shear production (Li et al. 2013). Langmuir circulation could develop deeper in the water column; though, according to Li et al. (2013), the Stokes production is much smaller than shear production and dissipation below the wave stirred layer. It is therefore not obvious that large eddies below the layer of wave breaking turbulence were driven by Stokes drift in the Li et al. (2013) model. Based on the above considerations, Soloviev and Dean (2015) and Soloviev et al. (for submission) have developed a coupled model of ramp-like structures and Langmuir Circulation, which does not require the Craik-Lebovich vortex force.

### **1.5. Magnetic signature of small- and fine-scale oceanographic processes**

Under certain conditions, some small- and fine-scale processes in the ocean can produce measurable magnetic signatures. In particular, the magnetic field fluctuations produced by ocean waves are dependent on many parameters including wave frequency, wave propagation direction with respect to the Earth's magnetic field, seafloor conductivity and permeability, and conductivity of the seawater, as well as the location of the observations (Smagin et al. 2014). Fluctuations in Earth's magnetic field induced by ocean waves, both surface and internal, have been theoretically investigated since the 1950s (Longuet-Higgins et al. 1954, Weaver 1965, Podney 1975, Chave 1984). Lilley et al. (2004) compared these theoretical investigations with magnetic measurements collected off the southern coast of Australia and found a qualitative consistency between the measurements and the theoretical investigations. There, however, has been no quantitative verification of the above models with observations, either in Lilley et al. (2004) or others.

A CFD model with a MHD add-on module had been applied to model and internal wave soliton with ambient stratification (Matt et al. 2014, Soloviev and Dean 2015). This model was verified with the magnetostatic model developed at the Naval Research Laboratory. These authors modeled an internal wave soliton in a domain 2 km long, 1 km

wide, and 250 m deep. The mesh resolution was 10 m in the horizontal direction and 2 m in the vertical direction with increased vertical mesh resolution in the thermocline. The thermal stratification was similar to that observed on the South Florida shelf. The MHD solution for this soliton simulation (Soloviev et al. 2013, Soloviev et al. 2015a) was calculated with the “frozen” velocity field of this hydrodynamic simulation and using a steady MHD model (as described in Section 2.2). Water conductivity was 4.788 S/m. The top wall had a conducting boundary condition with  $5.5 \times 10^{-15}$  S/m and the bottom wall had a conducting boundary condition with 0.4788 S/m. All other boundaries had an insulating boundary condition. The Earth’s magnetic field was set as follows:  $B_x = -2.7 \times 10^{-5}$  T,  $B_y = 2.52 \times 10^{-6}$  T,  $B_z = -3.7 \times 10^{-5}$  T. The MHD model results indicated that the internal wave soliton produced a magnetic signature on the order of 10 nT.

The modeled internal wave soliton produced a strong magnetic signature reaching several nT at the leading edge of the wave. This magnetic field signature was well within the range detectable by modern magnetometers and was consistent with the Naval Research Laboratory magneto-static model for the same domain size and wave size (Fig. 6). Note that the magnetic boundary conditions and mesh spatial resolution are somewhat different between the two simulations. Also, the Matt et al. (2014) and Soloviev and Dean (2015) simulation does not account for the boundary layer effects or self-inductance. This may explain the difference in the magnetic signature between the Naval Research Laboratory and the Matt et al. (2014) and Soloviev and Dean (2015) models. This deficiency of the CFD model has been corrected in this dissertation by accounting for self-inductance and bottom boundary layer physics.

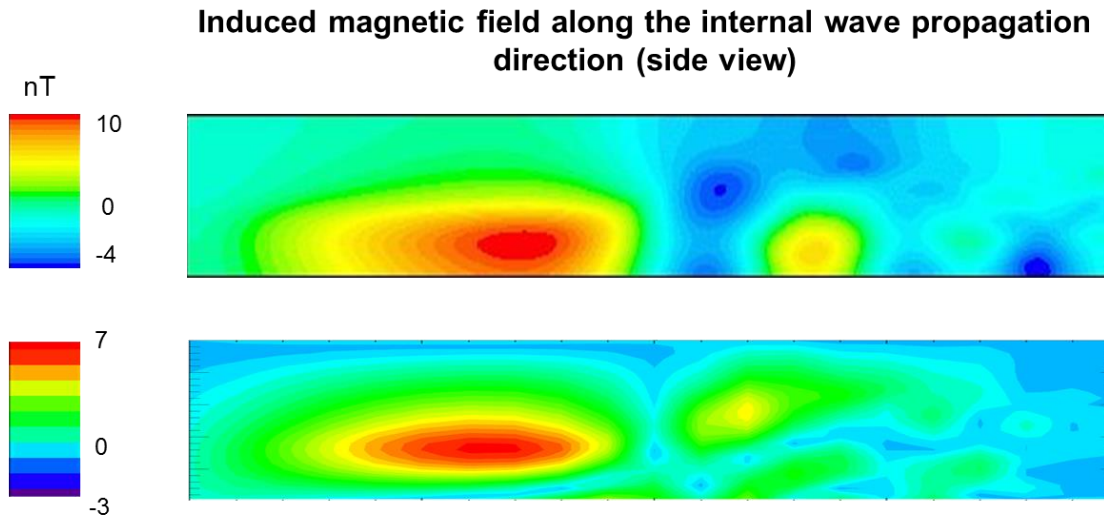


**Figure 6.** Magnetic signature of internal waves. (Top) *ANSYS Fluent* simulation of internal wave. (Bottom) Naval Research Laboratory magneto-static model. (After Matt et al. 2014.)

The magnetic signature of oceanographic phenomena such as surface waves, turbulence, spatially coherent structures, internal waves, diurnal jets, propagating freshwater lenses, and other small- and fine-scale processes can potentially be measured using sensitive magnetometers. Turbulence produced by DVM of zooplankton may have a measurable magnetic signature as well (Dean and Soloviev 2018). The magnetic signature of these processes can also be modeled using coupled CFD and MHD simulations (Soloviev and Dean 2018). These models are presented in more detail in Section 2. Magnetics measurements and simulations may also provide a method for indirectly determining the turbulence generation of DVM and other processes.

### 1.6. Goal

The overarching goal of this dissertation research is to introduce CFD methods in the calculation of the electromagnetic signature of small- and fine-scale oceanographic processes. To achieve this goal, the following tasks have been performed:

- Review of the literature related to small- and fine-scale oceanographic features
- Review existing analytical models of the electromagnetic signature of surface and internal waves

- Develop a suite of CFD, MHD, and magnetostatic models based on *ANSYS Fluent* with the MHD module and *ANSYS Maxwell*
- Verify these models with known analytical solutions, laboratory experiments, and available field data
- Identify shortcomings of the computational models
- Account for the seawater and seafloor electromagnetic properties
- Calculate the magnetic signature of DVM of zooplankton, internal waves, surface waves, freshwater lenses, and coherent structures for typical environmental conditions
- Evaluate the relative contributions of these processes in the magnetic noise in the ocean

The outline of the remainder of this dissertation is as follows: Chapter 2 describes the suite of numerical models developed and implemented for quantitative estimation of the magnetic signatures of various small- and fine-scale oceanographic processes. Chapter 3 discusses the magnetic model verifications with field and laboratory data and comparison with traditional, analytical models. Chapter 4 provides results of the modeling of DVM of zooplankton including the turbulence and magnetic signatures. Chapter 5 compares the magnetic signatures of various small scale oceanographic processes and Chapter 6 concludes this work.

## **2. Numerical models**

### **2.1. Computational fluid dynamics model**

A 3D, non-hydrostatic computational fluid dynamics (CFD) modeling software, *ANSYS Fluent*, is used in this work to simulate fine-scale processes in the ocean including DVM of zooplankton, freshwater lenses, surface waves, internal waves, undercurrent jets, and Langmuir circulation. Turbulence is modeled with the Large Eddy Simulation Viscosity model (LES), with Wall Adapting Local Eddy (WALE) as the sub-grid scale model (Nicoud and Ducros 1999) where the eddy viscosity is modeled by

$$\mu_t = \rho L_s^2 \frac{(S_{ij}^d S_{ij}^d)^{3/2}}{(\bar{S}_{ij} \bar{S}_{ij})^{5/2} + (S_{ij}^d S_{ij}^d)^{5/4}} \quad (18)$$

where  $L_s$  and  $S_{ij}^d$  in the WALE model are defined as  $L_s = \min(\kappa d, C_w V^{1/3})$  and

$$S_{ij}^d = \frac{1}{2}(\bar{g}_{ij}^2 + \bar{g}_{ji}^2) - \frac{1}{3} \zeta_{ij} \bar{g}_{kk}^2, \bar{g}_{ij} = \frac{\partial \bar{u}_i}{\partial x_j},$$

respectively. Here  $L_s$  is the mixing length for the

subgrid scales,  $\kappa$  is the von Karman constant,  $d$  is the distance closest to the wall, and  $V$  is the volume of the computational cell and the local grid scale  $\Delta = V^{1/3}$ . In *Fluent*, the default value of the WALE constant  $C_w$  is 0.325 (ANSYS *Fluent* 2013). The rate-of-strain

$$\text{tensor is } \bar{S}_{ij} = \frac{1}{2} \left( \frac{\partial \bar{u}_i}{\partial x_j} + \frac{\partial \bar{u}_j}{\partial x_i} \right).$$

Note, the LES model has an artificial length scale

separation between explicitly resolved and subgrid components (ANSYS *Fluent* 2013).

The LES WALE turbulence model does not directly solve for dissipation rate of turbulent kinetic energy. For verification of the CFD model, dissipation rate must be calculated in order to compare the simulation results with turbulence measurements during DVM by Kunze et al. (2006). Dissipation rate of turbulent kinetic energy,  $\epsilon$  is

$$\text{calculated from Delafosse et al. (2008) as } \epsilon = 2(v_T + \nu) S_{ij} S_{ij} = \frac{v_T + \nu}{2} \left( \frac{\partial u_i}{\partial x_j} + \frac{\partial u_j}{\partial x_i} \right)^2,$$

where

partial derivatives of velocity  $\frac{\partial u_i}{\partial x_j}$  and  $\frac{\partial u_j}{\partial x_i}$  are calculated by the model,  $v_T$  is subgrid

turbulent viscosity (exported from the model), and  $\nu$  is the molecular viscosity of water.

The partial derivatives are explicitly calculated in the LES model, while the turbulent viscosity is calculated from the subgrid-scale model, which accounts for turbulence produced by particle motion.

The discrete phase model (DPM) allows for the simulation of a discrete second phase in a Lagrangian frame of reference. In this work, the DPM is used to inject rigid spherical particles into the domain to simulate the DVM cycles of zooplankton (Dean et al. 2016a). The material of the particles is set as water, with the buoyancy adjusted to 1.2% more or less dense than the seawater to allow sinking or floating, depending on whether upward



or downward migration is simulated. Tests have been conducted to determine the correct buoyancy difference, which ensures a realistic vertical migration speed of several  $\text{cm s}^{-1}$ . The top and bottom walls of the domain are set to allow particles to escape, while the side walls are set to allow particles to reflect. The inlet is set to a periodic boundary condition, allowing particles to flow out of one side of the domain and back into the other side with the flow of the fluid. (The DPM model is also used for the injection of particles to simulate the presence of a nepheloid layer in the model of an internal wave breaking on the continental slope.)

A multiphase, volume of fluid (VOF) model is used to simulate air, water, and in some cases, a sediment layer in this dissertation. The VOF method can model immiscible fluids by solving an individual set of momentum equations and tracking the volume fraction of the separate fluids throughout the numerical domain. The VOF method tracks the volume fraction  $\alpha$  of each fluid, where any fraction of the  $q^{\text{th}}$  fluid is possible  $0 < \alpha_q < 1$ . The VOF method always ensures the sum is unity.

At the interfaces where more than one fluid is present in a cell, the VOF model uses the geometric interface reconstruction scheme, which is a piecewise-linear interpolation to calculate the advected fluid through each face (Youngs 1982). The tracking of the interface uses the following continuity equation:

$$\frac{1}{\rho_q} \left[ \frac{\partial}{\partial t} (\alpha_q \rho_q) + \nabla \cdot (\alpha_q \rho_q \bar{v}_q) \right] = S_{\alpha_q} + \sum_{p=1}^n (\dot{m}_{pq} - \dot{m}_{qp}) \quad (19)$$

where  $\rho_q$  is the density of the  $q^{\text{th}}$  fluid,  $\bar{v}_q$  is the velocity of the  $q^{\text{th}}$  fluid,  $\dot{m}_{pq}$  is the mass transfer from the  $p^{\text{th}}$  to the  $q^{\text{th}}$  fluid and  $\dot{m}_{qp}$  is the mass transfer from the  $q^{\text{th}}$  to the  $p^{\text{th}}$  fluid.  $S_{\alpha_q}$  is a user-defined source term that remained at the default value of zero for our numerical simulations.

## 2.2. Magnetohydrodynamic model

An MHD module combined with a 3D CFD model, based on *ANSYS Fluent* software is used in this work to study electromagnetic signatures of fine-scale oceanographic

phenomena. The *Fluent* MHD add-on module provides an opportunity to analyze the behavior of an electrically conducting fluid flow (*e.g.*, seawater) under the influence of a stationary magnetic field (the Earth's magnetic field). The MHD model is also able to accommodate the effect of a discrete phase (particles as a proxy for zooplankton).

The *Fluent* MHD model describes the electromagnetic fields by Maxwell's equations:

$$\nabla \cdot \vec{B} = 0 \quad (20)$$

$$\nabla \times \vec{E} = -\frac{\partial \vec{B}}{\partial t} \quad (21)$$

$$\nabla \cdot \vec{D} = q \quad (22)$$

$$\nabla \times \vec{H} = \vec{J} + \frac{\partial \vec{D}}{\partial t} \quad (23)$$

where  $\vec{B}$  is the magnetic field (Tesla),  $\vec{E}$  is the electric field ( $\text{V m}^{-1}$ ),  $\vec{D}$  is the induction field for the electric field, and  $\vec{H}$  is the induction field for the magnetic field,  $q$  is the electric charge density ( $\text{C m}^{-3}$ ), and  $\vec{J}$  is the electric current density ( $\text{A m}^{-2}$ ). Induction fields are defined as follows:

$$\vec{H} = \frac{1}{\mu} \vec{B} \quad (24)$$

$$\vec{D} = \varepsilon \vec{E} \quad (25)$$

where  $\mu$  is magnetic permeability ( $\text{H m}^{-1}$ ) and  $\varepsilon$  is electrical permittivity ( $\text{F m}^{-1}$ ).

The magnetic induction method is used to evaluate the current density, which is derived from Ohm's law and Maxwell's equations. Ohm's law is defined as

$$\frac{1}{\sigma} \vec{J} = \vec{E} + \vec{v} \times \vec{B} \quad (26)$$

where  $\sigma$  is the electrical conductivity ( $\text{S m}^{-1}$ ) and  $\vec{v}$  is the fluid velocity ( $\text{m s}^{-1}$ ). From (19) and (24) the induction equation becomes

$$\frac{\partial \vec{B}}{\partial t} + (\vec{v} \cdot \nabla) \vec{B} = (\vec{B} \cdot \nabla) \vec{v} + \frac{1}{\mu\sigma} \nabla^2 \vec{B}. \quad (27)$$

From the solved magnetic field,  $\vec{B}$ , the current density,  $\vec{J}$ , can be calculated using Ampere's law

$$\nabla \times \frac{\vec{B}}{\mu} = \vec{J}. \quad (28)$$

However, in the derivation of these equations, two terms appear to be neglected in the *Fluent* MHD model. The equation that should be obtained for induction is

$$\frac{\partial \vec{B}}{\partial t} + (\vec{v} \cdot \nabla) \vec{B} = (\vec{B} \cdot \nabla) \vec{v} + \frac{1}{\mu\sigma} \nabla^2 \vec{B} + \frac{1}{\sigma} (\nabla \sigma) \times \vec{E} + \frac{1}{\sigma} (\nabla \sigma) \times (\vec{v} \times \vec{B}). \quad (29)$$

The last two terms on the right side of (29) are missing from the *Fluent* MHD model. These terms are important for variable conductivity and have been tested with the help of a user-defined function (UDF) but showed no significant impact on the solution.

The magnetic field,  $\vec{B}$ , can be decomposed into the externally imposed field,  $\vec{B}_0$ , and the induced field,  $\vec{b}$ , due to fluid motion where  $\vec{B} = \vec{B}_0 + \vec{b}$ . Only the induced field  $\vec{b}$  is solved and Equation (26) becomes

$$\frac{\partial \vec{b}}{\partial t} + (\vec{v} \cdot \nabla) \vec{b} = \left( (\vec{B}_0 + \vec{b}) \cdot \nabla \right) \vec{v} + \frac{1}{\mu\sigma} \nabla^2 \vec{b} - (\vec{v} \cdot \nabla) \vec{B}_0 - \frac{\partial \vec{B}_0}{\partial t}. \quad (30)$$

It is assumed that the externally imposed magnetic field doesn't change in time so

$$\frac{\partial \vec{B}_0}{\partial t} = 0, \text{ which results in}$$

$$\frac{\partial \vec{b}}{\partial t} + (\vec{v} \cdot \nabla) \vec{b} = \left( (\vec{B}_0 + \vec{b}) \cdot \nabla \right) \vec{v} + \frac{1}{\mu\sigma} \nabla^2 \vec{b} - (\vec{v} \cdot \nabla) \vec{B}_0. \quad (31)$$

The MHD solver is initialized with a hydrodynamic solution from the CFD model. Two methods have been used for calculating the MHD solution. For the magnetostatic solution method (Soloviev et al. 2013), the velocity field from the hydrodynamic solution

is “frozen” by turning off equations for energy, flow, and multiphase and the MHD model is turned on. The MHD model is then run for 1 time-step with a time-step size of 0.001 s including 1000 iterations.

For the magnetodynamic solution, the above described method was improved upon to include the effect of self-inductance. In this method, at the time-step of interest, the MHD and CFD models are run for 500 time-steps, with a time-step size of 0.001 s including 20 iterations per time-step. Note that convergence of the MHD solution requires a stricter convergence criteria than the hydrodynamic component. The selection of the number of time-steps is based on a convergence test. The convergence time of  $500 \times 0.001s = 0.5s$  is still much less than the time for the velocity field evolution with the selected mesh grid size. With the aforementioned convergence process, the MHD model is able to account for the self-inductance phenomenon (Appendix). Nevertheless, this convergence time is not sufficient for convergence in the air. The magnetic signature above the sea surface is beyond the scope of this dissertation.

One limitation of the MHD model is that it assumes a sufficiently conductive fluid so that the charge density and displacement current terms can be neglected. The displacement current term is important for high frequency processes (*e.g.*, radio waves). This research is focused on oceanographic processes with relatively low frequencies, and the displacement term does not appear to be prominent, even in the air.

Another limitation is that the MHD model is not able to reproduce a small jump in the magnetic induction due to the relatively small difference in permeability at the interface between the air and water. Though this jump is very small, in the Earth’s magnetic field it can result in a total magnetic field difference of up to 0.2-0.3 nT. In order to account for the small difference in magnetic permeability, I have used the *ANSYS Maxwell* model, which is described next.

### **2.3. Magnetostatic model**

*ANSYS Maxwell* is an electromagnetic modeling tool, which is capable of analyzing low-frequency phenomena using finite element analysis to solve magnetic problems. Here, this software is used to explore the effect of materials with different magnetic

properties such as permeability (or susceptibility) on magnetic field deviations. *Maxwell* solves Maxwell's Equations (20) – (23) in a finite region of space with defined boundary and initial conditions. In the 3D magnetostatic solver, the Maxwell equations are as follows:

$$\nabla \times \vec{H} = \vec{J} \quad (32)$$

$$\nabla \cdot \vec{B} = 0 \quad (33)$$

$$\vec{B} = \mu_0 \cdot \mu_r (\vec{H}) \cdot \vec{H} \quad (34)$$

Magnetic permeability is the measure of the ability of a material to support the formation of a magnetic field within itself or the degree of magnetization that a material obtains in response to an applied magnetic field. Relative permeability,  $\mu_r$ , is the ratio of the permeability of some material to the permeability of the free space:  $\mu_r = \frac{\mu}{\mu_0}$ .

Magnetic susceptibility  $\chi_m$  is related to magnetic permeability as follows:  $\chi_m = \mu_r - 1$ . It is indicative of whether a material is attracted to or repelled from a magnetic field. Paramagnetic materials form internal, induced magnetic fields in the direction of the applied magnetic field, while diamagnetic materials form induced magnetic fields in the direction opposite to that of the applied magnetic field (Miessler and Tarr 2010). Different materials can have different magnetic permeabilities. For example, air is a paramagnetic material, while water is a diamagnetic material. These different magnetic material properties can affect the Earth's magnetic field near the interface of the two materials. In this work, I use *ANSYS Maxwell* to explore how differences in these magnetic properties between materials affect the Earth's magnetic field near their interface. This model is verified with a laboratory experiment (see Section 3.5).

*ANSYS Maxwell* is well-suited to simulate the effect of magnetic permeability differences at the interface of two materials with different permeabilities (e.g., air and water). However, due to the limitations of *ANSYS Maxwell*, motion can only be translational or rotational. Therefore, this model is unable to account for the velocity field in the ocean, including surface and internal waves.

Neither of the two magnetic models, *ANSYS Fluent* MHD or *ANSYS Maxwell*, is able to describe both the magnetic signature of velocity field in a conducting media and the difference of magnetic permeability of different materials. Each model has advantages and disadvantages, therefore the combination of these two models may compensate, at least partially, for their disadvantages.

### **3. Model verifications**

To quote Box and Draper (1987): “all models are wrong, but some are useful.” This essentially means that all models must make some simplifications/approximations to simulate our complex, non-linear world. In order to be sure that these simplifications do not result in artifacts, the model must be verified. The models developed in this work are compared with known analytical solutions of surface (Section 3.1) and internal waves (Section 3.2). Related boundary effects are discussed in Section 3.3. The models are also verified with field measurements (Section 3.4) and a laboratory experiment (Section 3.5). The results of this work are summarized in Section 3.6.

#### **3.1 Comparison of MHD model with known analytical solutions of surface waves**

Weaver (1965), Beal and Weaver (1970), and Podney (1975) developed analytical models for the magnetic field generated by surface and internal waves in the ocean and in the air above the ocean surface. In this section, the *ANSYS Fluent* MHD model is compared with these known analytical models.

Weaver (1965) considers the magnetic fields generated by ocean swell and wind-driven waves and concludes that ocean swell is as important of a generating mechanism of magnetic signatures as local wind-waves of a greater amplitude. Therefore, in the open ocean, magnetic signals may be significant even in calm seas due to ocean swell. Weaver (1965) assumes that the air and seawater have a negligible difference in permeability and that the ocean bottom has no effect. Based on these assumptions, Weaver (1965) calculated the component of the magnetic field of the Earth,  $F$ , that is measured by a total field magnetometer in the ocean as

$$|h_{\parallel}| = (\pi a \sigma F / \omega) (S^2 + C^2) \left[ S^2 (g + 2d\omega^2)^2 + C^2 (g - 2d\omega^2)^2 \right]^{1/2} e^{-d\omega^2/g} \quad (35)$$

and in the air as

$$h'_{\parallel} = (\pi a \sigma F g / \omega) (S^2 + C^2) e^{-s\omega^2/g}, \quad (36)$$

where  $h_{\parallel}$  and  $h'_{\parallel}$  are the horizontal components of the magnetic field in the water and air, respectively;  $a$  is the amplitude of the ocean wave at the surface,  $\sigma$  is electrical conductivity,  $\omega$  is angular frequency of the ocean waves,  $g$  is gravity,  $d$  is depth,  $s$  is the altitude above the sea,  $S = \sin I$ ,  $I$  is the dip angle,  $C = \cos I \cos \theta$ ,  $\theta$  is the eastward inclination of the direction of wave propagation from the magnetic meridian. For these calculations, typical values of Earth's constant magnetic field,  $F$ , and dip angle,  $I$ , for midlatitudes in the northern hemisphere were used and the waves were traveling in the direction of magnetic north. Equations (35) – (36) follow from Maxwell's electromagnetic theory with some unavoidable assumptions due to the analytical nature of this model.

Weaver (1965) assumed that "...applying the conditions that normal and tangential magnetic field components must be continuous across the air-sea boundary." However, a subsequent work (Podney 1975) stated that "...transverse magnetic type fields vanish above an ocean surface" and only the normal component of the magnetic induction is continuous at the air-water interface. There is apparently a contradiction between these two papers regarding the magnetic field in the air.

The above analytical solution by Weaver (1965) was reproduced using the *ANSYS Fluent* MHD model. The domain for this simulation was 500 m long by 250 m wide by 500 m deep, with a mesh resolution of 2 m in the horizontal and 0.14 m in the vertical at the air-sea interface, expanding to 3 m at the top (of the air layer) and bottom of the domain. This is a two-phase, Volume of Fluid model (see, Section 2.1) with air (top 250 m) and water (bottom 250 m) layers. The velocity field was initialized using a UDF to set the  $u$  and  $w$  components of orbital velocities of the surface waves for a flat ocean surface, which allowed for comparison with Weaver's (1965) analytical solution (that implied a flat ocean surface). The velocity of surface waves were defined as follows:

$$u = A\omega \frac{\cosh(k(H+z))}{\sinh(kH)} \cos(kx - \omega t), \quad w = A\omega \frac{\sinh(k(H+z))}{\sinh(kH)} \sin(kx - \omega t) \quad (37)$$

where  $A$  is wave amplitude,  $\omega$  is the wave frequency,  $H$  is the height of the water layer,  $z$  is depth, and  $k$  is wavenumber (Phillips 1977). The simulation was run for 5 s period surface waves. Figures 7 and 8 show the initial velocity condition in the water for the MHD simulation, according to Equation (37). The velocity was initialized to 0 m/s in the air. The MHD solver is initialized with the hydrodynamic solution from the CFD model. The computational procedure is described in Section 2.2.

In the Weaver (1965) analytical solution, the orbital velocity of the wave is fixed; while, the *Fluent* solution evolves after initialization according to the Navier-Stokes equations, which resulted in some decay of the orbital velocity with time. Due to the relatively short period of surface waves (5 s), the velocity field in the *Fluent* model evolved by approximately 29% during the 0.5 s convergence time of the magnetohydrodynamic solution implemented in this work, which is corrected in the magnetic solution by multiplying by a factor of 1.29. (Note that this effect is negligible for internal waves due to their much longer periods.)

To be consistent with Weaver (1965), the surface wave direction was in the direction of magnetic north. The Earth's magnetic field was set as follows:  $B_x = 1.71 \times 10^{-5}$  T,  $B_y = 0$  T,  $B_z = -4.698 \times 10^{-5}$  T, corresponding to 70°N latitude. The electrical conductivity of water and air were set to 4 S/m and  $5.5 \times 10^{-15}$  S/m, respectively. The bottom and top of the domain had a conducting boundary conditions with conductivity of 0.4 S/m and  $5.5 \times 10^{-15}$  S/m, respectively. Figure 9 shows the comparison of the amplitude of the magnetic field fluctuations produced by the MHD model with the analytical solution of Weaver (1965). Though Weaver's (1965) solution resulted in 1-D (vertical) magnetic profiles; technically, this model is 2-D. In order to ensure that the 3-D *Fluent* MHD was comparable with Weaver's (1965) results, both 2-D and 3-D simulations were conducted. It appears that both the 2-D and 3-D *Fluent* MHD models are consistent with the analytical model in the water column (Fig. 9).



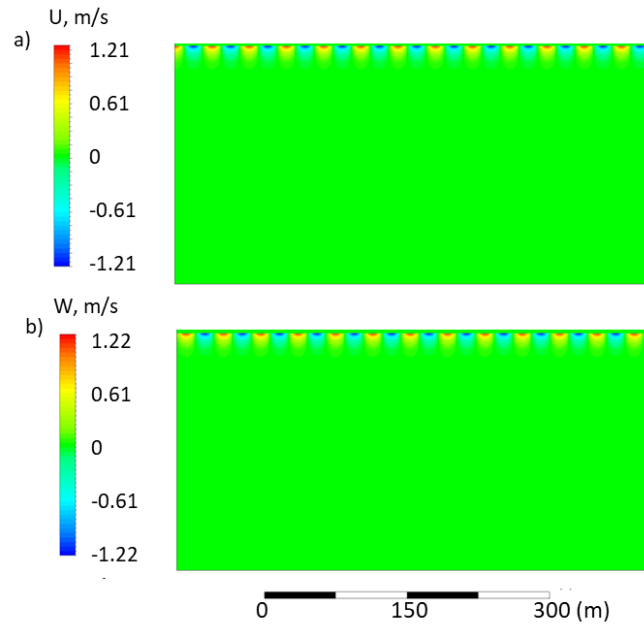


**Figure 7.** Orbital velocity of 5 s period surface waves (under the assumption of a flat surface) following Weaver (1965). a) Contour plot on the center plane of the numerical domain of  $u$  and b)  $w$  velocities in the water layer applied for the initialization of the *Fluent* MHD model.

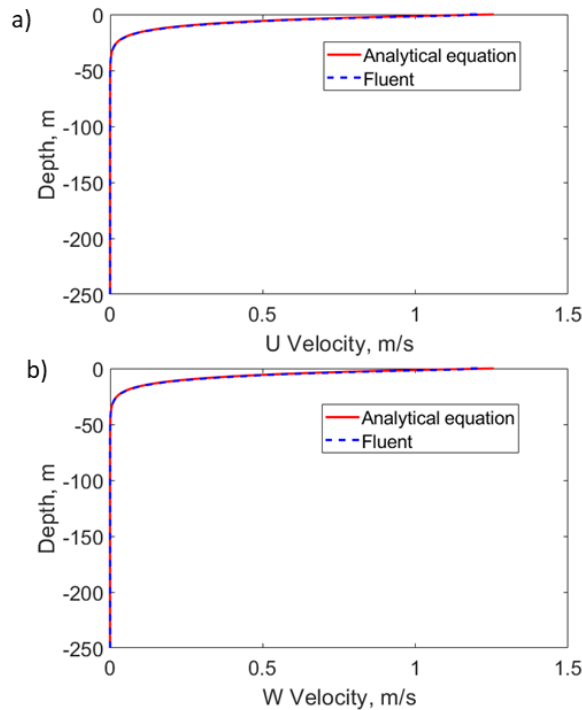


**Figure 8.** The amplitude of velocity components calculated from the values on center plane of the numerical domain of a)  $u$  and b)  $w$  orbital velocities of a 5 s period surface waves compared to Equation (37).

The boundary effects at the sides of the numerical domain in the horizontal direction have been removed in the calculation of the vertical profile shown in Figure 9, by removing 150 m from either side of the domain. There are some boundary effects near the top and bottom of the numerical domain, but the magnetic signatures at these locations are far below the level that can be measured with current magnetometers. The boundary effects at the top and bottom of the numerical domain will be considered in more detail in Section 3.3.

As mentioned above, there is a contradiction between the traditional models (Weaver 1965, Podney 1975) about the magnetic field at the air-sea interface, which has not been resolved. (Due to the lack of sufficient details in Weaver (1965) and Podney (1975), I have not been able to resolve it either.) Therefore, comparison of the *Fluent* MHD model results with the analytical model solutions in the air is not feasible.

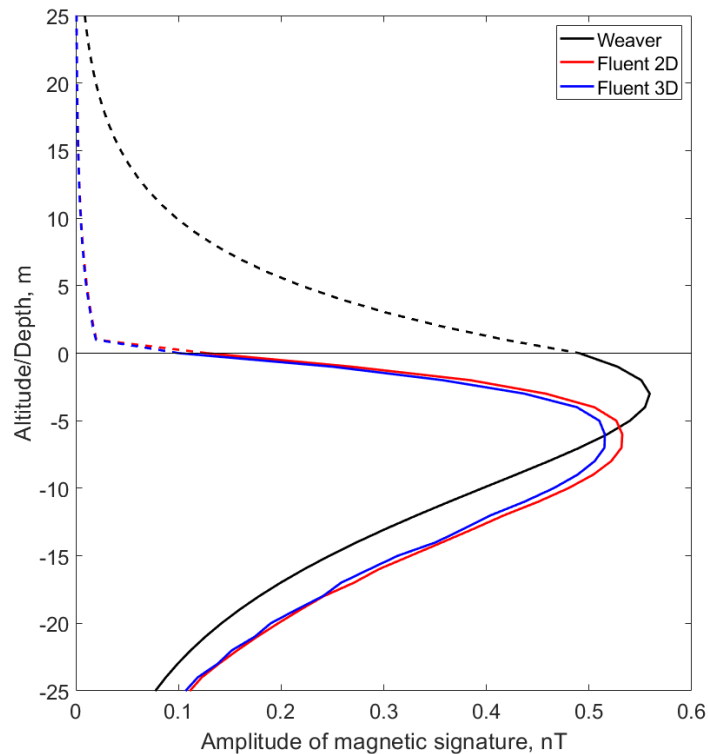


**Figure 9.** Magnetic signature of 5 s surface wave from the center plane of the *Fluent* MHD model compared to Weaver (1965) analytical solution zoomed to the depth/altitude near the air-sea interface on a linear scale.

### 3.2 Comparison of MHD model with known analytical solutions of internal waves

An additional *Fluent* MHD model verification was conducted for the case of internal waves, using Beal and Weaver (1970) analytical solution for comparison. Beal and Weaver (1970) consider the magnetic fields generated by internal waves with periods between 1 – 30 minutes in a two-layer ocean with an infinite depth and uniform conductivity. They determine that this signal is less important than that produced by ocean swell. Beal and Weaver (1970) calculated the components of the magnetic signature produced by the internal waves with a 1% density difference between the two ocean layers. Respectively, the x and z components of the magnetic field produced by deep-water internal waves in the ocean layer above the internal wave interface in Beal and Weaver's model were

$$|h_x| = Ae^\zeta \left\{ C^2 \zeta^2 + S^2 (1 + \zeta)^2 \right\}^{1/2}, \quad |h_z| = Ae^\zeta \left\{ S^2 \zeta^2 + C^2 (1 - \zeta)^2 \right\}^{1/2} \quad (38)$$

and in the layer below the internal wave interface,

$$|h_x| = Ae^{-\zeta} \left\{ C^2 \zeta^2 + S^2 (1 - \zeta)^2 \right\}^{1/2}, \quad |h_z| = Ae^{-\zeta} \left\{ S^2 \zeta^2 + C^2 (1 + \zeta)^2 \right\}^{1/2}, \quad (39)$$

where  $A = 2\pi a \sigma F \left\{ g(\alpha - 1) / k(\alpha + 1) \right\}^{1/2}$ ,  $\zeta = k(z - d)$ ,  $\alpha = \rho_1 / \rho_2 = 1.01$ ,  $a$  is the amplitude of the ocean wave at the interface. For these calculations, typical values of Earth's constant magnetic field,  $F$ , and dip angle,  $I$ , for midlatitudes in the northern hemisphere were used and the waves were traveling in the direction of magnetic north. Equations (38) – (39) follow from Maxwell's electromagnetic theory with some unavoidable assumptions due to the analytical nature of the model.

To simulate the internal wave case from Beal and Weaver (1970), the velocity field was initialized using a UDF to set the u and v components of orbital velocities of the internal waves centered at 100 m depth to compare with the analytical solution for a flat interface. The velocity of internal waves were defined as follows (see Section 1.2):

$$u_1 = -A\omega \frac{\cosh(kz)}{\sinh(kh_1)} \cos(kx - \omega t), \quad w_1 = -A\omega \frac{\sinh(kz)}{\sinh(kh_1)} \sin(kx - \omega t) \quad (40)$$

$$u_2 = A\omega \frac{\cosh(k(H+z))}{\sinh(kh_2)} \cos(kx - \omega t), \quad w_2 = A\omega \frac{\sinh(k(H+z))}{\sinh(kh_2)} \sin(kx - \omega t) \quad (41)$$

for the upper layer and the lower layer, respectively, where  $h_1$  is the height of the upper layer and  $h_2$  is the height of the lower layer (Massel 2015). In this case  $h_1 = 100 \text{ m}$  and  $h_2 = 150 \text{ m}$ . Note that for comparison with Beal and Weaver (1970), the interface between the upper and lower layers is set to be flat in the *Fluent* model as well.

A 50 m wavelength was chosen for verification of the analytical model, which corresponds to a deep water wave. Figures 10 and 11 show the initial velocity condition in the water for the MHD simulation with a 50 m long internal wave. The velocity field was initialized to 0 m/s in the air.

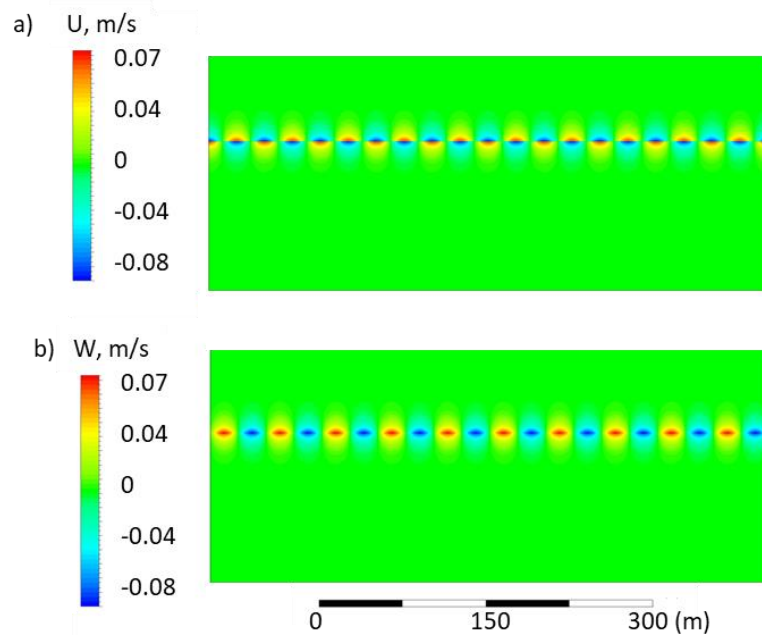


**Figure 10.** Orbital velocity of 50 m long internal wave. (under the assumption of a flat interface) following Beal and Weaver (1970) a) Contour plot on the center plane of the numerical domain of  $u$  and b)  $w$  velocities in the water layer applied for the initialization of the *Fluent* MHD model.

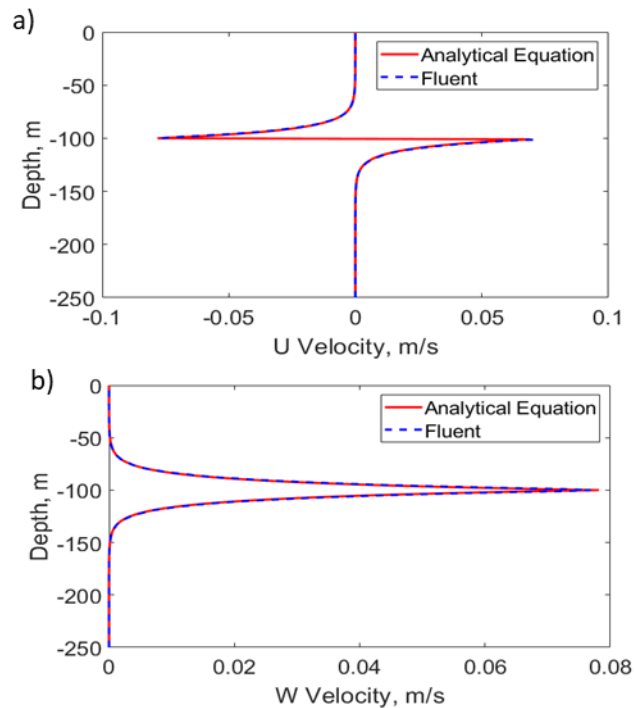


**Figure 11.** The amplitude of velocity components calculated from the values on center plane of the numerical domain of a)  $u$  and b)  $w$  orbital velocities of a 50 m long internal wave compared to Equations (40) – (41).

The analytical model of Beal and Weaver (1970) for internal waves is based on Weaver’s (1965) model for surface waves, which was considered above. Figure 12 shows the comparison of the *Fluent* MHD model results with the analytical model. The *Fluent* MHD model setup was the same as in the surface waves case. The *Fluent* MHD shows remarkably consistent results with the analytical model for the 50 m long internal wave (Fig. 12). Since a 50 m internal wave can be classified as a deep water wave, the boundary effects at the air-sea interface and at the seafloor are negligible. Note, horizontal boundary effects have been removed in this analysis by removing 100 m from either side of the numerical domain in the calculation of the amplitude of the magnetic signature in the same way as the analysis of surface waves.

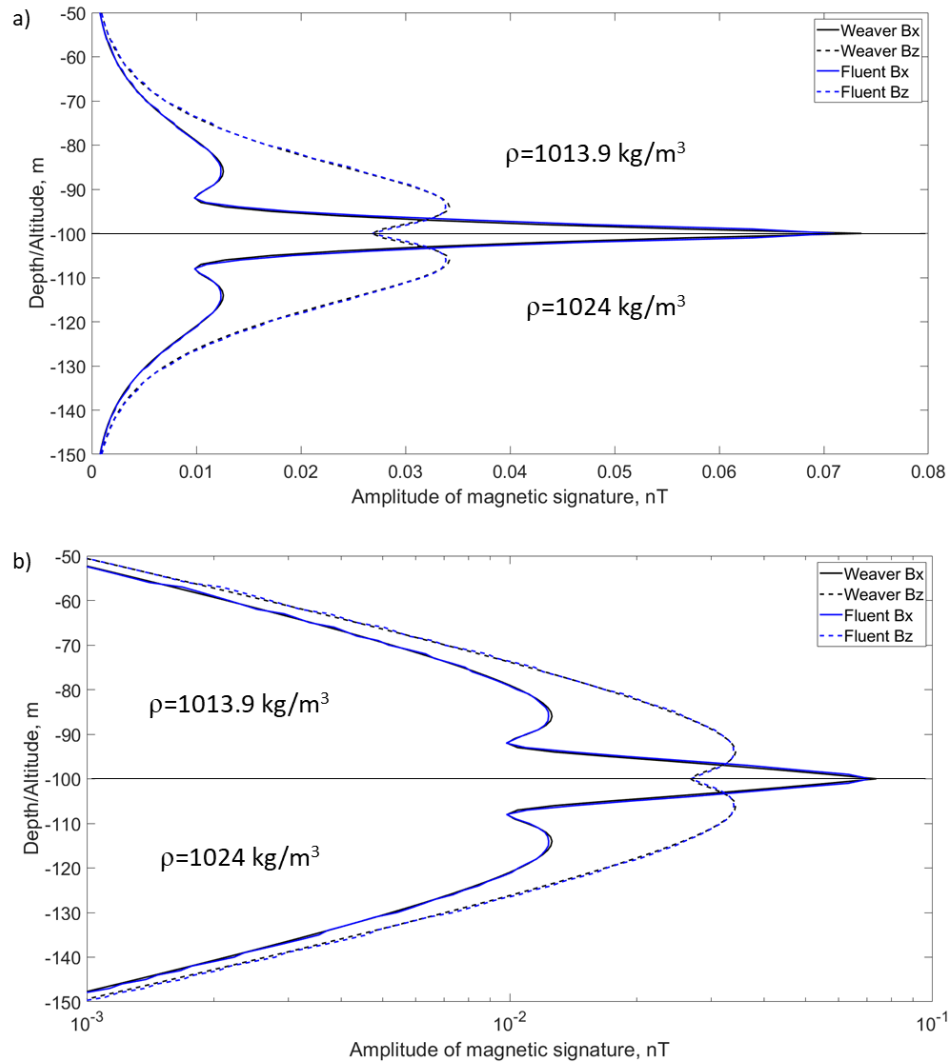


**Figure 12.** Magnetic signature of 50 m internal wave from the center plane of the compared to Beal and Weaver (1970) analytical solution. a) Zoomed into the area of the internal wave interface on a linear scale, b) zoomed near the internal wave interface on a semi log scale. The horizontal line indicates the wave interface.

The orbital velocities of deep water internal waves have practically no interaction with the seafloor. For these short waves, the *Fluent* model produces results that are remarkably similar to that of the analytical models. Based on these results, I conclude that the *Fluent* MHD compares well with the analytical solution in the water column for deep water waves. When the waves become longer, there is interaction of the wave orbital velocities with the boundaries and the Beal and Weaver (1970) analytical model becomes questionable. The shallow water waves interact with the bottom and surface of the ocean.

### 3.3 Boundary Effects

One factor, which may affect the magnetic signature of internal shallow water waves near the seafloor, is hydrodynamic boundary layer effects. Shallow water internal waves produce convergence/divergence patterns near the seafloor with relatively large shear, which may enhance the magnetic signature of internal waves. Figures 13 and 14 demonstrate the effect of the addition of a 10 m thick bottom boundary layer for a 500 m and a 1000 m idealized internal wave, respectively. Both linear and logarithmic horizontal velocity profiles were tested, though the difference is not substantial.

For 500 m and 1000 m long internal waves, there is a substantial difference between the Beal and Weaver (1970) analytical solution and the *Fluent* MHD solution (Figures 13 and 14). Since these are shallow water waves, Beal and Weaver (1970) use the shallow water approximation in their model. At the same time, the *Fluent* MHD model solves for the magnetic field in the entire domain and no additional assumptions about shallow or deep water waves are involved in the solution. Further comparison of the *Fluent* MHD model with the Beal and Weaver (1970) analytical solution with respect to the field measurements can be found in Section 3.4.

The logarithmic velocity profile for the u component was determined by the following equation:

$$u(z') = \frac{u_*}{\kappa} \ln \left( \frac{z'}{z_0} \right) \quad (42)$$

where  $u_*$  is friction velocity,  $\kappa$  is the Karman constant,  $z_0 = 0.01m$  is the surface roughness. At the top of the logarithmic velocity layer (10 m above the seafloor) the u velocity is defined as

$$u(z'_0) = \frac{u_*}{\kappa} \ln \left( \frac{z'_0}{z_0} \right), \quad (43)$$

and, therefore,

$$u_* = u(z'_0) \kappa \ln \left( \frac{z'_0}{z_0} \right), \quad (44)$$

where  $z'_0 = 10m$  is the height of the logarithmic velocity layer. By plugging Equation (44) into Equation (42) and using the internal wave velocity profile in the bottom layer (Equation 41), the velocity profile in the bottom 10 m of the domain is defined as follows:

$$u(z') = \frac{u(z'_0)}{\ln \frac{z'_0}{z_0}} \ln \left( \frac{z'}{z_0} \right) = A\omega \frac{\cosh(k(H+z))}{\sinh(kh_2)} \frac{1}{\ln \frac{z'_0}{z_0}} \ln \frac{250+z}{z_0} \cos(kx - \omega t), \quad (45)$$

where  $z'$  is the height above the bottom in the logarithmic velocity layer. The  $w$  component of velocity profile in the boundary layer was calculated as a linear interpolation from 10 m height above the bottom, which may not exactly satisfy the continuity equation.

The addition of the velocity profile due to the presence of the bottom boundary layer resulted in an increase of the amplitude of the total magnetic field fluctuations predicted by the *Fluent* MHD model by a factor of 2.3 and 3.5 for the 500 m (Fig. 13) and 1000 m (Fig. 14) idealized internal waves, respectively.

The addition of a boundary layer appears to be important for the generation of the magnetic signature of oceanographic processes near the seafloor. Incorporation of the bottom boundary layer effects is necessary for modeling of the magnetic signature of these processes. This is especially critical for the field measurements analyzed in Section 3.4 since the magnetometers are located approximately 1 m above the seafloor. More details on these measurements and the MHD model based on them can be found in Section 3.4.



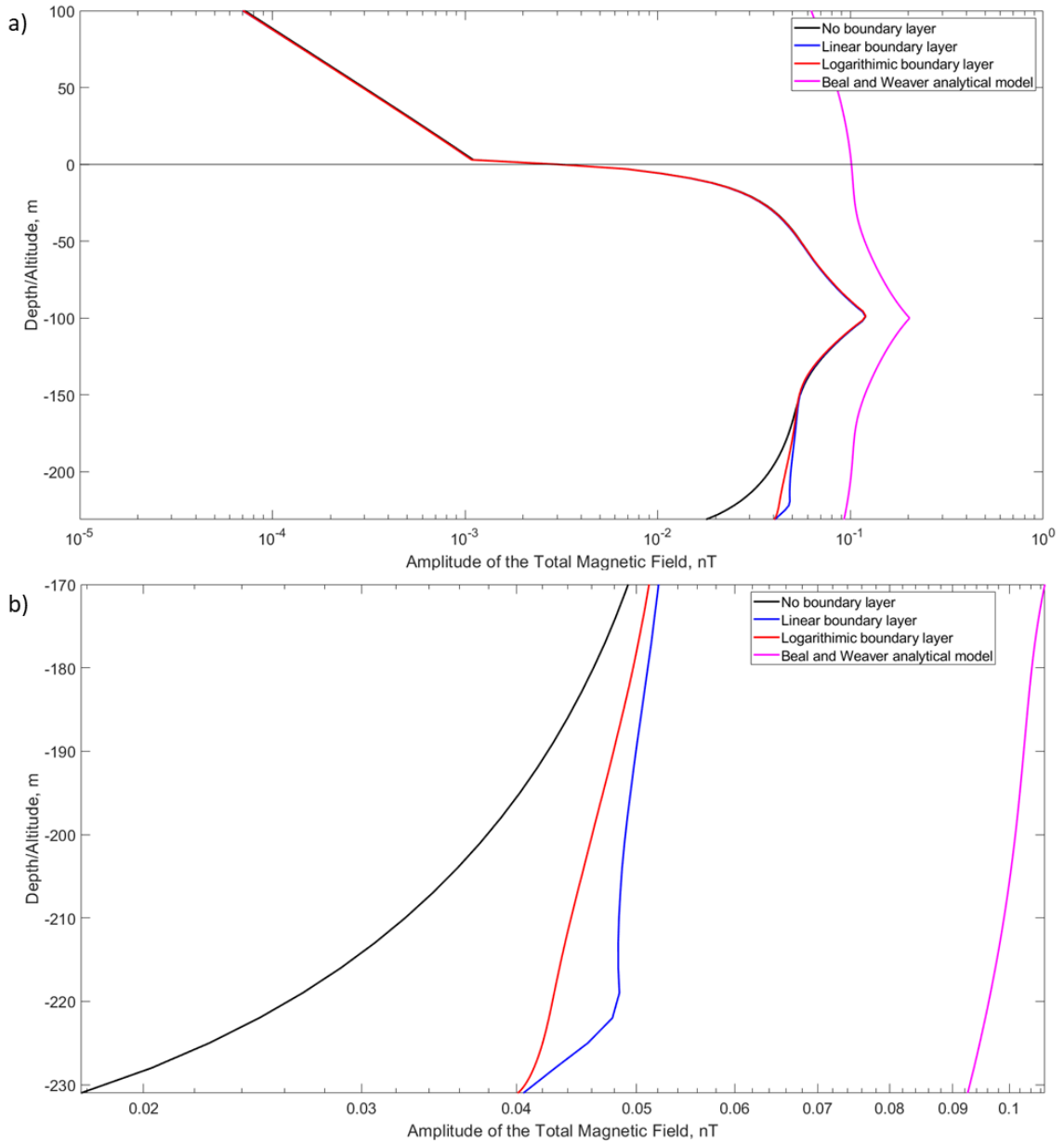


**Figure 13.** (a) Magnetic signature of 500 m long internal wave with different seafloor and boundary conditions from the center plane of the *Fluent* MHD in comparison with Beal and Weaver’s (1970) analytical model, (b) near-bottom area shown in more detail. Note that the traditional Beal and Weaver (1970) model does not appear to be consistent with the measurements (Section 3.4).

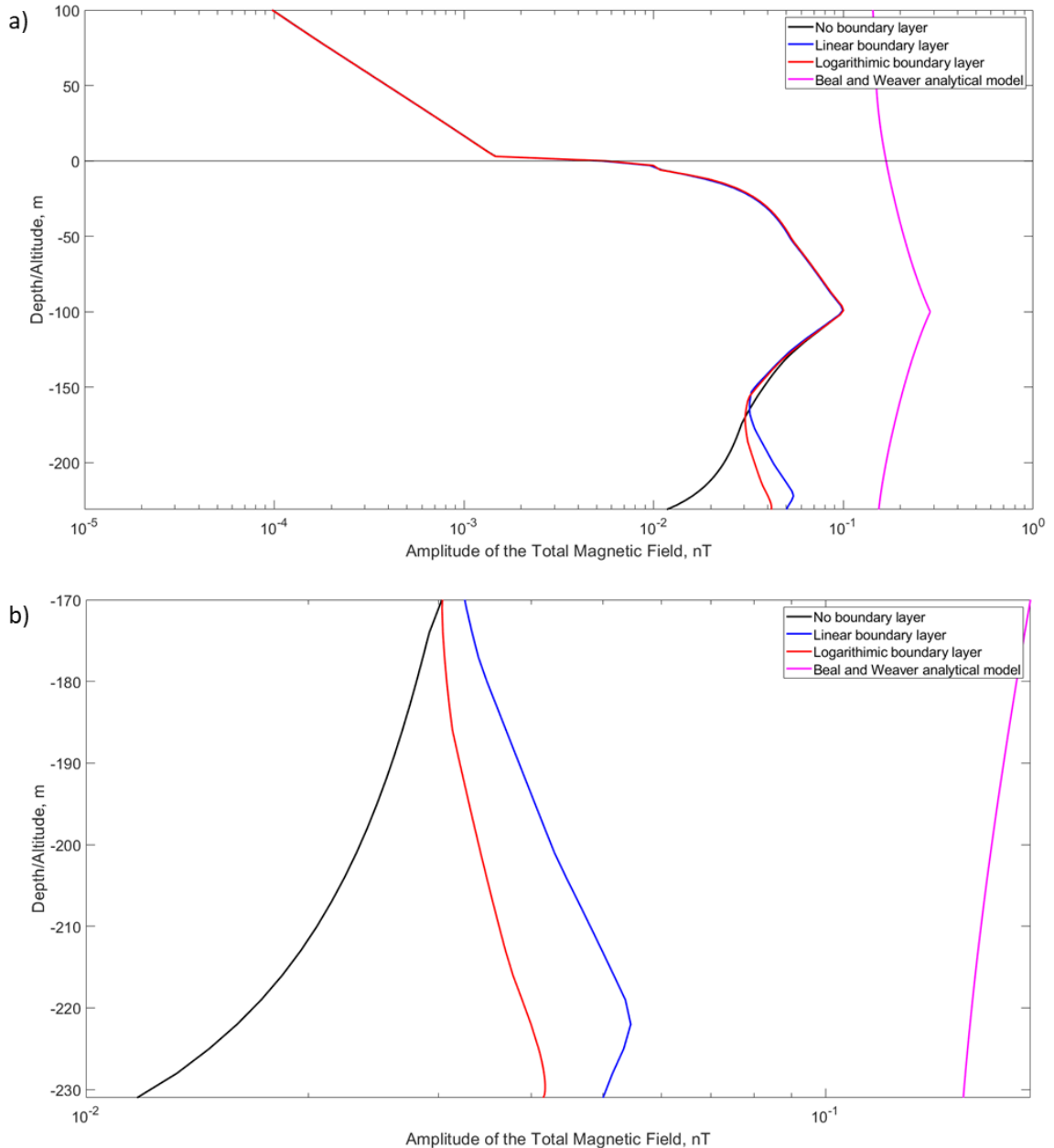


**Figure 14.** (a) Magnetic signature of 1000 m long internal wave with different seafloor and boundary conditions from the center plane of the *Fluent* MHD compared to the Beal and Weaver (1970) analytical solution, (b) near-bottom area shown in more detail.

### 3.4 Model verification in oceanic conditions

Further verification of the MHD model was done applying the model used in Section 3.1 and 3.2 to the case of internal wave solitons measured by NSWCCD during the Ambient Weather Experiment at the EM Observatory. Velocity and total magnetic field

were measured during this experiment using two magnetometer/ADCP pairs. The internal wave solitons observed on 30 April 2017 and 3 May 2017 are analyzed here in detail (Figs. 16 and 20).

In a stratified ocean having a Brunt-Väisälä frequency profile,  $N(z)$ , the vertical component of the vector profile of velocity of a progressive wave, is a solution of the integral equation (Podney 1975)

$$v_z(z) = \frac{1}{\tilde{\omega}^2} \int_0^D \tilde{N}^2(\zeta) v_z(\zeta) G(\zeta, z) k d\zeta + v_{z0} \frac{\sinh(k(D-z))}{\sinh(kD)} \quad (46)$$

where  $G(\zeta, z) = \frac{\sinh(k\zeta)\sinh(k(D-z))}{\sinh(kD)}$ ,  $\zeta \leq z$ ,  $\tilde{\omega}^2 = \omega^2 - \Omega^2$ ,  $\tilde{N}^2(z) = N^2(z) - \Omega^2$ ,

$\omega$  is the angular frequency,  $\Omega$  is the local vertical component of the Earth's rotation vector,  $k$  is wavenumber,  $v_{z0}$  is the velocity at the free-surface, and  $D$  is the depth of the internal wave interface (Cox 1962).

Internal wave solitons can often be represented in a two-layer approximation. In this case, the ocean stratification can be represented by two homogenous layers with a density discontinuity at an interface; as a result, the Brunt-Väisälä frequency disappears from Equation (46), and the hydrodynamic eigenfunctions decay exponentially (Chave 1984). For a two-layer ocean of finite depth, the solution for the vertical component of the orbital velocity of a soliton is as follows:

$$v_x = v_{x0} \frac{\cosh(k(D+z))}{\sinh(kD)} \quad (47)$$

As a first approximation, this equation can be significantly simplified if  $\lambda \ll 2\pi D$ ,

$$v_x(z) = v_{x0} \frac{\cosh(k(D-z))}{\sinh(kD)} \approx e^{-kz}. \quad (48)$$

The measurements from the ADCPs are in the temporal domain, while the CFD modeling is conducted in the spatial domain. The wavelength of the internal wave soliton is a necessary parameter to be able to properly model the magnetic signature of these

processes. Therefore, the temporal data from ADCPs have to be transformed into the spatial domain. For this purpose, we will use exponential decay of the horizontal component of the orbital velocity, as follows from the theoretical Equation (48).

The slope of the linear polynomial interpolation of this decay in a semi log scale gives an estimated wavenumber of the internal wave soliton (Fig. 15). The wavenumber was calculated for both ADCP Nodes at the crest and trough of the internal wave for both 30 April and 3 May (Table 1).

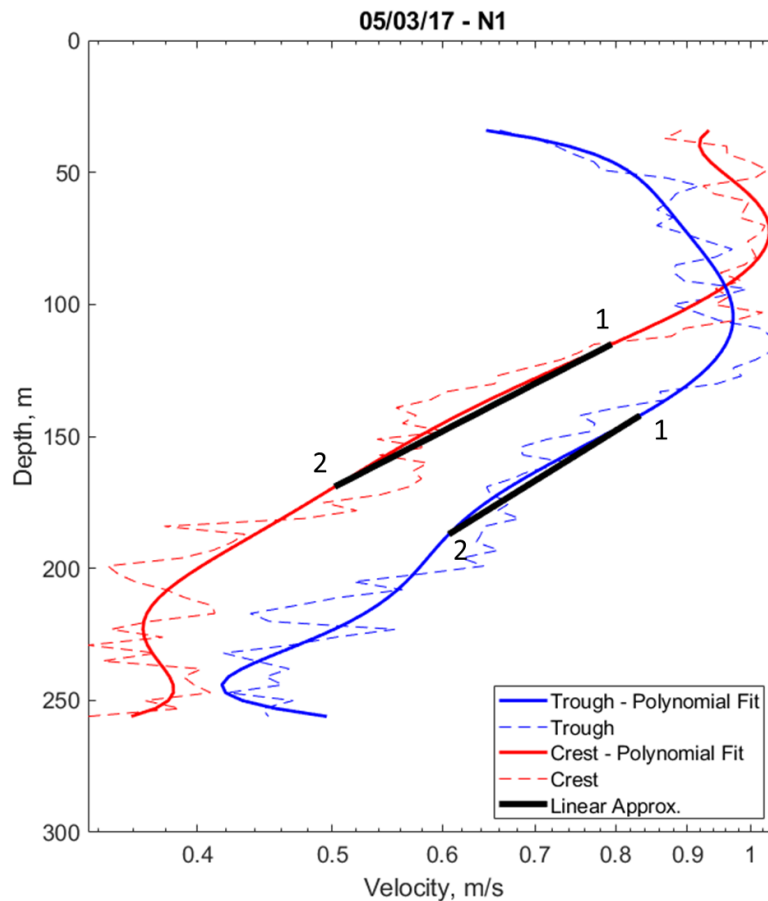


**Figure 15.** Example of wavenumber calculation from 30 April 2017 Node 1 ADCP northward velocity during internal wave soliton passing. The dashed lines are the initial data, the solid lines are the 7<sup>th</sup> order polynomial fit to the data. The red lines are from the time that the wave crest passed over the ADCP. The blue lines are when the trough passed over the ADCP, and the black lines are the linear interpolations used to calculate wavenumber.

Two cases (30 April and 3 May) were modeled with the *Fluent* MHD model and compared with the magnetic measurements. On 30 April, the wavelength was

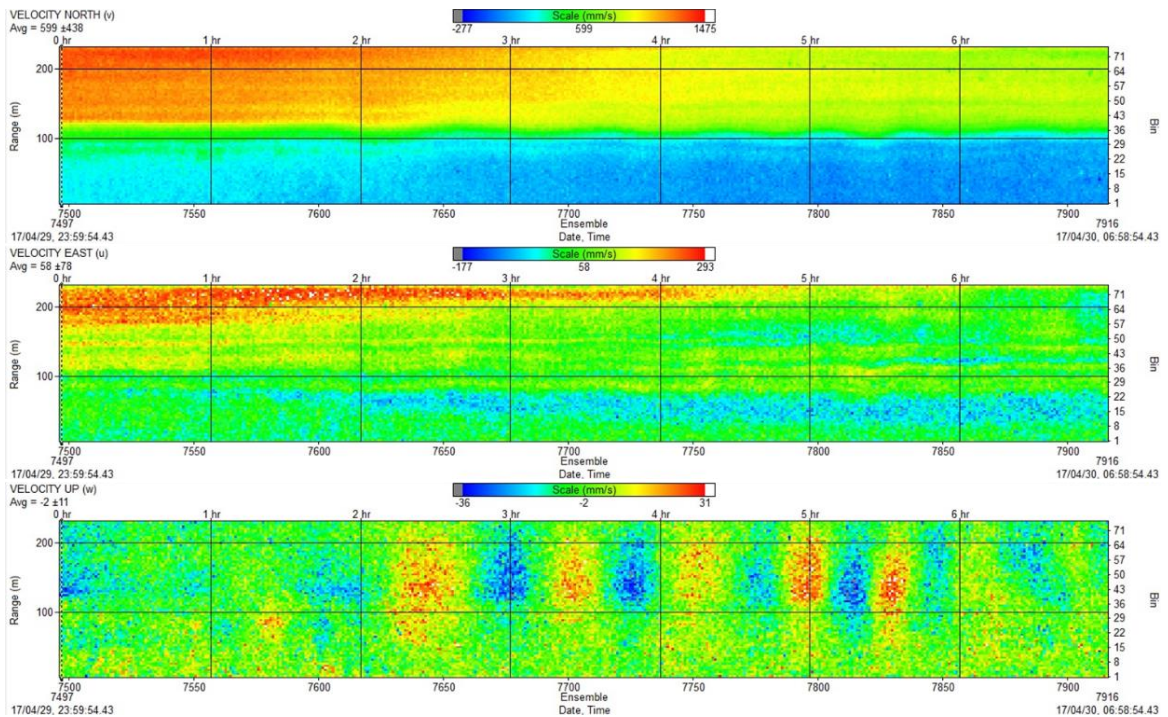
approximately 465 m (Fig 16). A 15,717 m long numerical domain was designed using the internal wave soliton wavelength as the length scale for conversion of the temporal to spatial scale. The domain was 120 m wide, with a 231 m water layer, and 250 m thick air layer. The height of the air layer was approximately one-half of the internal wave soliton wavelength. The mesh resolution was 3 m in the vertical (to match the ADCP resolution) and 23.25 m in the horizontal. The horizontal size of the mesh corresponded to one ensemble of the ADCP measurement. On 3 May, the internal wave soliton with a wavelength approximately 1190 m was observed (Fig 20). Respectively, the domain was designed with the following dimensions: 14,552 m long, 120 m wide, with a 231 m water layer, and 600 m thick air layer. The mesh resolution was 3 m in the vertical and 34 m in the horizontal.

**Table 1.** Wavenumber calculation for internal wave solitons observed during the 2017 Ambient Weather Experiment.

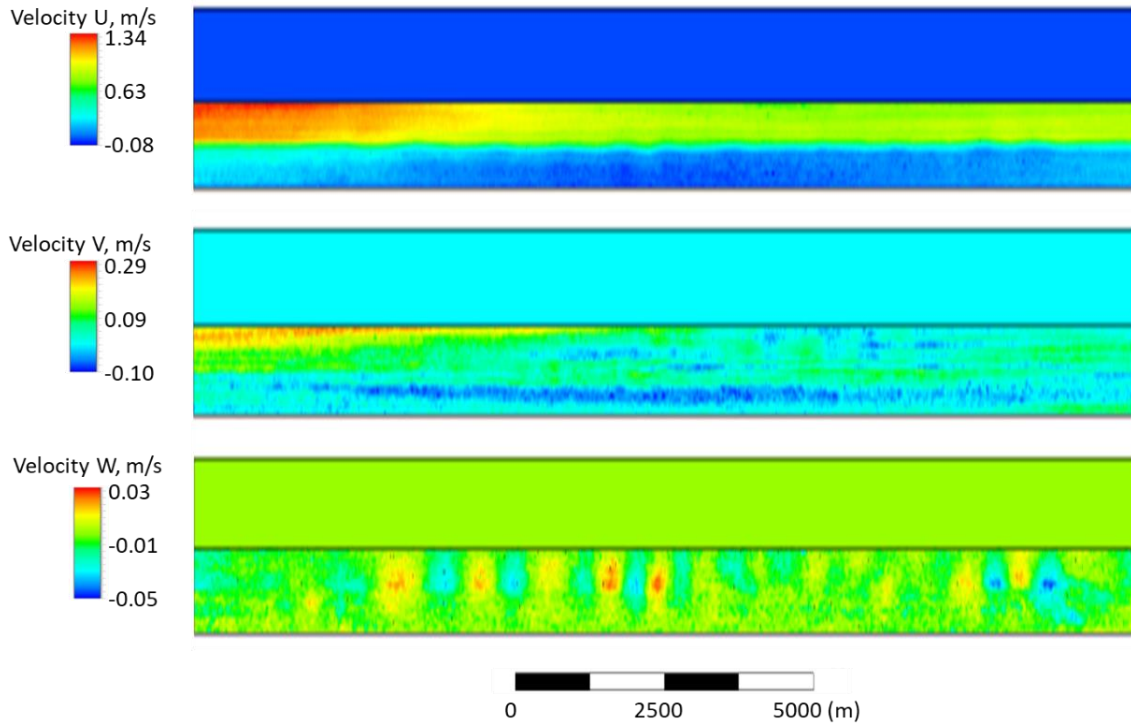
Date	Node	Crest/ Trough	Ensemble	Depth 1 (m)	Depth 2 (m)	Vel 1 (m/s)	Vel 2 (m/s)	Wavenumber (1/m)	Wave Length (m)
April 30	1	Crest	567	132.6	174.6	0.638	0.0723	0.0135	466.57
April 30	1	Trough	587	147.6	177.6	0.540	0.1318	0.0136	461.43
April 30	3	Crest	519	130.4	175.4	0.641	0.0875	0.0132	476.60
April 30	3	Trough	538	139.4	178.4	0.598	0.1038	0.0127	495.84
May 3	1	Crest	196	115.1	169.1	0.794	0.5023	0.0054	1161.6
May 3	1	Trough	161	142.1	187.1	0.833	0.6067	0.0050	1215.1
May 3	3	Crest	214	115.5	166.5	0.791	0.4885	0.0059	1058.3
May 3	3	Trough	172	133.5	181.5	0.814	0.5503	0.055	1142.8

The CFD model was initialized with the velocity field measured at the EM Observatory (Figs. 17 and 21). Due to the lack of information on the 3D velocity field, the model has been initialized under the assumption that the internal wave soliton

propagates in the x-direction. As a result, there is no spatial variability of the velocity field in the y-direction. For both cases, the velocity measurements began at approximately 7 m above the seafloor. Below this level, the vertical mesh resolution was increased to 0.25 m and logarithmic velocity profiles for the horizontal components of velocity were implemented. Note, that the vertical component of velocity was linearly interpolated to the seafloor, which may not completely satisfy the continuity equation. For both cases, the MHD model was initialized with the Earth's constant magnetic field at the location of the measurements ( $B_x=2.53 \times 10^{-5}$  T,  $B_y=2.99 \times 10^{-6}$  T,  $B_z=-3.6 \times 10^{-5}$  T). The conductivities of the water and air were set at 4.788 S/m,  $5.5 \times 10^{-15}$  S/m, respectively. The permeability of the air and water were set at  $1.257 \times 10^{-6}$  H/m.

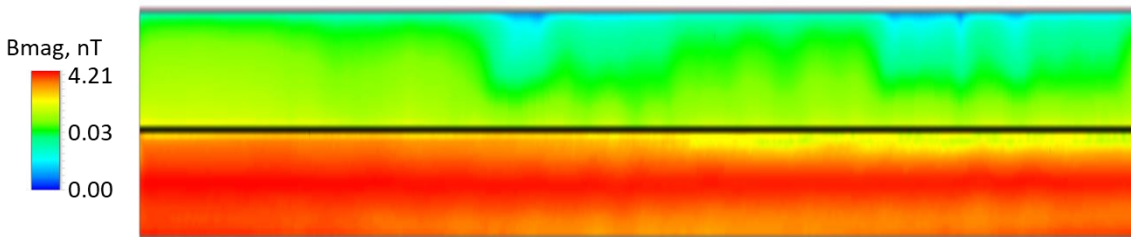


**Figure 16.** The velocity field on 30 April 2017 during the Ambient Weather Experiment measured by NSWCCD. The top, middle, and bottom plots show northward, eastward, and vertical velocity components, respectively. All scales are in mm/s.



**Figure 17.** Contour plot on the center plane of the velocity field initialization of the model on 30 April from the field measurements. The domain includes air and seafloor layers. The top, middle, and bottom plots show northward, eastward, and vertical velocity components, respectively. The horizontal line indicates the air-sea interface.

The MHD model was initialized with the velocity field from the 30 April measurements. Figure 18 shows the magnetic signature produced by the MHD model.



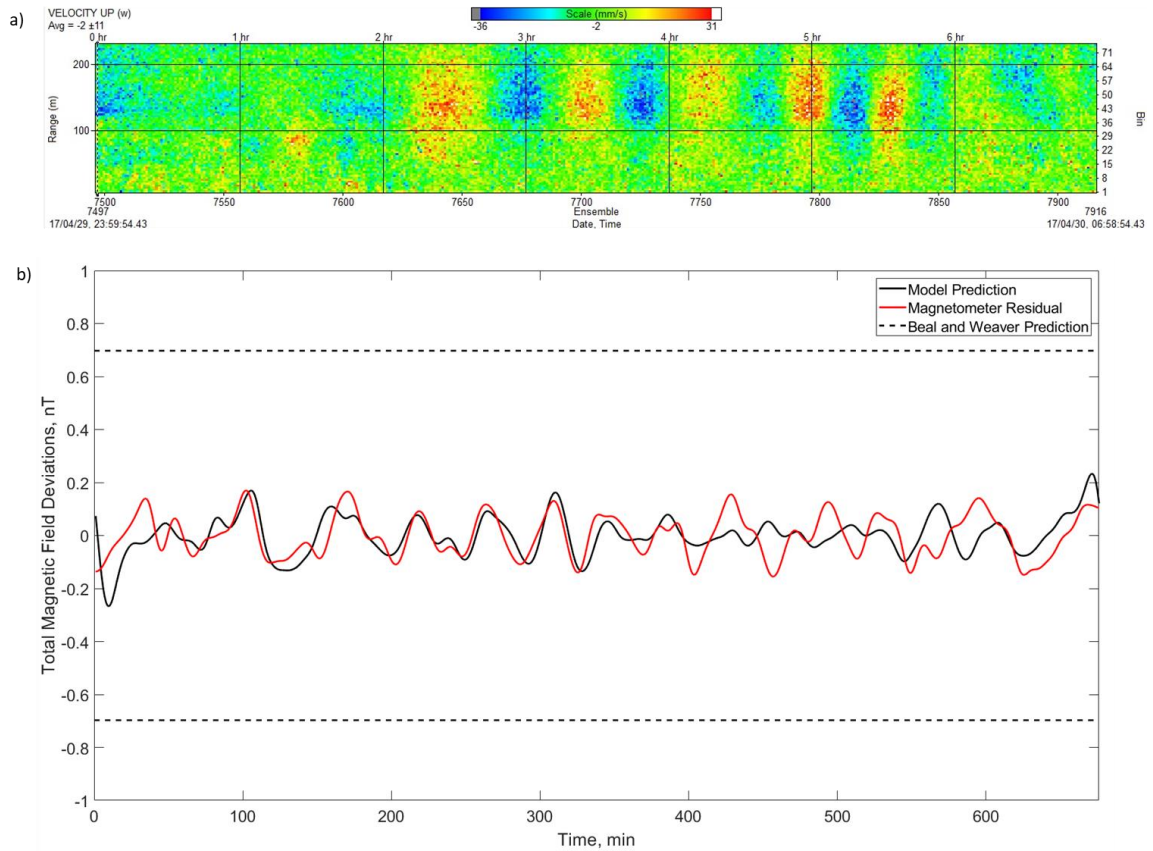
**Figure 18.** Contour plot on the center plane of the magnitude of the modeled magnetic field fluctuations induced by the velocity field on 30 April shown in log scale. The horizontal black line indicates the air-sea interface.

Figure 19 compares the field measurements with the model results and the Beal and Weaver (1970) analytical model. The vertical current velocity measured by the ADCP on

30 April indicates the passing of an internal wave soliton (Fig. 19a). Note that the model operates in the spatial domain, while the velocity observations used for the model initialization are from a fixed mooring. The transformation from the time to the space domain is conducted based on the wavenumber of the internal wave as determined from the exponential decay of its orbital velocity (Table 1). Consequently, I have modeled an internal wave soliton propagating exactly in the x (northward) direction. (In reality, the internal wave soliton may be propagating at some angle to the northward direction.) Under the above assumptions, the model has no meaningful output for the y-component of the magnetic field fluctuations from the internal wave soliton. Due to the extremely small vertical component of the velocity field near the bottom, the vertical component of the magnetic signature is negligible.

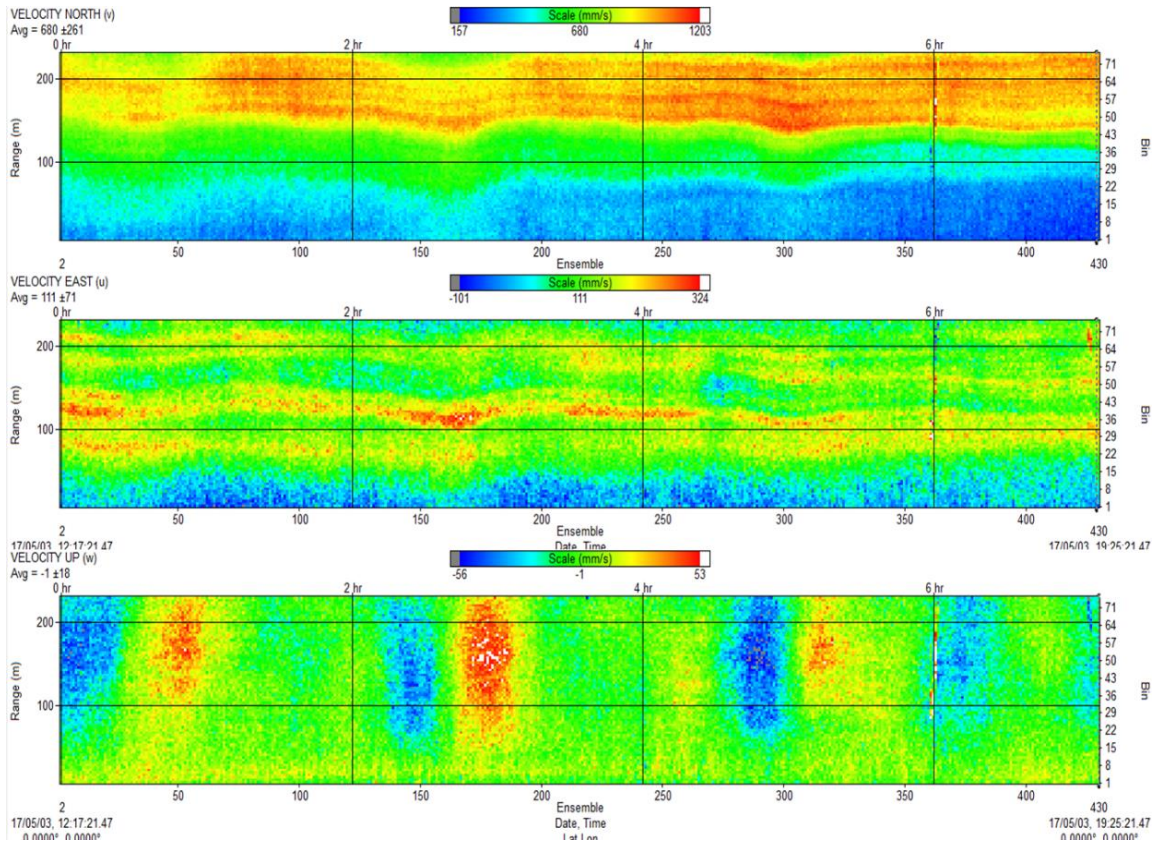
In order to distinguish the internal wave soliton electromagnetic signature from the background ocean circulation, a band-pass filter has been applied to the total magnetic field measured in the field data set. Correspondingly, the x-component of the magnetic field fluctuations produced by the model have been filtered in the same way (Figure 19b). There is reasonably good consistency between the model and the field measurements. At the same time, the Beal and Weaver (1970) model corresponding to the observed internal wave soliton with 7.5 m amplitude (see Table 1) shows significantly higher magnetic signature of the internal wave compared to the field data.





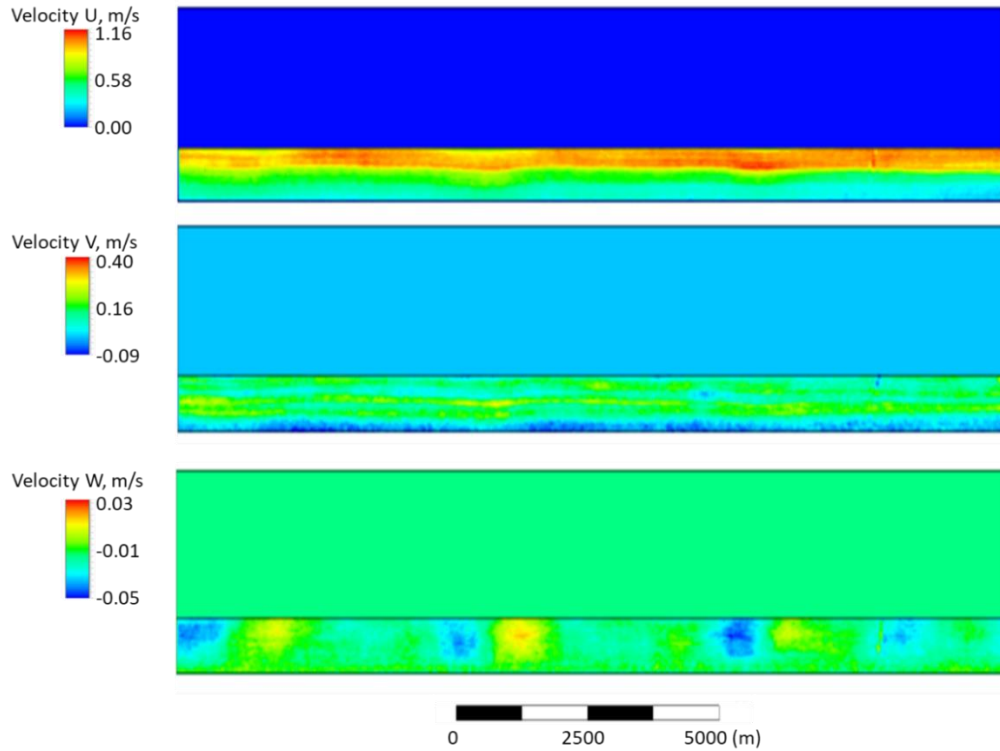
**Figure 19.** a) Vertical current velocity on 30 April showing the passing of an internal wave soliton. b) Comparison of total magnetic field calculated by the model (5 m off the bottom in the center of the domain in the y-direction), measured during the Ambient Weather Experiment on 30 April, and the Beal and Weaver (1970) analytical model.

The MHD model for the internal wave observed on 3 May was initialized with the velocity field data (Fig. 20). The initialization is shown in Figure 21.



**Figure 20.** The velocity field on 3 May 2017, during the Ambient Weather Experiment measured by NSWCCD. The top, middle, and bottom plots show northward, eastward, and vertical velocity components, respectively. All scales are in mm/s.

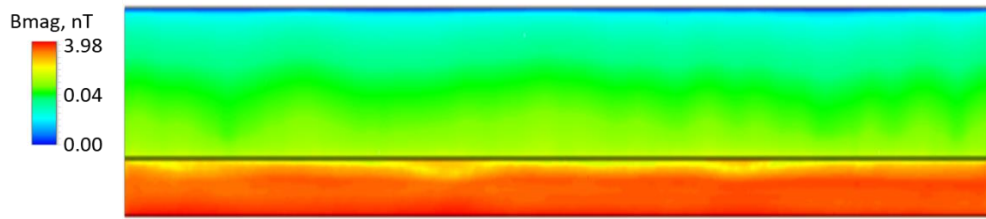
The MHD model was initialized with the velocity field from the 3 May measurements. Figure 22 shows the magnetic signature produced by the MHD model.



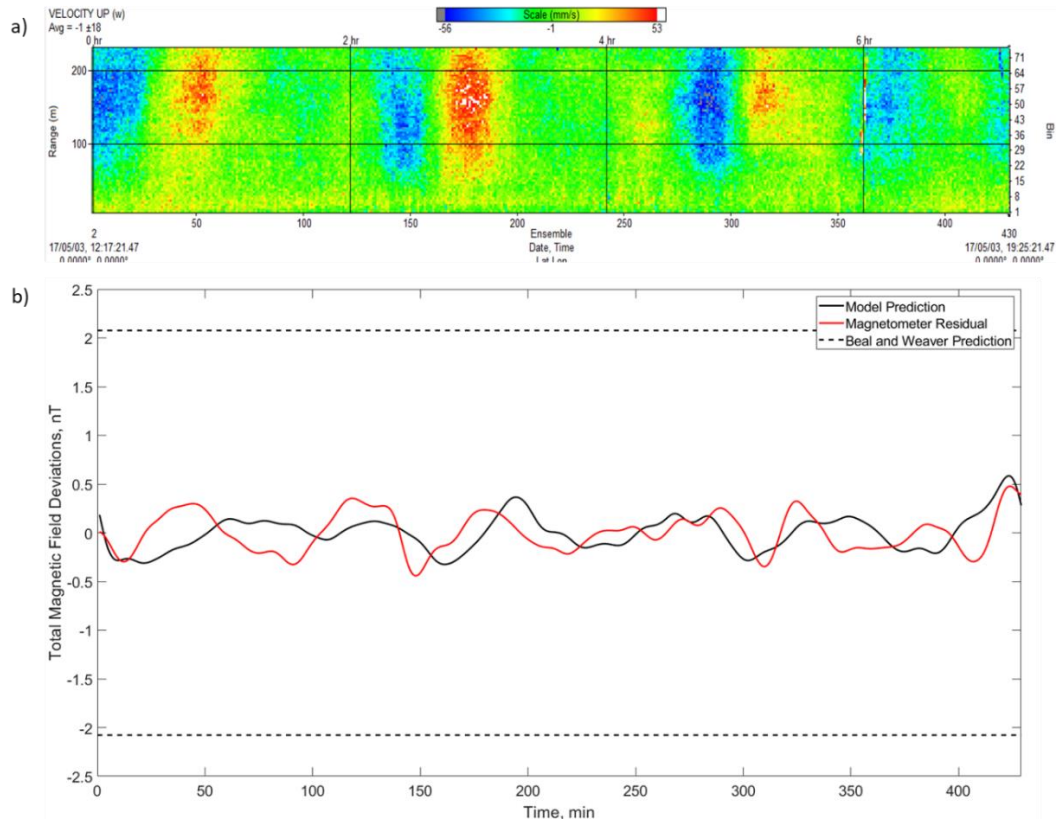
**Figure 21.** Contour plot on the center plane of the velocity field initialization of the model on 3 May from the field measurements. The domain includes air and seafloor layers. The top, middle, and bottom plots show northward, eastward, and vertical velocity components, respectively.

Figure 23 compares the field measurements with the model results corrected for the resolution in the bottom boundary layer and the Beal and Weaver (1970) analytical model. The vertical current velocity measured by the ADCP on 3 May indicates the passing of an internal wave soliton (Fig. 23a). In order to distinguish the internal wave soliton from the background ocean circulation, a band-pass filter has been applied to the field data and in the model in the same way as in Figure 19b. There is also good consistency in the magnetic signature amplitude between the model and the field measurements (Fig. 23b). Apparently, there is some difference between the phases of the field data and model results, which can be explained by the spatial separation by approximately 500 m in the cross-shelf direction between the ADCP and magnetometer during the experiment on May 3. Notably, the Beal and Weaver (1970) model corresponding to the observed internal wave soliton with 13.5 m amplitude (see Table 1)

shows significantly higher magnetic signature compared to observational data, in this case as well.



**Figure 22.** Contour plot on the center plane of the magnitude of the modeled magnetic field fluctuations induced by the velocity field on 3 May shown in log scale. The horizontal black lines indicate the air-sea interface and the sea-bottom interface.



**Figure 23.** a) Vertical current velocity on 3 May showing the passing of an internal wave soliton. b) Comparison of total magnetic field calculated by the model (5 m off the bottom in the center of the domain in the y-direction), measured during the Ambient Weather Experiment on 3 May, and the Beal and Weaver (1970) analytical model.

### **3.5 Verifications of the magnetohydrodynamic and magnetostatic models with laboratory experiment**

An additional verification of the *ANSYS Fluent* MHD and *Maxwell* models was conducted using the University of Miami Rosenstiel School of Marine and Atmospheric Science SURge STructure Atmosphere INteraction (SUSTAIN) tank using results from Kluge et al. (2018) with surface waves in saltwater and freshwater environments. Additionally, an empty tank test was done to determine the magnetic signature produced by the wave maker at SUSTAIN.

In the experiment at the SUSTAIN facility (Fig. 24), the water level in the tank was 0.75 m and waves were produced at 0.56 Hz and with 0.1 m amplitude. An acoustic elevation sensor was located on top of the tank and was used to measure the surface waves generated in the tank. Two Geometrics G-824 magnetometers measured Earth's total magnetic field and its fluctuations due to surface waves and two high-resolution accelerometers (TE Connectivity Model 4630A-005-060) were used to measure the tank vibrations. Accelerometers were placed on the tank to determine the contribution of and remove vibrations of the tank from the measured magnetic signature during experiments. A differential method was used by placing the two magnetometers on the outer tank walls, separated horizontally by approximately one-half wavelength (1.83 m). This method effectively suppressed extraneous magnetic distortions (such as passing cars), while doubling the magnetic signal of surface waves. The experiments were conducted around midnight in order to further reduce the effect of extraneous sources of magnetic distortions.

Spectral analysis of the experimental magnetic signal of surface waves indicates that most of the energy in the signal was at the wave frequency of 0.56 Hz and less energy was at higher frequency harmonics, which are due to non-linearity of shallow water surface waves (Fig. 25).

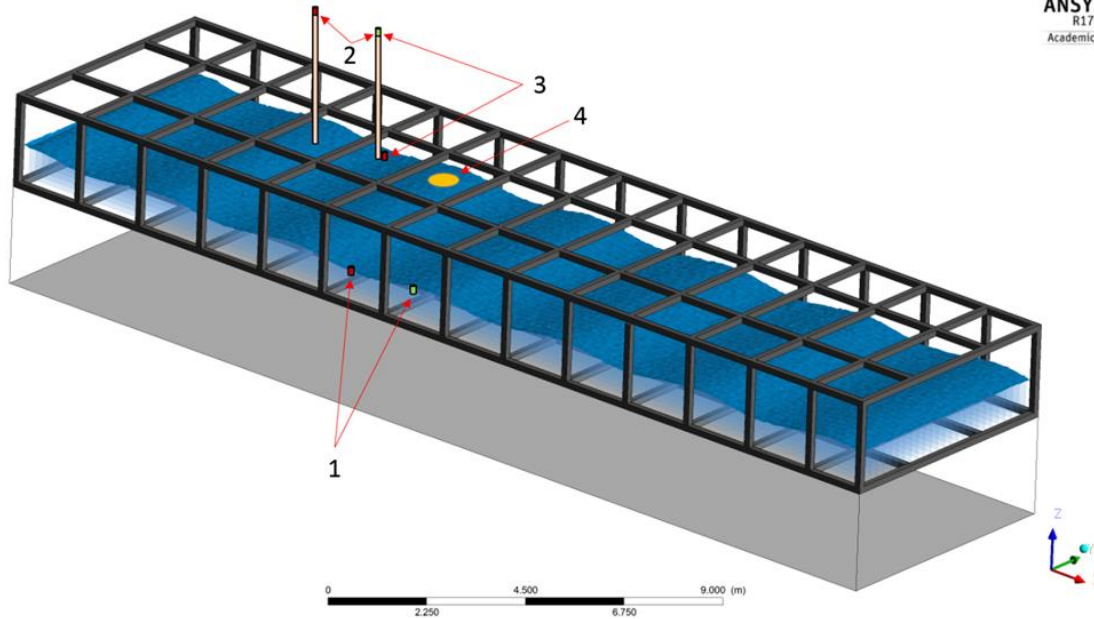


**Figure 24.** Setup of magnetometer pair during SUSTAIN laboratory experiment to measure the magnetic signature of surface waves. 1) Two magnetometers placed on the side of the tank near the water level. 2) Sensors placed above the tank on two tripods. 3) One magnetometer on tripod and one on the glass. 4) Acoustic transducer.

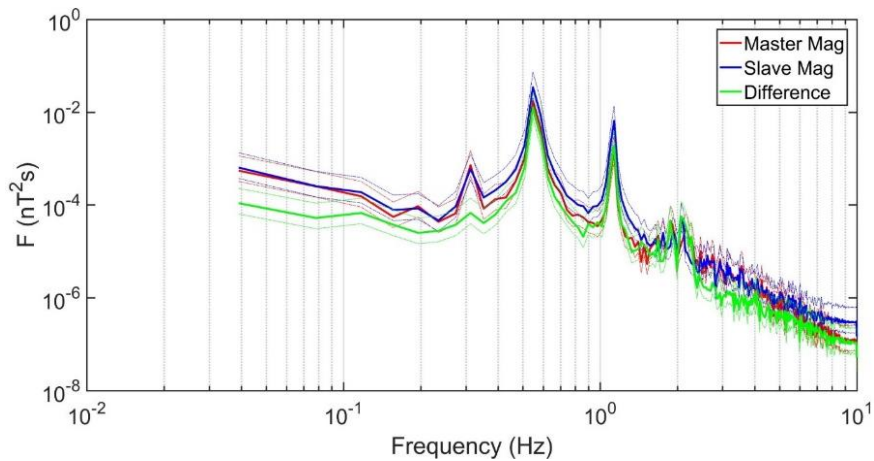


**Figure 25.** Spectra from surface waves magnetic signature time series. The red solid line shows the spectrum from the master magnetometer, the blue line indicates the spectrum from the slave magnetometer, and the green represents the difference spectrum calculated by taking the difference between the master and slave magnetometers time series. The dashed lines indicate the confidence intervals of the spectra (After Kluge et al. 2018).

Experimental results suggest that the magnetic signature generated by surface waves in the SUSTAIN tank was an order of magnitude larger than predicted by the traditional

model (Podney 1975). Based on theoretical calculations, the discrepancy may come from the difference of magnetic permeability in water and air that is not accounted for in the traditional model.

Further verification of the *Fluent* and *Maxwell* models was conducted by simulating this laboratory experiment. The *Fluent* MHD model can effectively reproduce the magnetohydrodynamic effect of surface waves (Section 3.1). The *Maxwell* model is a magnetostatic model and may help to elucidate the difference between the measured magnetic signature of surface waves and the predicted value of the traditional models.

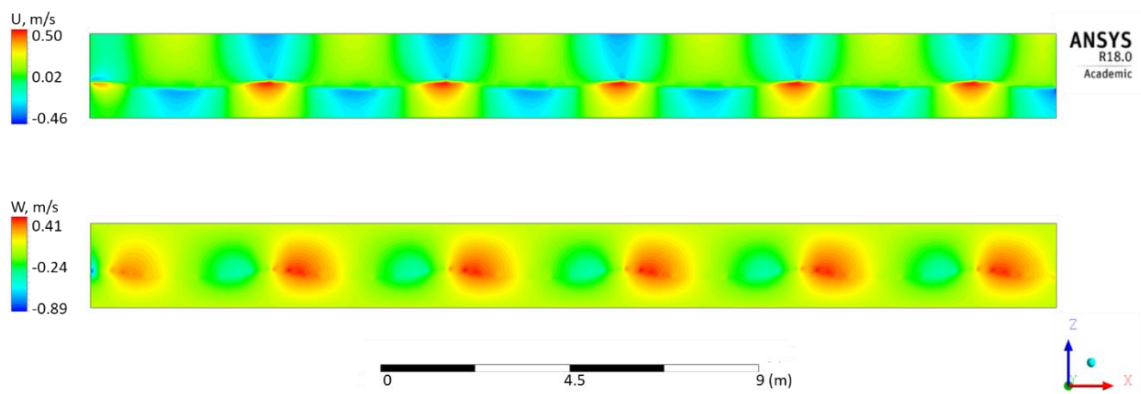


**Figure 26.** Center plane contour plot of initial velocity U (top) and W (bottom) produced by 0.1 m amplitude 0.56 Hz linear surface wave in SUSTAIN tank in the ANSYS *Fluent* CFD model.

A magnetohydrodynamic simulation of the SUSTAIN tank experiment was conducted using the ANSYS *Fluent* MHD model. The numerical domain is 22 m long, 6 m wide, and 2 m deep with mesh resolution of 0.04 m in all directions. The mean water level was set to 0.75 m, which is the same as in the SUSTAIN experiment. Two cases were run: linear and non-linear surface waves. The linear surface waves were initialized with 0.1 m amplitude and 4.18879 m length (equivalent to 0.56 Hz as in the experiment). For the case with the linear waves, the velocity field was “frozen” after one time-step and the MHD model was applied (Fig. 26). To produce non-linear waves, the CFD model was allowed to run for 2.5 s until the waves became non-linear and the MHD model was applied to the “frozen” velocity field at that time. The Earth’s magnetic field in these simulations was  $B_x = 1.99 \times 10^{-5}$  T,  $B_y = -1.56 \times 10^{-5}$  T,  $B_z = -3.6 \times 10^{-6}$  T, which accounts

for the angle of the SUSTAIN tank relative to magnetic north (wave propagation is  $45^\circ$  to the left of magnetic north).

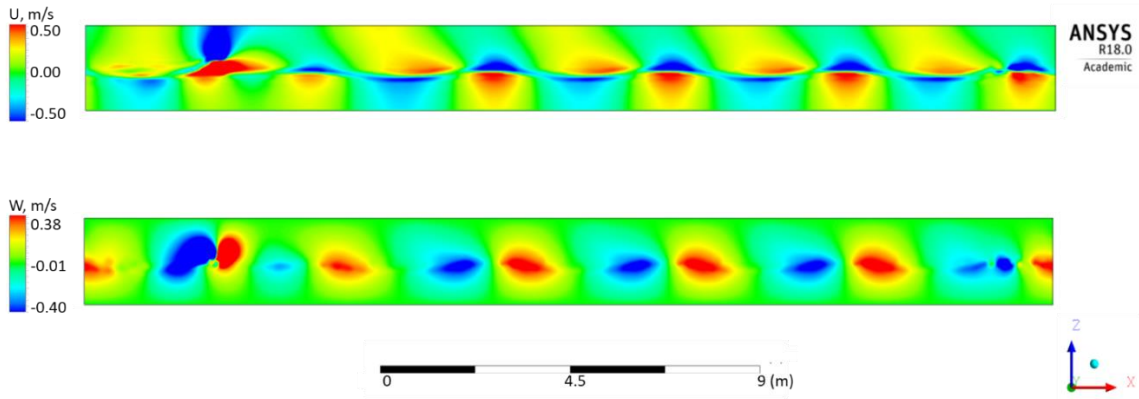


**Figure 27.** Center plane contour plot of initial velocity U (top) and W (bottom) produced by 0.1 m amplitude 0.56 Hz non-linear surface wave in SUSTAIN tank in the ANSYS *Fluent* CFD model after 2.5 s of simulation.

These linear surface waves produced fluctuations in the z-component of the magnetic field of approximately 0.026 nT (Fig. 28a). The non-linear surface waves produced fluctuations in the z-component of the magnetic field of approximately 0.03 nT (Fig. 28b).

The *Fluent* MHD model produces a magnetic signature of the surface waves in the SUSTAIN experiment very similar to that predicted by the traditional model but smaller than what was measured. It is possible that the small difference in magnetic permeability between the air and water coupled with the angle change of the wave could account for the difference between the model prediction and the observations.



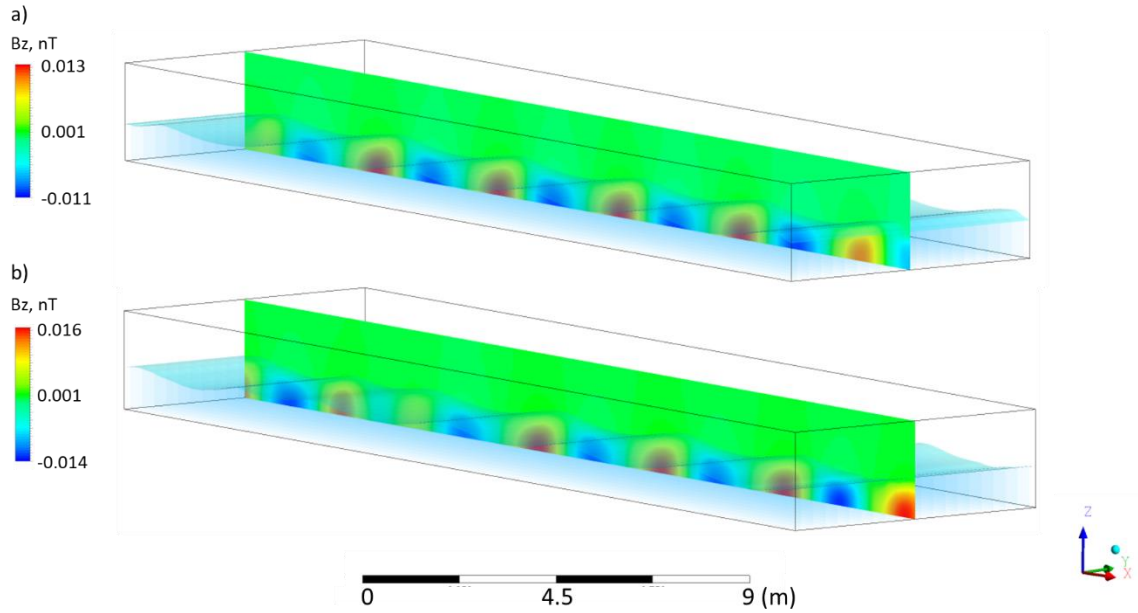


**Figure 28.** ANSYS *Fluent* MHD simulation of laboratory experiment with (a) linear surface waves and (b) nonlinear waves. Contour plot shows magnetic field fluctuations for the z-component.

The difference in magnetic permeability between the air and water results in the magnetic field refraction (Pendry et al. 2006). At the air-water interface, the normal component of the magnetic field is continuous while the tangential component has a discontinuity, which can be described by the following equations:

$$\Delta B_n = B_{an} - B_{wn} = 0 \quad (49)$$

$$\Delta B_t = B_{at} - B_{wt} = B_0 (\chi_a - \chi_w) \sin \alpha \quad (50)$$

where the subscripts  $t$  and  $n$  denote the tangential and normal components of the magnetic field, respectively.  $B_0 = (B_{0t}^2 + B_{0n}^2)^{1/2}$  is the magnetic field in the free space,  $B_a$  is the magnetic field in the air,  $B_w$  is the magnetic field in the water,  $\alpha$  is the inclination angle, and  $\chi_a$  and  $\chi_b$  are the volume magnetic susceptibilities of the air and water, respectively ( $\chi_a=0.36 \times 10^{-6}$ ,  $\chi_w=-9.05 \times 10^{-6}$ ). The change in the magnetic field due to refraction as it passes through the air-water interface is determined as follows:

$$\Delta B = B_0' - B_0 = B_0 (1 + (\chi_w - \chi_a) \cos^2 \alpha) - B_0 = B_0 (\chi_w - \chi_a) \cos^2 \alpha = -0.1391 \text{ nT} \quad (51)$$

where  $B_0 = 43,926.2$  nT is the Earth's magnetic field entering the air-water interface,  $B_0'$  is the Earth's magnetic field after passing through the interface and undergoing refraction, and  $\alpha$  is  $54.5358^\circ$  at the Miami location.

The presence of the wavy surface results in variations of the magnetic field caused by the effect of magnetic field refraction (Soloviev and Dean 2018). The amplitude of magnetic field variations is calculated as follows:

$$\begin{aligned} \Delta B' &= B_0 \left(1 + (\chi_a - \chi_w) \cos^2(\alpha - \beta)\right) - B_0 \left(1 + (\chi_a - \chi_w) \cos^2(\alpha + \beta)\right) = \\ &B_0 (\chi_a - \chi_w) \left(\cos^2(\alpha - \beta) - \cos^2(\alpha + \beta)\right) = 0.14 \text{ nT} \end{aligned} \quad (52)$$

where  $\beta$  is the maximum slope of the wavy surface, which is estimated as  $8.9^\circ$  for the waves in the SUSTAIN facility during the above-described experiment.

To explore this effect of magnetic permeability difference, a magnetostatic simulation of the laboratory experiment has been conducted using the *ANSYS Maxwell* model (Fig. 29). The model accounts for the difference in electrical conductivity between air and water, but the conductivity differences should have no impact on the solution because *ANSYS Maxwell* does not allow for the introduction of wave motion in fluid (only translational or rotational motion - see Section 2.3). The relative magnetic permeability of air was set to  $1.0000004 \text{ H m}^{-1}$  and water was set to  $0.999991 \text{ H m}^{-1}$ , which results in an approximately 0.14 nT jump of the magnetic field at the air-water interface. The results produced by the *ANSYS Maxwell* model are quantitatively consistent with estimates of  $\Delta B$  and  $\Delta B'$  from a simple analytical model.

The magnetic signature of surface waves consists of the magnetohydrodynamic (Fig. 28) and magnetostatic (Fig. 29) components. These magnetic components have somewhat different phases and decay rates, depending on the height of surface waves and their direction relative to the Earth's magnetic field. Note that in the laboratory settings with relatively small surface waves, the magnetostatic component appears to be an order of magnitude larger than the magnetohydrodynamic component. The model and laboratory experiment results (Kluge et al. 2018) appear to be in general agreement (Fig. 30). However, there are vibrations of the SUSTAIN tank in high-gradient magnetic fields in

the SUSTAIN facility (Kluge et al. 2018), which might result in the additional errors that have not yet been analyzed and corrected, if necessary. The analysis of the SUSTAIN data is still in progress.

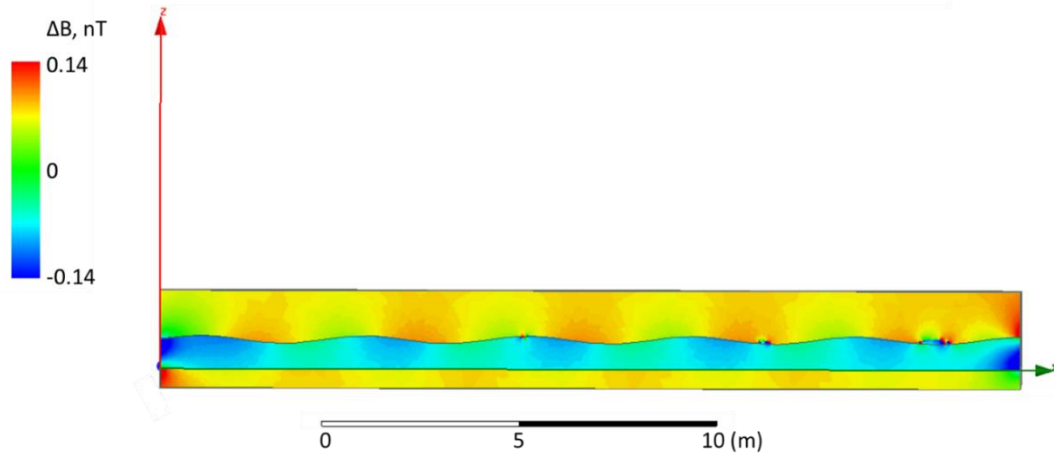


**Figure 29.** ANSYS Maxwell simulation of laboratory experiment with linear surface waves. Contour plot shows total magnetic field fluctuations (Soloviev and Dean 2018).

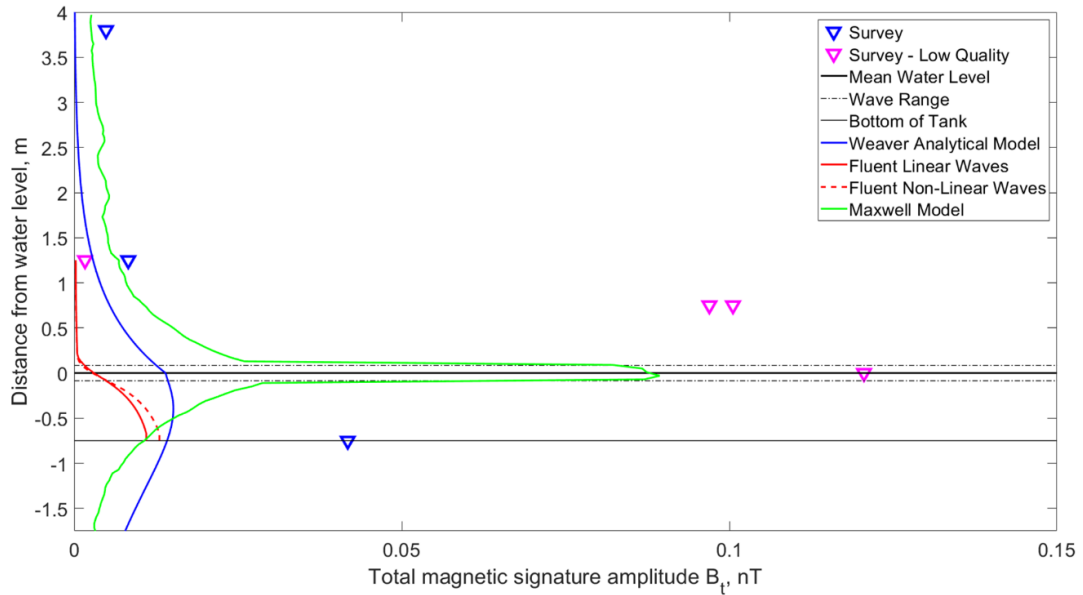


**Figure 30.** Comparison of traditional model, measurements, and magnetohydrodynamic (linear and non-linear wave), and magnetostatic models of the amplitude of the magnetic signature of surface waves.

In this work, both the ANSYS Fluent MHD and the ANSYS Maxwell models were used because neither model can reproduce both the effects of magnetic induction in a moving

fluid and magnetic permeability jump at the interface of air and water. *ANSYS Fluent* MHD is able to account for magnetic induction due to wave motion, while *Maxwell* is not able to reproduce motion of water (see Section 2.3). *ANSYS Maxwell* is able to simulate the effect of the magnetic permeability jump at the air-water interface, while *ANSYS Fluent* MHD always compensates the permeability differences in the environment and therefore is not able to account for the magnetic permeability jump at the air-water interface.

### 3.6 Summary

The *Fluent* solution is reasonably close to the analytical solution of Weaver (1965) for surface waves of a 5 s period except near the air-water interface. The comparison with analytical models in the upper few meters and in the air is complicated by the fact that these models (Weaver 1965, Podney 1975, and others) contradict each other on the magnetic field at the air-sea interface. Unfortunately, there are no reliable magnetic measurements in the air above the wavy surface in order to verify either the analytical or the *Fluent* model near the air-sea interface or in the air. Therefore, comparison of the *Fluent* MHD model results with the analytical model solutions in the air is not feasible.

The *Fluent* MHD model appears to coincide well with the results of the analytical models for the 50 m internal wave that can be classified as a deep water internal wave (deep water means  $kh \ll 1$ ). There is, however, a significant difference between the *Fluent* MHD model and the analytical solutions for the 500 m and 1000 m internal waves (Figs. 12 and 13). These waves can be classified as shallow water internal waves, which inherently involve boundary effects. The analytical models either ignore or do not properly account for the boundaries.

The intercomparison of the *Fluent* MHD model with the field data (Figs. 19 and 23) suggests that the *Fluent* MHD model is able to produce more consistent results than the Beal and Weaver (1970) analytical model. Initialization of the *Fluent* model with the 3D spatial velocity field can further increase the accuracy of the magnetic signature prediction. In particular, in this work, there was not sufficient information from the field measurements on the direction of internal wave soliton propagation. Additionally,

velocity measurements near the seafloor in the bottom boundary layer are needed for initialization of the model since the magnetic measurements used for model verification are located at approximately 1 m above the seafloor.

The effect of self-inductance appears to be important in the generation of the magnetic signature of shallow water waves. Self-inductance is a result of a non-stationary solution, which *Fluent* MHD can properly account for. The analytical models typically do not account for self-inductance.

The results of the laboratory measurements at SUSTAIN are well described with the combination of the *Fluent* MHD and *Maxwell* models. The measurements are dependent on both the magnetostatic and magnetohydrodynamic solutions due to the combination of orbital velocities of the waves and the difference in magnetic properties of the air and water.

In general, the magnetic models do a good job describing the magnetic field fluctuations produced by the field measurements and the laboratory experiment. The verified model suite is then applied to other small-scale oceanographic phenomena and their magnetic signatures are compared (Section 5). In Sections 4 and 5, I implement the approach of Matt et al. (2014) and Soloviev and Dean (2015) that does not include self-inductance or boundary layer effects, which may result in an underestimation of the magnetic signature in the bottom boundary layer. This, however, is not expected to affect the comparison of the magnetic signature produced by submesoscale oceanographic processes since the signature maxima reported in Table 2 do not occur in the bottom boundary layer.

## **4. Magnetic signature of DVM**

### **4.1 Modeling of DVM in the Straits of Florida**

Dean et al. (2016a) simulated DVM of zooplankton in the Straits of Florida in a 50 m by 50 m by 250 m domain. In order to ensure adequate mesh resolution, they performed a validation test for three different mesh resolutions: 2 m, 1 m, and 0.5 m. There was some difference in the results between the 2 m and 1 m mesh resolutions, but no significant difference between the 1 m and 0.5 m mesh resolutions. Therefore, a homogenous 1 m

mesh resolution was used for all calculations. Figure 31 shows the initial conditions used in the Dean et al. (2016a) model to simulate DVM in the Straits of Florida. The velocity profile was based on 11 months of observations from a 75 kHz bottom mounted ADCP at a 240-m isobath. However, there was no temperature or salinity information collected during this time so the density profile was estimated from historical data. The Straits of Florida is a very energetic area, and changes in current velocity and density can occur over different time scales, which may have an impact on the effect of DVM of zooplankton on turbulence generation.

Boundary conditions of the model are no-slip on the bottom wall, slippery on side walls, and a fixed wind stress on the top wall to simulate an approximately  $5 \text{ m s}^{-1}$  wind. Periodic boundary conditions are imposed at the inlet and outlet to allow for infinite fetch, as well as to allow the particles simulating zooplankton to stay in the domain indefinitely. The heat flux at the top wall is  $20 \text{ W m}^{-2}$  during daytime (just before sunset or just after sunrise) and  $-100 \text{ W m}^{-2}$  during nighttime.

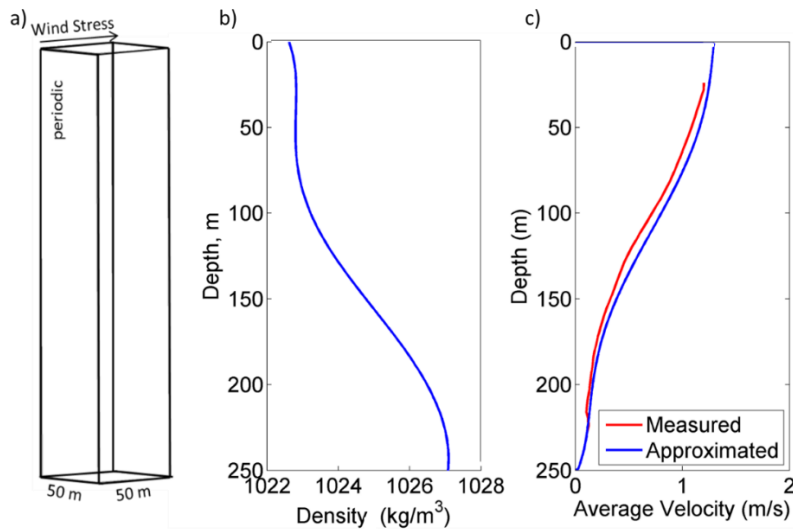


**Figure 31.** Straits of Florida CFD model setup: (a) numerical domain; (b) initial density profile; (c) measured current velocity profile compared to the linearized average profile initiated in the model.

Solution methods for the model are set as follows: pressure-based solver with the SIMPLE scheme for pressure-velocity coupling; for spatial discretization, PRESTO! scheme was used for pressure, Least Squares Based scheme for gradient, Bounded

Central Differencing for momentum, and Second Order Upwind for energy. Second Order Implicit scheme was used for the transient formulation.

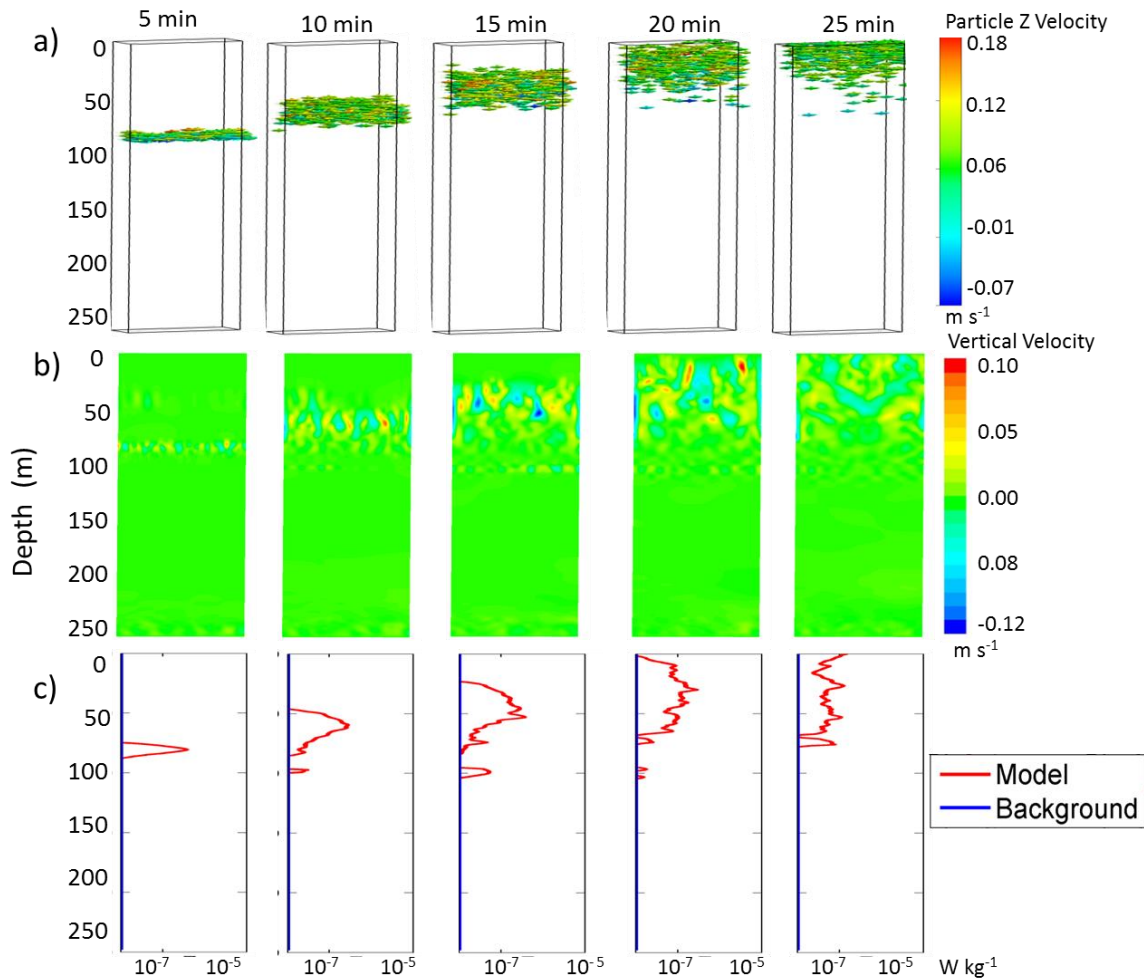


**Figure 32.** Modeling turbulence produced by DVM of zooplankton in the Straits of Florida by injecting 10,000 positively buoyant particles with 0.01 m diameter at 100 m: (a) particle locations at five-minute intervals; (b) contour plots of vertical velocity ( $\text{m s}^{-1}$ ); (c) average profiles of dissipation rate  $\epsilon$  ( $\text{W kg}^{-1}$ ). Background turbulence dissipation rate in the Straits of Florida is set at  $10^{-8} \text{ W kg}^{-1}$  following measurements by Gregg et al. (1999). In the upper few meters, dissipation rate exceeded  $10^{-8} \text{ W kg}^{-1}$  due to surface wind stress and has been removed.

Dean et al. (2016a) simulated the effect of a range of concentrations of zooplankton undergoing DVM on small-scale turbulence. Three different concentrations were tested: 10,000 individuals/ $\text{m}^3$  (extreme concentration), 5,000 individuals/ $\text{m}^3$  (intermediate concentration), and 1,000 individuals/ $\text{m}^3$  (low concentration). The case with the extreme concentration of particles (proxy for migrating zooplankton) showed an increase in

dissipation rate of turbulent kinetic energy by two to three orders of magnitude over background turbulence (Fig. 31c). Background turbulence for the Straits of Florida was reported by Gregg et al. (1999) as  $10^{-8} \text{ W kg}^{-1}$ . At intermediate concentrations, the increase in dissipation rate of turbulent kinetic energy was one to two orders of magnitude above background turbulence levels (Fig. 33c). At low concentrations, there was less than one order of magnitude increase in dissipation rate of turbulent kinetic energy over background levels (Fig. 34c). The model results suggest that the level of turbulence caused by DVM is likely concentration-dependent.

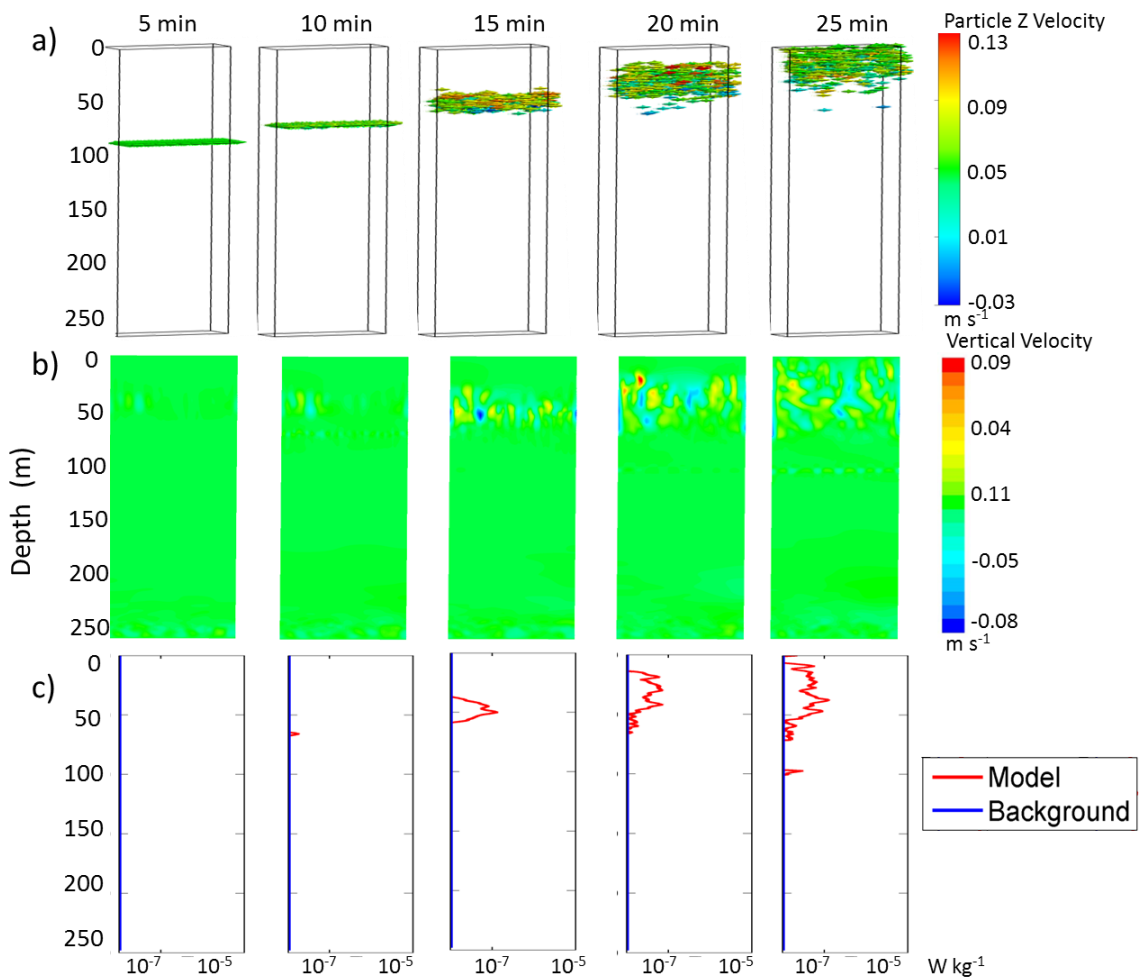


**Figure 33.** Same as in Fig. 32, but by injecting 5000 particles  $\text{m}^{-3}$ .



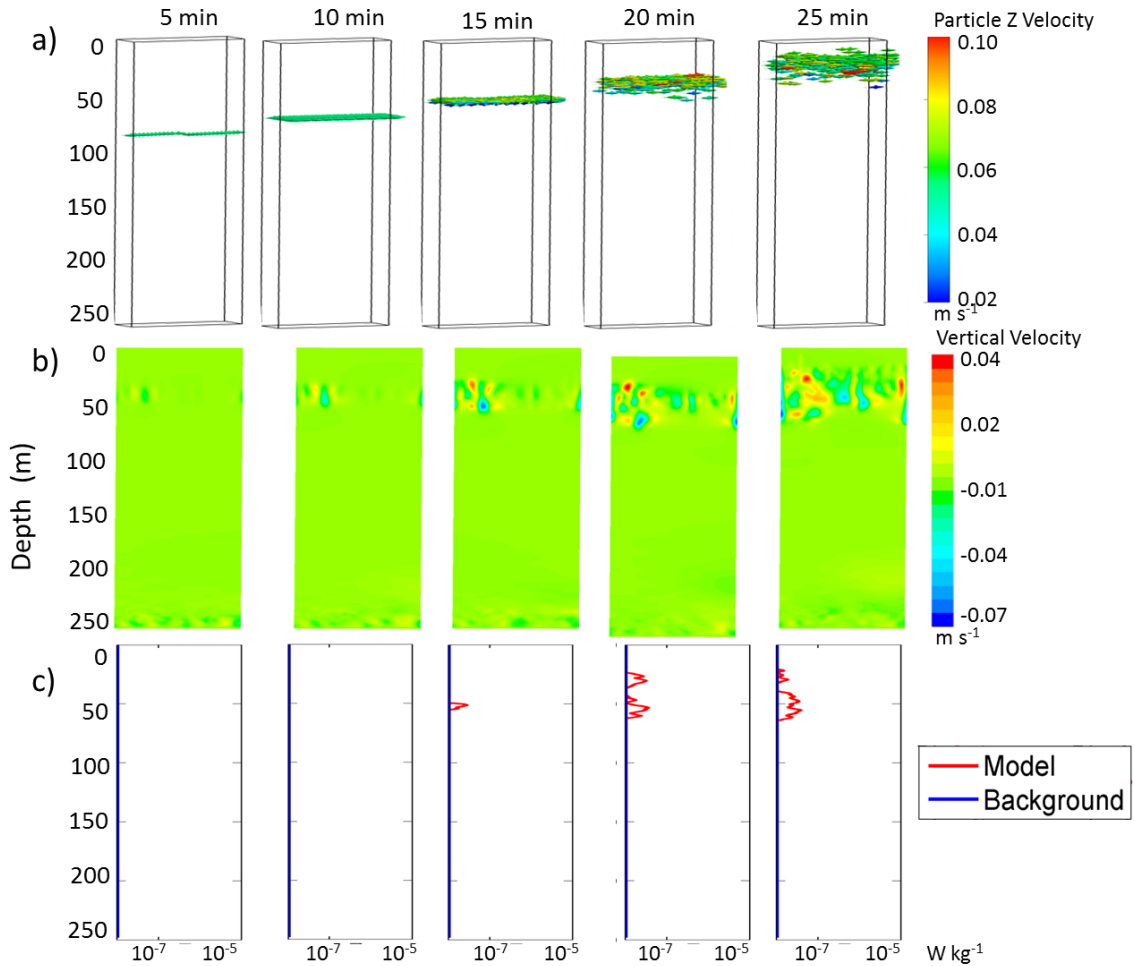


**Figure 34.** Same as in Fig. 32, but by injecting 1000 particles  $\text{m}^{-3}$ .

These preliminary model results were compared with current velocity profiles from ADCP data collected in the Straits of Florida (USCG 2008). Figure 35a shows averaged northward current velocity profiles over an 11-month ADCP data set during migration as compared to three hours before and after migration times. Only cases where the Florida Current was present above the bottom ADCP mooring were considered (maximum northward velocity component greater than  $0.75 \text{ m s}^{-1}$ ) to eliminate the influence of coastal waters, which may have different biophysical interactions. There is a small, but statistically significant, decrease in northward current velocity during migration as compared to the three-hour difference (Fig. 35b). A three-hour difference was chosen to emphasize the higher frequency process associated with DVM and suppress lower

frequency, high-energy processes such as mesoscale eddies, diurnal and semidiurnal tides, and inertial oscillations.

The modeled average current velocity was compared in cases with particles and without particles. In the extreme concentration of particles case ( $10,000 \text{ org/m}^3$ ), 25 minutes after injection, there was a decrease in current velocity (Fig. 36) qualitatively similar but an order of magnitude larger than that seen in the field data (Fig. 35b). In the low concentration of particles case ( $1000 \text{ org/m}^3$ ), there was a smaller decrease in current velocity (Fig. 37), which was quantitatively similar to that observed from the field data (Fig. 38). Based on this information, it is possible to have an idea about the average concentration of zooplankton undergoing migration during the 11 month period of measurements. Comparison of the model and average ADCP velocity profiles is, of course, complicated by their substantial dependence on the environmental conditions, not directly related to DVM, including wind/wave mixing, Florida Current meandering, and tides. In principle, diurnal cycles, breezes, and tides can have an effect on the velocity field even at 20–30 m depth.

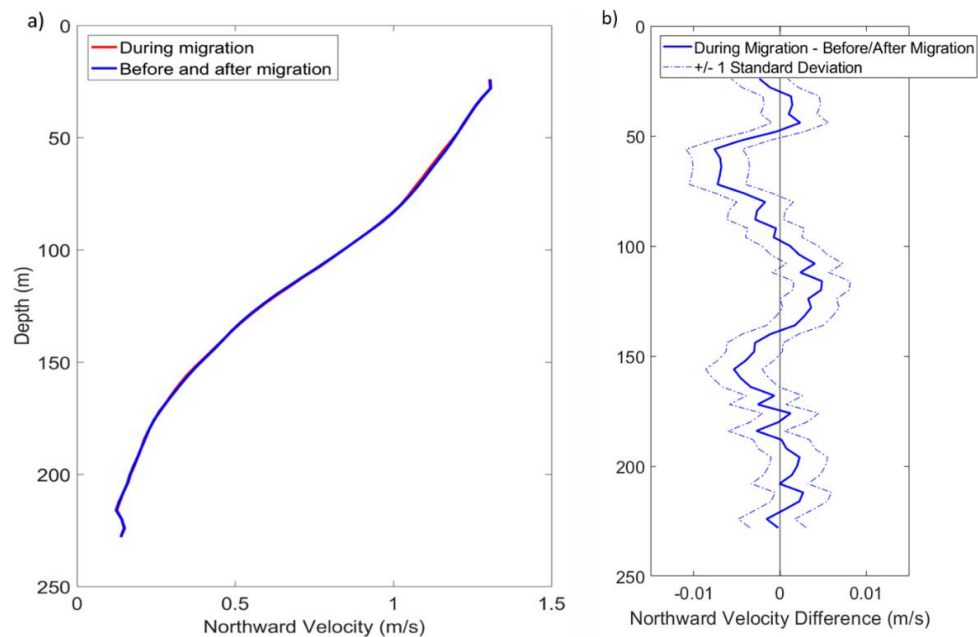


**Figure 35.** Average ADCP northward current velocity profiles in full 11-month data set during migration compared to before migration from ADCP. The velocity profile during migration was calculated as an hour-long average around sunrise/sunset and the before migration velocity profile was calculated as an hour-long average, three hours prior to and after sunrise/sunset. a) Average velocity profile. b) Difference between during migration and  $\pm 3$  hours using a 67% confidence interval (dashed lines).

This small, on the order of 0.01 m/s, but statistically significant decrease in current velocity can be linked to the presence of zooplankton undergoing DVM and is likely caused by the change in the vertical mixing coefficient produced by additional turbulence from the DVM of zooplankton. The increased turbulent friction could affect the current velocity profiles. It should be noted that most of the decrease in current velocity from the model took place in the upper 50 m of the ocean. However, the near surface bins of the ADCP data had to be removed from the calculation due to multiple reflections. If current velocity measurements were available closer to the surface of the ocean, a larger effect on current velocity might be seen.

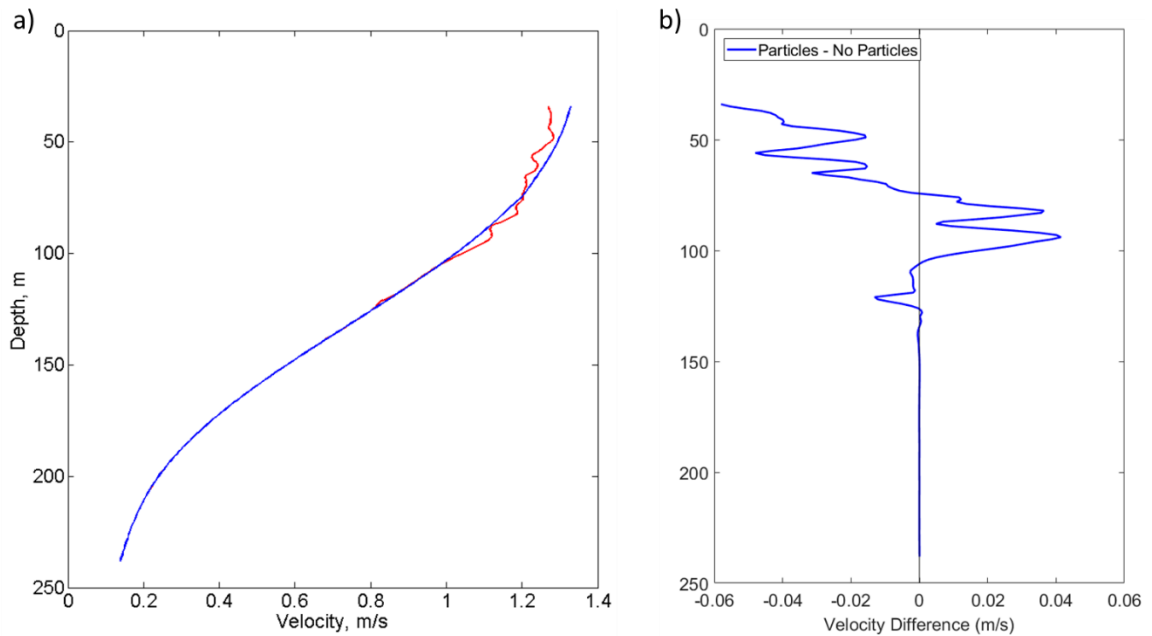


**Figure 36.** Average model current velocity in Straits of Florida in extreme concentration case (10,000 org/m<sup>3</sup>). a) Average current velocity profiles in particles and no particles cases. b) No particles case at 25 minutes after injection minus particles case at same time. Particles representing zooplankton were released at 100 m depth.

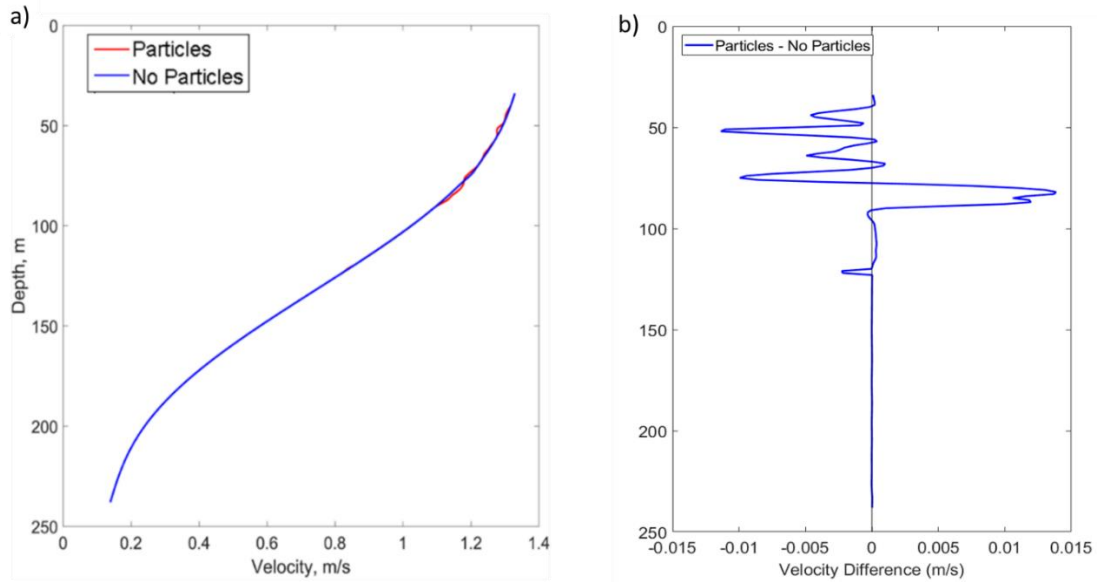


**Figure 37.** Average model current velocity in Straits of Florida in case with low concentration of particles ( $1000 \text{ org/m}^3$ ). a) Average current velocity profiles in particles and no particles cases. b) No particles case at 25 minutes after injection minus particles case at same time. Particles representing zooplankton were released at 100 m depth.

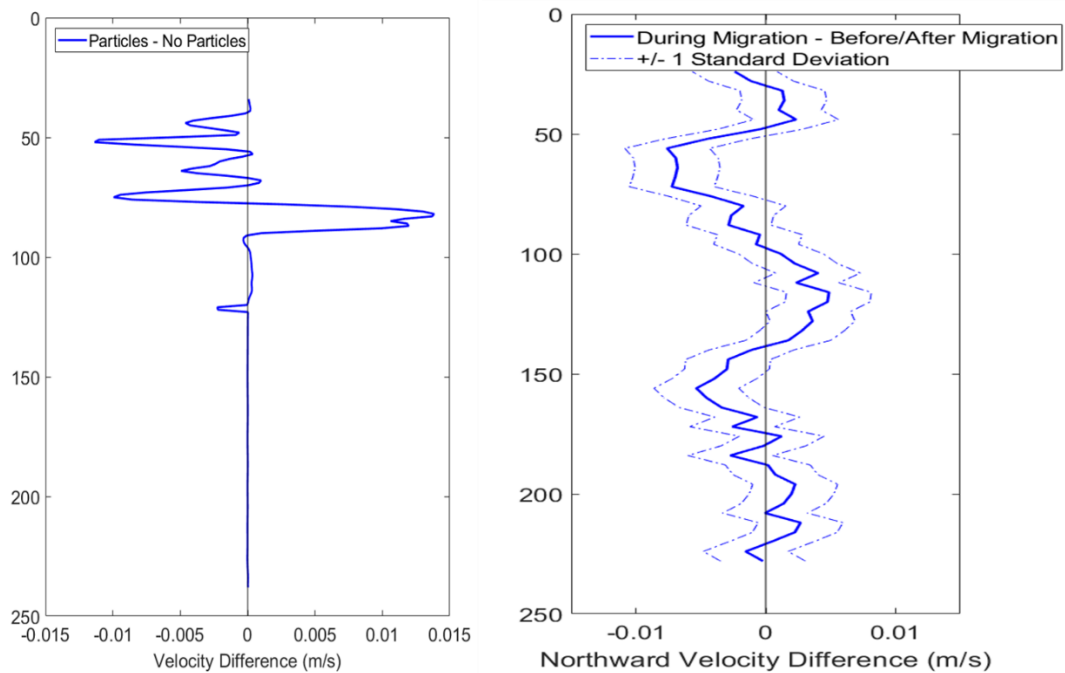


**Figure 38.** Comparison of effect of DVM of zooplankton on current velocity in the model with a low concentration of particles and observations.

## 4.2 Modelling of DVM in Saanich Inlet

The above-described *ANSYS Fluent* CFD model has also been applied to Saanich Inlet, British Columbia, Canada with a somewhat different domain (50 x 50 x 150 m) and the same mesh that was used in the Straits of Florida simulation. For the initial conditions, stratification information was taken from temperature and salinity profiles averaged over several days of sample collection (Fig. 39) (Rousseau 2010). Current velocity profiles were not available for this specific location so it was estimated from the VENUS observatory in the Strait of Georgia, which is just outside of Saanich Inlet (<https://data.oceannetworks.ca/>).

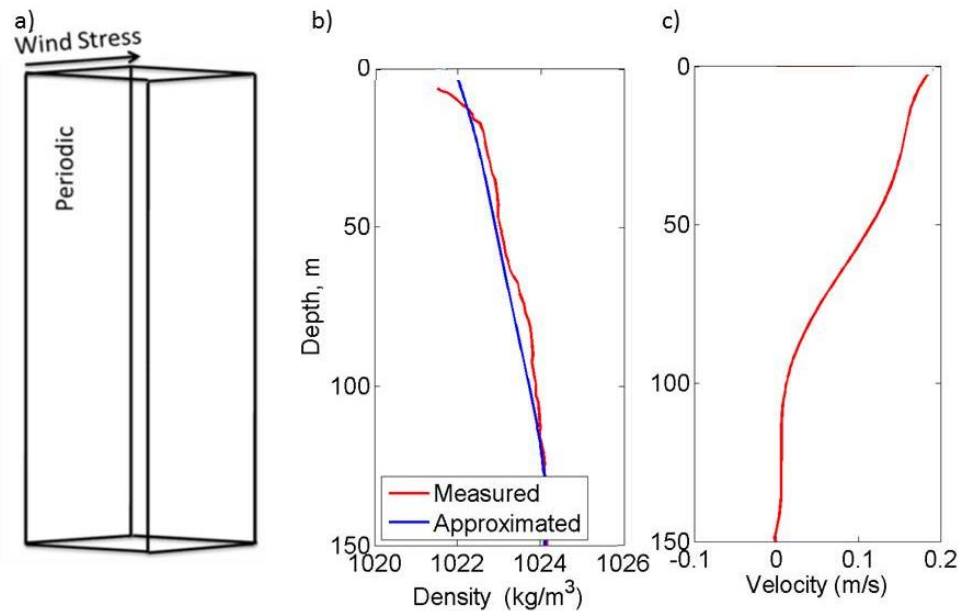


**Figure 39.** Saanich Inlet model setup: a) numerical domain; b) measured potential density profile compared to the linearized average profile initiated in the model; c) initial current velocity average profile. (After Dean et al. 2016a.)

In Saanich Inlet, the case with extreme concentration of particles (10,000 individuals/m<sup>3</sup>) showed an increase in  $\epsilon$  by approximately 2 - 3 orders of magnitude over background turbulence dissipation rate when particles, a proxy for migrating zooplankton, were present in the mixed layer (Fig. 40). The measured background dissipation rate of turbulence was reported in Kunze et al. (2006) on the order of  $10^{-9}$  W kg<sup>-1</sup>. The turbulence induced in the model by the particles remains in the wake of the

particles for some time after they have migrated out of the area, which is seen on the vertical velocity contour plots (Fig. 41).

The case with an intermediate concentration of particles (5000 individuals/m<sup>3</sup>) showed an increase in dissipation rate of turbulent kinetic energy of approximately 1 - 2 orders of magnitude during particle migration (Fig. 41). There is also an increase of turbulence in the wake of the particles, but it is less pronounced than at the extreme concentration of particles.

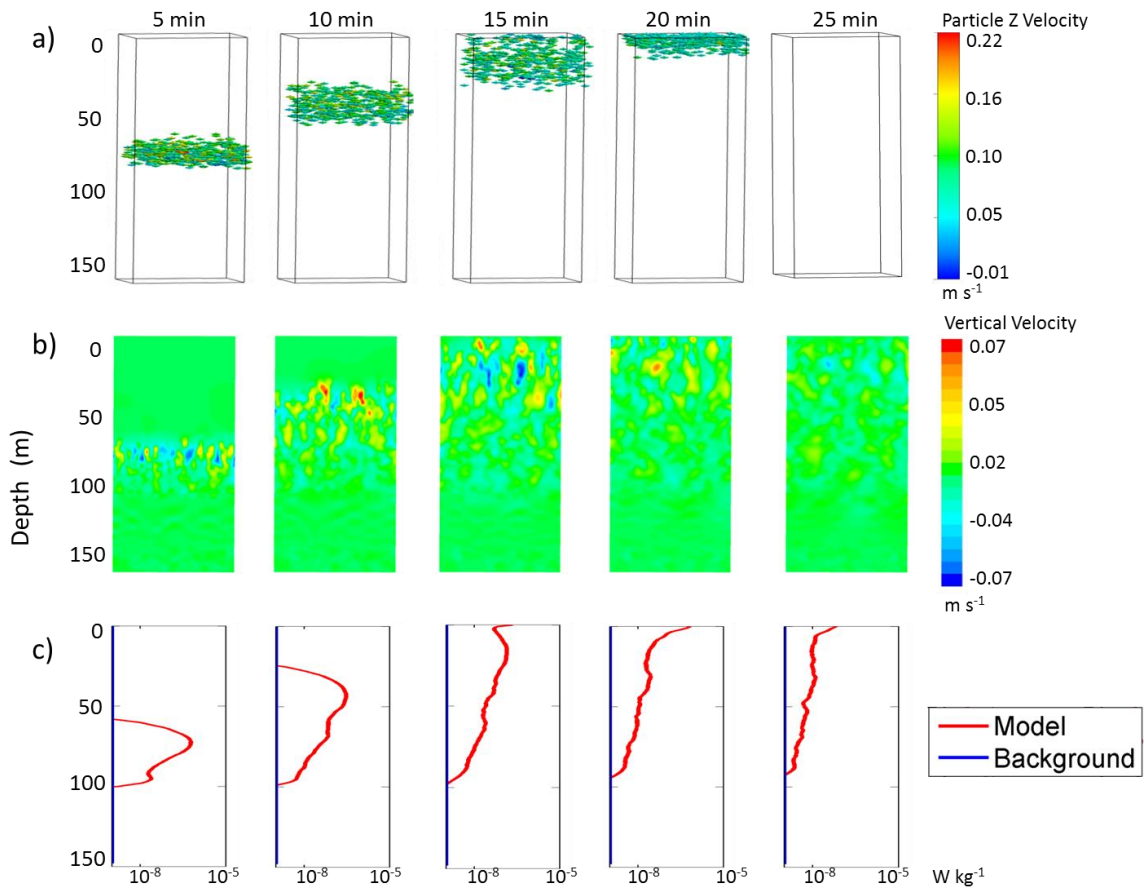


**Figure 40.** Modelling the turbulence produced by DVM of zooplankton in Saanich Inlet by injecting 10,000 m<sup>-3</sup> positively buoyant particles with 0.01 m diameter at 100 m: a) particle locations at five minute intervals; b) contours of vertical velocity; c) average profiles of dissipation rate  $\epsilon$  ( $W\ kg^{-1}$ ). Background turbulence dissipation rate in Saanich Inlet is set at  $10^{-9}\ W\ kg^{-1}$  following measurements by Kunze et al. (2006). In the upper few meters dissipation rate exceeded  $10^{-9}\ W\ kg^{-1}$  due to surface wind stress and has been removed.

The case with low concentration of particles (1000 individuals/m<sup>3</sup>) showed almost no change in dissipation rate of turbulent kinetic energy over background turbulence during particle migration; though, there were still relatively small fluctuations of vertical velocity on the contour plots (Fig. 42). Note that the background turbulence dissipation rate in the model without particles was comparable to or lower than the measurement noise reported by Kunze et al. (2006).

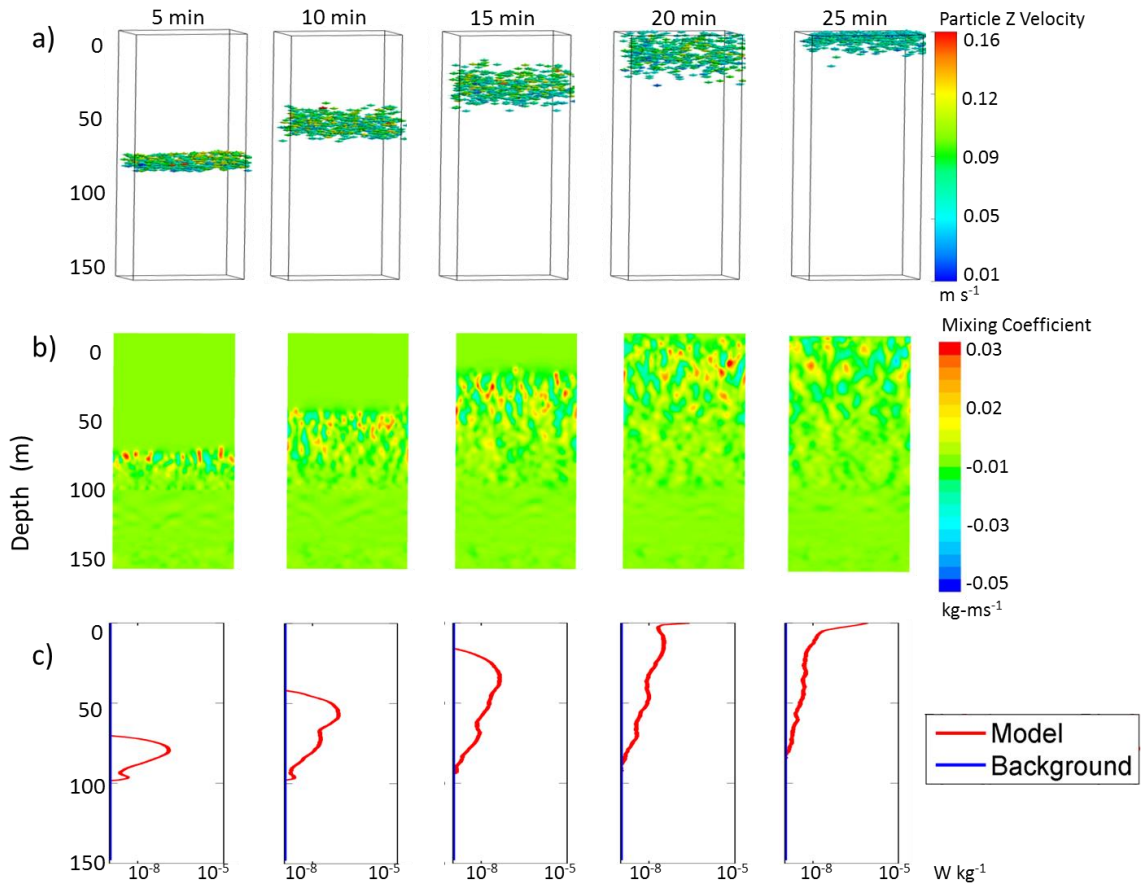


**Figure 41.** Same as in Figure 40, but by injecting 5000 particles m<sup>-3</sup>.

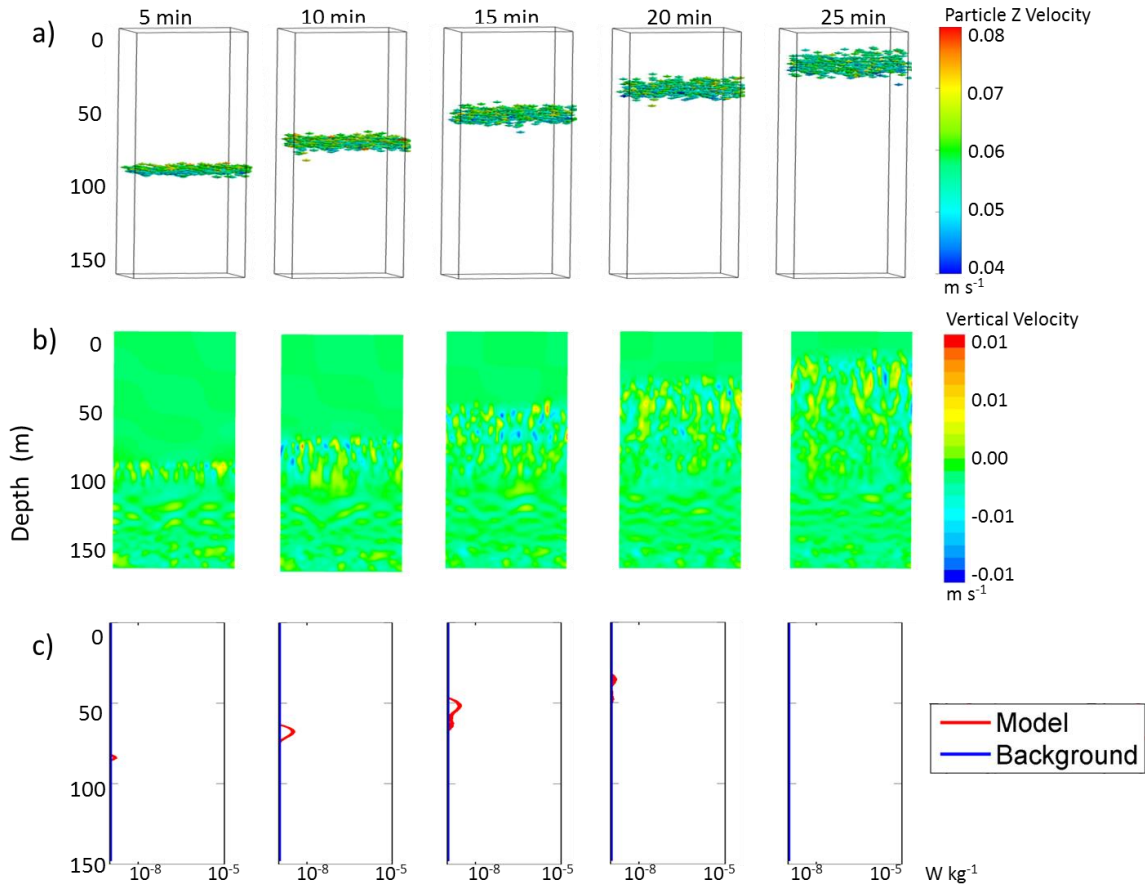


**Figure 42.** Same as in Figure 40, but by injecting 1000 particles  $\text{m}^{-3}$ .

These results suggest that DVM of zooplankton can cause a measurable increase of dissipation rate of turbulent kinetic energy in the upper layer of the ocean, though strongly dependent on zooplankton concentration. However, there may be some discrepancies between simulated and measured dissipation rates during migration. The model results show horizontally averaged dissipation rate over the 50 m by 50 m model domain, while measurements of turbulence are instantaneous profiles (Kunze et al. 2006). Zooplankton undergoing DVM tend to be spatially inhomogeneous, which leads to locally increased areas of turbulence in the ocean.

Modeling the zooplankton as buoyant ridged spherical particles may result in either the overestimation or underestimation of turbulence generation. Swimming behavior is not taken into consideration in this model, which could cause the underestimation of turbulence (Huntley and Zhou 2004). However, this work also does not account for the



streamlined body shape of most migrating zooplankton, which could cause overestimation of turbulence.

Mixing efficiency depends on the length scale of turbulence generated, relative to the vertical buoyancy scale (Visser 2007). As the length scale of the generated turbulence increases, the mixing efficiency increases (Kunze 2011). Therefore, the mixing efficiency from turbulence generated by an individual organism is likely very low. However, turbulence generation by organisms with a collective behavior depends on volume and concentration of organisms, as well as their shape and orientation (Katija 2012), increasing the mixing efficiency over a single organism. This model likely oversimplified the effect of collective behavior on turbulence generation by the use of spherical particles.

### **4.3 Modeling of DVM in the Gulf of Mexico during oil spill**

The above-described *ANSYS Fluent* CFD model has also been applied to the Gulf of Mexico using the same domain and mesh that were used in the Straits of Florida simulation. Initial conditions were determined from ADCP and CTD data taken aboard the R/V *F.G. Walton Smith* during the CARTHE LAgrangian Submesoscale ExpeRiment (LASER) cruise in January and February 2016. Several CTD casts were taken during this month-long cruise at different locations, including near the mouth of the Mississippi River. The CTD data from the cast on 29 January 2016, at 20:00 UTC near the mouth of the Mississippi River was used to determine the initial density profile and ADCP data from a one-hour average around the time of the CTD cast have been used to determine the initial velocity profile (Fig. 43).

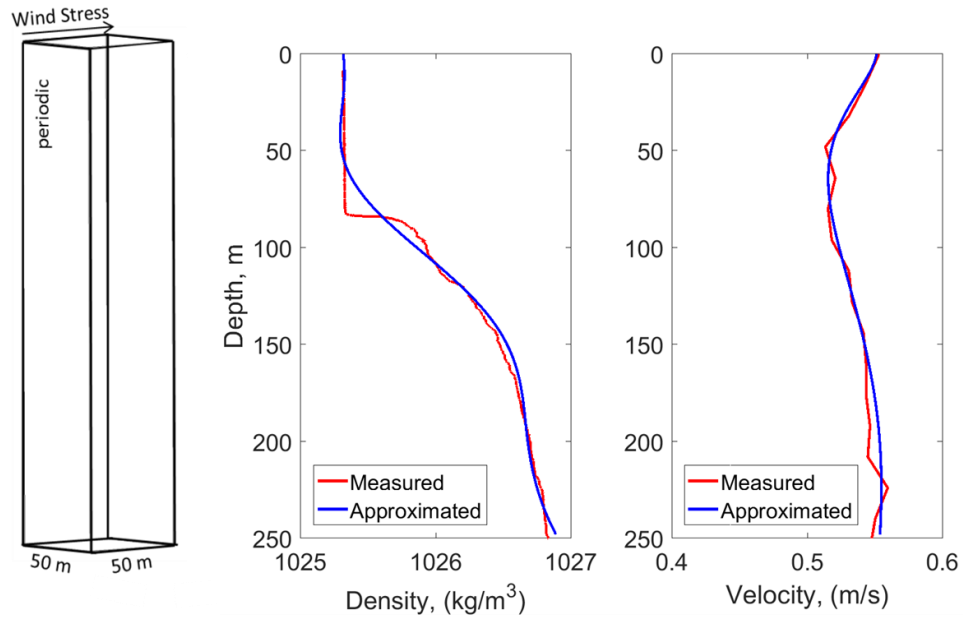


**Figure 43.** Gulf of Mexico CFD model setup. The domain was a 50 x 50 x 250 m box representing a section of the Gulf of Mexico. Initial density and velocity profiles were determined from interpolated profiles of ARGO floats.

Results of the simulation with an extreme concentration of particles ( $10,000 \text{ org/m}^3$ ) show an increase in dissipation rate of turbulent kinetic energy by two to three orders of magnitude over background turbulence (Fig. 44c). The background turbulence for the Straits of Florida (reported by Gregg et al. (1999) as  $10^{-8} \text{ W kg}^{-1}$ ) was used as a preliminary estimate. More research needs to be done to determine the appropriate level of background turbulence for this location. Additional concentrations of zooplankton will be tested in the model to determine their effect on turbulence dissipation.

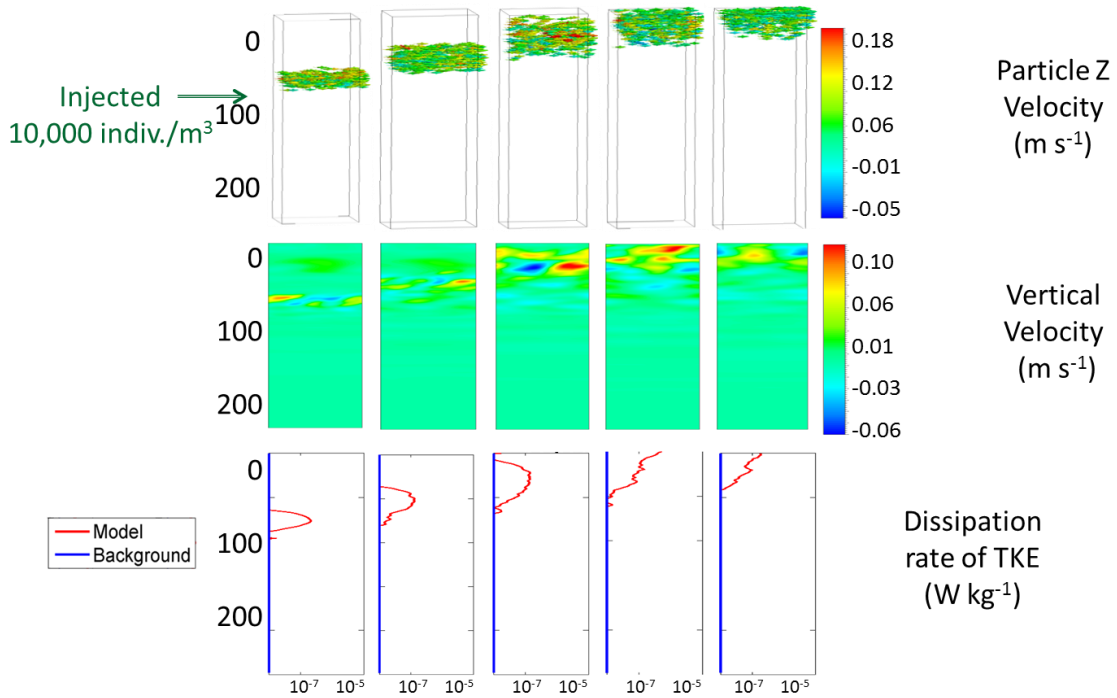


**Figure 44.** Modeling turbulence produced by DVM of zooplankton in the Gulf of Mexico by injecting 10,000 positively buoyant particles with 0.01 m diameter at 100 m: (a) particle locations at five-minute intervals; (b) contour plots of vertical velocity ( $\text{m s}^{-1}$ ); (c) average profiles of dissipation rate  $\epsilon$  ( $\text{W kg}^{-1}$ ). Background turbulence dissipation rate in the Straits of Florida is set at  $10^{-9} \text{ W kg}^{-1}$  following measurements by Kunze et al. (2006).

Propulsion speed of some organisms may be somewhat changed because of buoyancy effects due to varying salinity stratification in the upper layer of the ocean. The highly viscous nature of oil emulsions may slow zooplankton migration and increase dissipation rate due to upward migration. The presence of oil emulsions, however, can have a more dramatic effect on the DVM of zooplankton (with dire consequences for the marine ecosystem).

#### 4.4 Modeling of Magnetic Signature of DVM

In order to simulate the magnetic signature of DVM of zooplankton, the *ANSYS Fluent MHD* model was applied to the hydrodynamic solution (“frozen” velocity field) as described in Section 4.1. The Earth’s magnetic field in South Florida ( $B_x = 2.51 \times 10^{-5} \text{ T}$ ,  $B_y = 3 \times 10^{-6} \text{ T}$ , and  $B_z = -3.59 \times 10^{-5} \text{ T}$ , <http://www.ngdc.noaa.gov/geomag-web>) is applied as an external magnetic field. Material properties of the seawater are set as follows:

electrical conductivity is  $4.788 \text{ S m}^{-1}$  and magnetic permeability is  $1.257 \times 10^{-6} \text{ H m}^{-1}$ . The bottom and top of the domain had a conducting boundary conditions with conductivity of  $0.4 \text{ S/m}$  and  $5.5 \times 10^{-15} \text{ S/m}$ , respectively. All other walls are set as insulating boundaries. The calculation is performed with a very small time-step size (*e.g.*,  $0.001 \text{ s}$ ) for a single time-step for 1000 iterations in order to ensure convergence of the magnetic solution.

The MHD model has been applied to the Straits of Florida simulations with extreme and low concentrations of zooplankton. The MHD model results indicate that migrating zooplankton can cause magnetic fluctuations of approximately  $70 \text{ pT}$  in the case of an extreme concentration of zooplankton undergoing migration and approximately  $15 \text{ pT}$  for a low concentration of zooplankton (Fig. 45). This signal is relatively small but is well within the range of modern magnetometers. DVM also produces an electric signal. The extreme concentration of zooplankton produces an electric signal of approximately  $10 \mu\text{V/m}$  and the low concentration of zooplankton produces an electric signal of  $15 \mu\text{V/m}$  (Fig. 46).

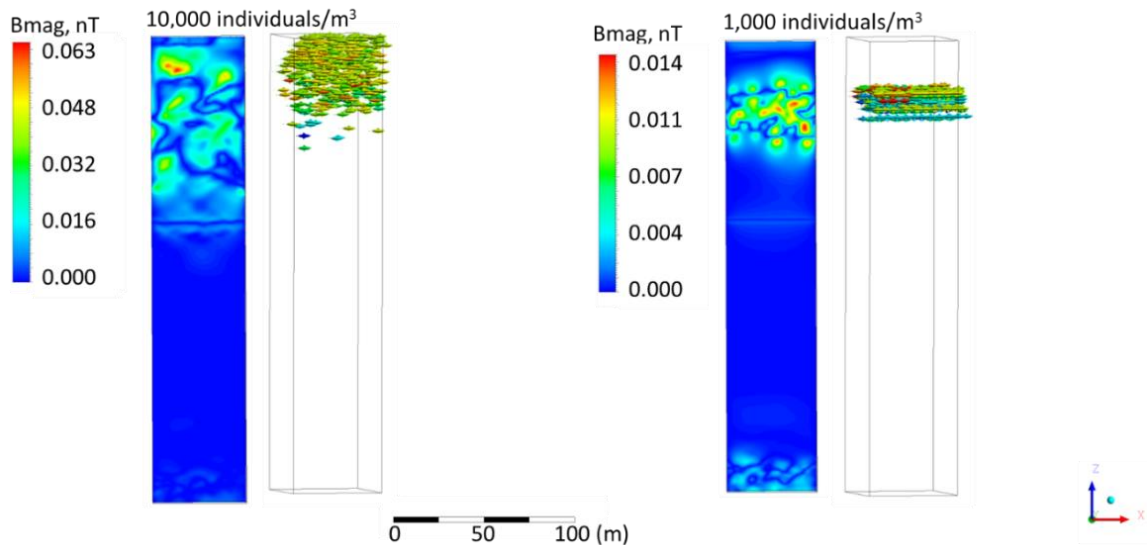


**Figure 45.** Magnetic signature of bio-turbulence 20 min after injecting positively buoyant particles with  $0.01 \text{ m}$  diameter at  $100 \text{ m}$ : (Left) Magnetic signature of extreme concentration of zooplankton and particle location 20 min after injection; (b) magnetic signature of low concentration of zooplankton and particle location 20 min after injection.

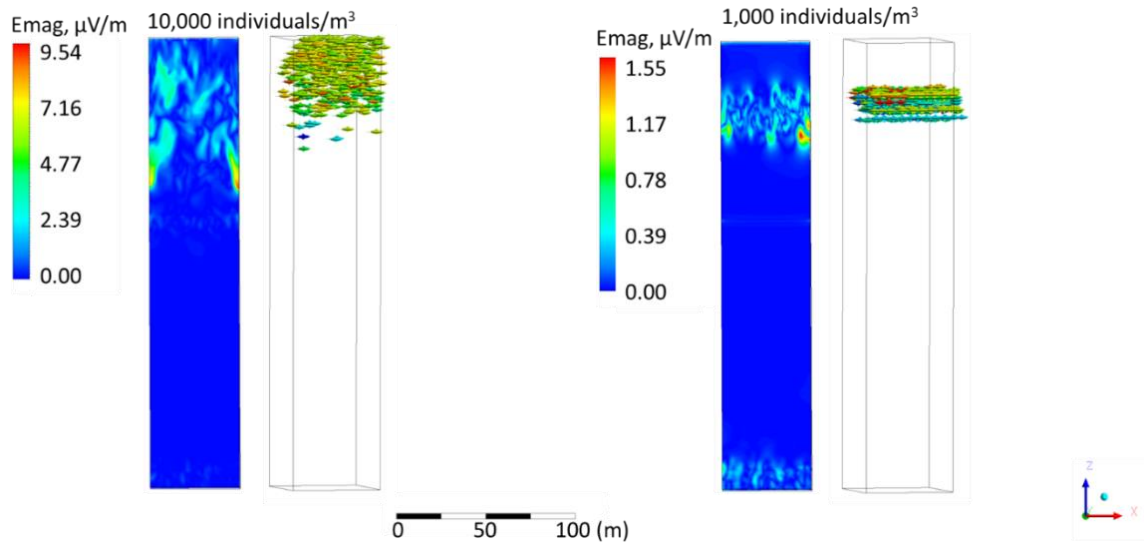


**Figure 46.** Electric signature of bio-turbulence 20 min after injecting positively buoyant particles with 0.01 m diameter at 100 m: (Left) Electric signature of extreme concentration of zooplankton and particle location 20 min after injection; (b) electric signature of low concentration of zooplankton and particle location 20 min after injection.

## 5. Comparison of magnetic signature of DVM to magnetic signature of other fine-scale oceanographic processes

Hydrodynamic simulations using *ANSYS Fluent* have been conducted exploring other fine-scale oceanographic processes such as surface waves, internal wave soliton, internal wave breaking on the continental slope, freshwater lenses, and Langmuir circulation. MHD simulations have also been conducted for these processes (Soloviev et al. 2015a, Soloviev et al. 2018) using the verified *Fluent* MHD model. The magnitude of the magnetic signature produced by the DVM of zooplankton with these other oceanographic magnetic sources are compared below.

### 5.1 Idealized surface waves

Ocean surface waves are an important mechanism for the generation of magnetic signatures. The orbital motion of seawater produced by wind-driven surface waves (Warburton and Caminiti 1964) and ocean swell (Weaver 1965) in the Earth's magnetic field creates a measurable magnetic signature above and below the water's surface. The

magnetic signature produced by these waves is dependent on both wavelength and amplitude.

Soloviev et al. (2015a) compared the *ANSYS Fluent* MHD simulation of surface waves with the analytical solution by Warburton and Caminiti (1964). This work has updated the simulation of the magnetic signature using the *Fluent* MHD model (Section 3). The domain for this simulation was 500 m long, 300 m wide, and 600 m high. The water layer was 300 m deep and the air layer was 300 m high. The mesh resolution was 5 m in the horizontal and 0.75 m in the vertical at the air-sea interface, increasing in both directions away from the interface. Surface waves with an amplitude of 2 m and a wavelength of 36 m were imposed in this simulation using a wave boundary condition (Fig. 47). The bottom boundary had a no slip condition, while all other boundaries were slippery.

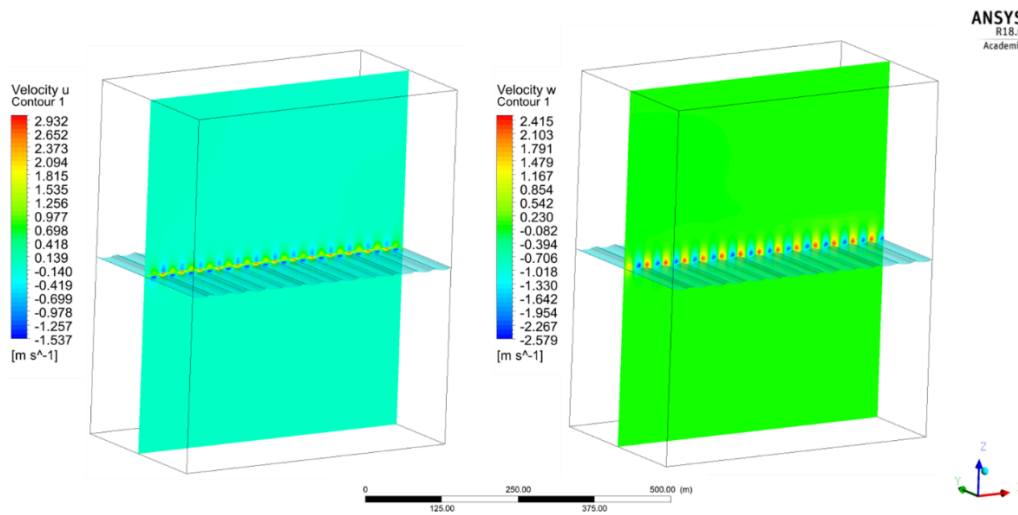


**Figure 47.** CFD simulation of 2 m amplitude, 36 m long surface waves. Contour plots of U velocity (left) and W velocity (right) with an isosurface of density showing the air-sea interface.

The verified *ANSYS Fluent* MHD model was applied to the hydrodynamic calculation with the Earth’s magnetic field set as follows:  $B_x=2.51 \times 10^{-5}$  T,  $B_y=3 \times 10^{-6}$  T,  $B_z=-3.59 \times 10^{-5}$  T. The electrical conductivity of water and air were set to 4.788 S/m and  $5.5 \times 10^{-15}$  S/m, respectively. The bottom boundary had a conducting wall, with electrical conductivity of 0.4 S/m. The *ANSYS Fluent* MHD model produced the magnetic

signature on the order of 1 nT, which is in reasonable agreement with the analytical solution (Fig. 48). As mentioned in Section 2.2, the *ANSYS Fluent* MHD model was missing two terms in the Maxwell equations, which deal with changing electrical conductivity. In this simulation, those additional terms have been recovered with a UDF, but there was no substantial change to the solution.

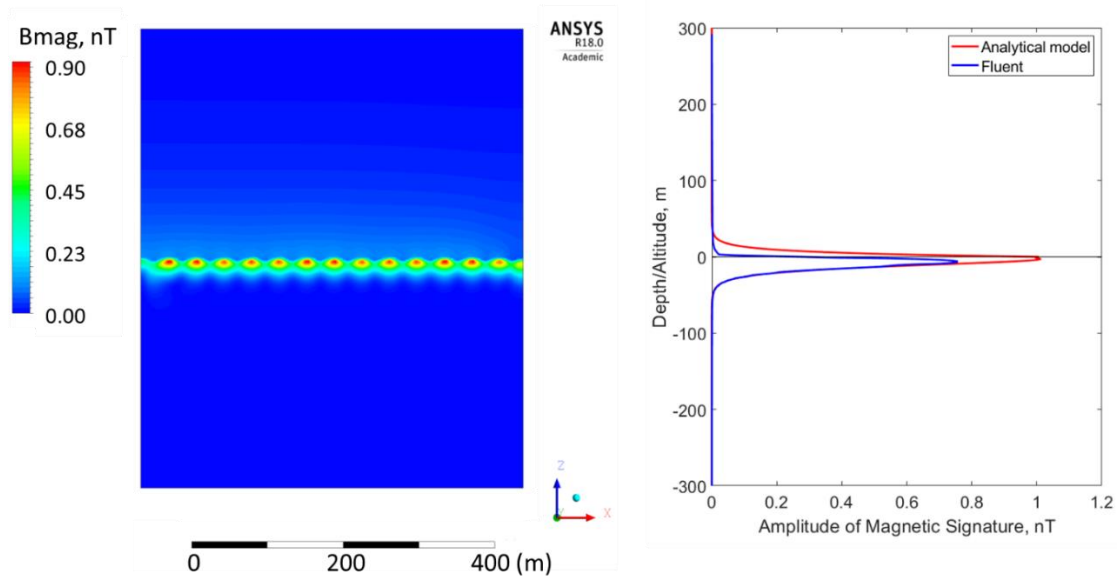


**Figure 48.** Magnetic signature of surface waves. (Left) Center plane, side-view contour plot of the magnetic signature,  $B_0$ , produced by surface waves. (Right) Amplitude of the magnetic signature of surface waves.

## 5.2 Internal wave soliton breaking on the continental slope

It is well known that internal waves in the ocean can interact with continental slopes. Under certain conditions, energy produced by breaking internal waves is concentrated near the seafloor, creating boundary layer instabilities and thus vortices that stir up sediment and produce layers of suspended particles, known as nepheloid layers (Cacchione and Drake 1986). Nepheloid layers are a prominent feature on continental margins worldwide and can significantly contribute to the transportation of matter and energy in these environments (Eisma 1993). The thickness of this layer depends on the current velocity produced by wave breaking and the type of sediment present in the area.

A hydrodynamic simulation of an idealized internal wave soliton breaking on the continental slope was run and the effect of the creation of a nepheloid layer was explored using a DPM model (Section 2.1). The domain was 2000 m long, 200 m wide, and 275 m high, with a 13.2° slope representing the continental slope. The mesh resolution was 5 m in all directions. There was a no slip boundary condition on the bottom of the domain including the slope. All other boundaries were slippery. The model was initialized with a 14.6°C temperature anomaly, 1.25 psu salinity anomaly, and resulted in a 4.5 kg/m<sup>3</sup> density anomaly (Fig. 49). This anomaly propagated as an internal wave soliton. As the wave broke on the continental slope, the Lagrangian particles were entrained in the gravity current head and formed a nepheloid layer.

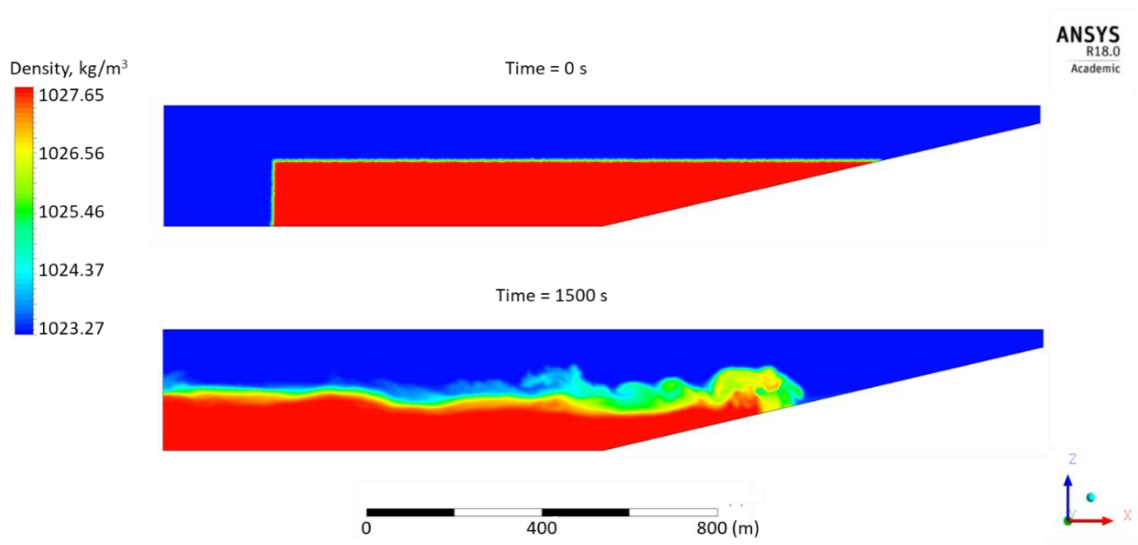


**Figure 49.** Initial condition for the internal wave breaking on the continental slope. (Top) Center plane contour plot of the initial density anomaly; (bottom) center plane contour plot of density at the time of the MHD simulation.

At the time of wave breaking on the slope, the verified MHD model was run on the “frozen” velocity field to determine its magnetic signature. The Earth’s magnetic field was set to be that in Dania Beach, FL ( $B_x=3 \times 10^{-6}$  T,  $B_y=-2.51 \times 10^{-5}$  T,  $B_z=-3.59 \times 10^{-5}$  T). Note, the difference in the Earth’s field in this simulation compared to the others in this section is due to the coordinate system. Here x is west and y is south. In other simulations, x is north and y is west. The electrical conductivity of water and air were 4.788 S/m and  $5.5 \times 10^{-15}$  S/m, respectively. The bottom boundary had a conducting



boundary condition with 0.4 S/m conductivity. The magnetic signature produced by the internal wave breaking was approximately 1.4 nT and the electrical signature was approximately 60  $\mu\text{V/m}$  (Fig. 50). The highest magnetic signature produced by this wave breaking was in the area of highest shear and very little signal was observed near the bottom of the domain.

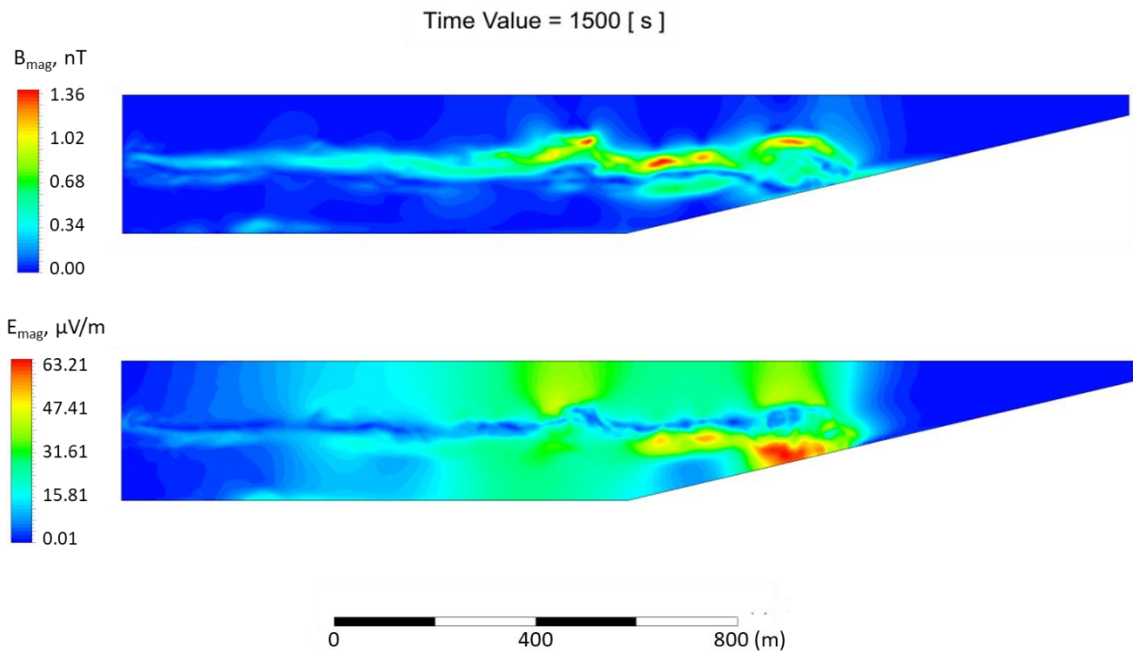


**Figure 50.** Center plane contour plot at 1500 s of (top) magnitude of the magnetic field fluctuations and (bottom) magnitude of the electric field fluctuations due to an internal wave breaking on the continental slope.

### 5.3 Freshwater lens spreading

Convective rains and river runoff can produce freshwater lenses on the ocean surface. The large density gradient between the lens and its surrounding environment produce strong pressure gradients causing the lens to spread laterally as a gravity current (Soloviev and Lukas 1997). The water motion of spreading gravity current can produce a magnetic signature. The stronger the density difference, the faster the lens will spread, and presumably, the larger the magnetic signature it will produce.

A hydrodynamic simulation was conducted to explore the dynamics of the propagation freshwater lenses produced by river runoff similar to that observed in the

Mississippi River Delta (Soloviev et al. 2015b). The domain for this simulation was 1000 m long, 40 m wide, and 40 m deep with a 1 m mesh resolution in the y-direction, 50 cm in the x-direction, and 12 cm in the vertical at the top of the domain, and expanding to the bottom. The model was initialized with an initial 6.1°C temperature anomaly and a 5.4 psu salinity anomaly, resulting in a 2.5 kg/m<sup>3</sup> density anomaly representing a freshwater lens produced by river runoff (Fig. 51). Wind stress was applied, which was equivalent to 15 m/s (Fairall et al. 2003). The freshwater plume spread like a gravity current (Fig. 51 bottom).

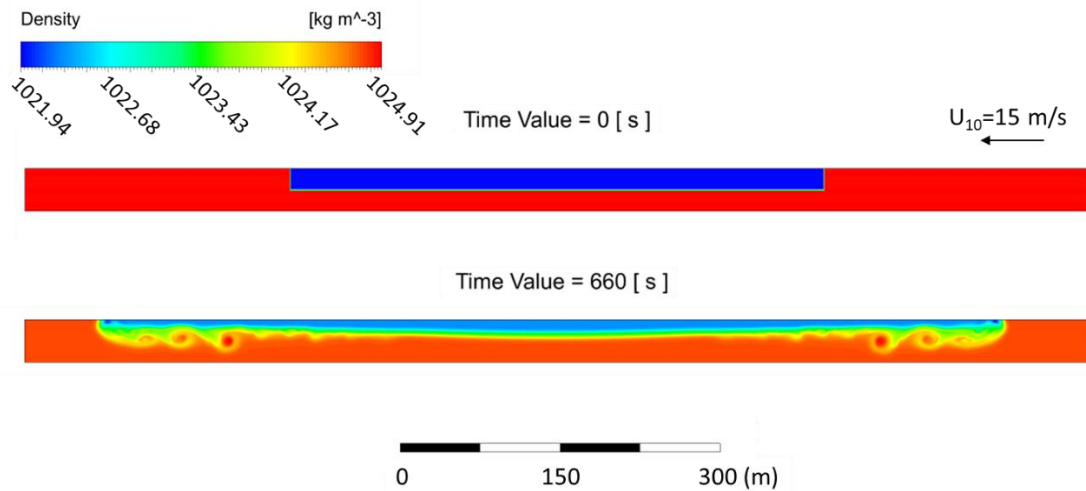


**Figure 51.** Model setup of freshwater lens simulation. Top shows the density center plane contour plot at the model initialization. Bottom shows the density center plane contour after the freshwater lens has spread for 660 s.

The MHD model was then applied to the “frozen” velocity field after 660 s of the CFD simulation. Water conductivity was 4.788 S/m. The magnetic boundary conditions were insulating on all walls. The Earth’s magnetic field was set as follows:  $B_x=2.51 \times 10^{-5}$  T,  $B_y=3 \times 10^{-6}$  T,  $B_z=-3.59 \times 10^{-5}$  T. The magnetic signature of freshwater lens propagation from this hydrodynamic simulation is approximately 0.53 nT (Fig. 52b) (Soloviev et al. 2017). The electric signature produced by this freshwater lens was 10.41  $\mu$ V/m (Fig. 52c).

This simulation was conducted for freshwater lens produced by river runoff. In areas of larger river run off with a larger density anomaly, this signal may be much stronger.

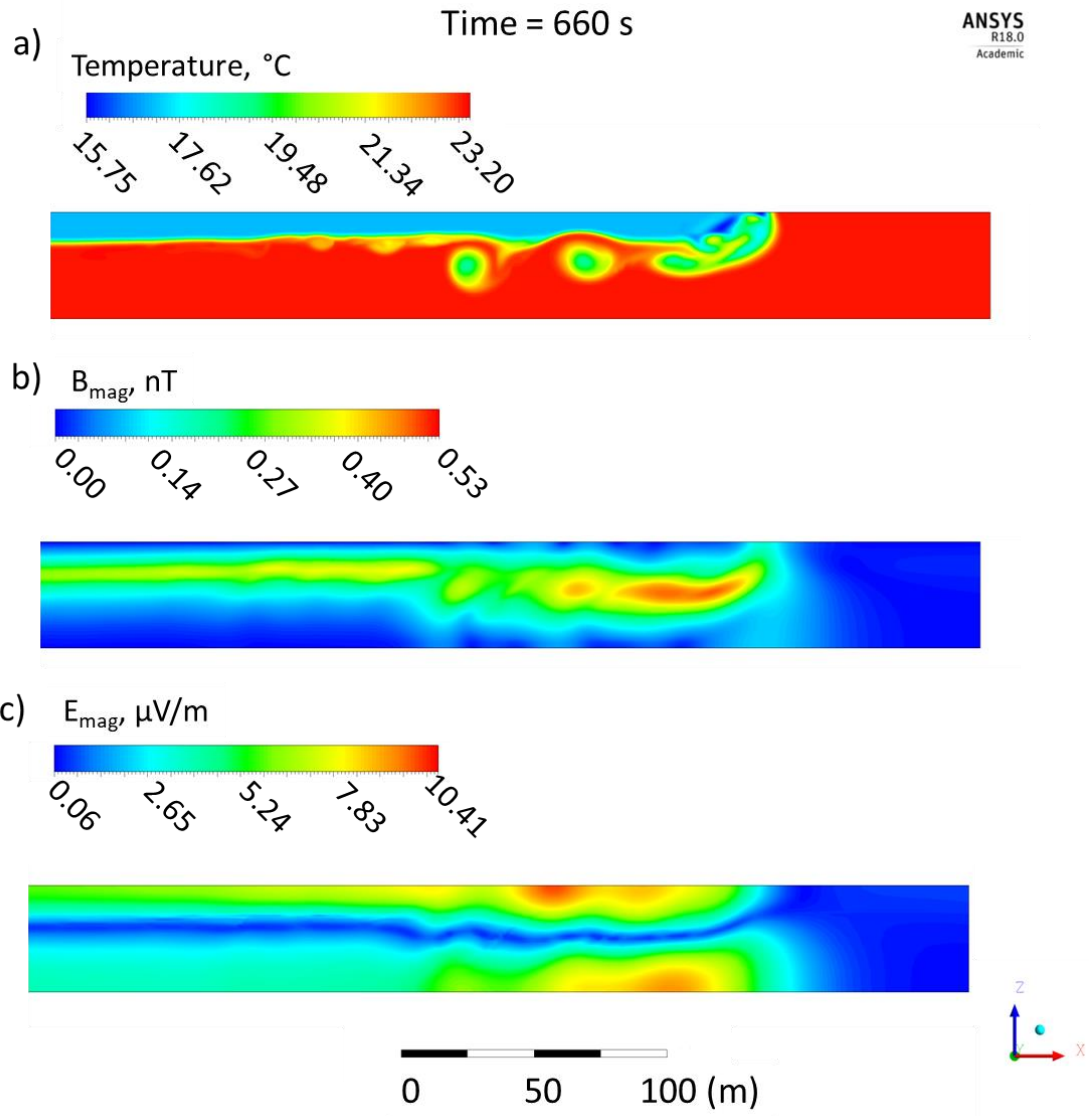


**Figure 52.** Magnetic signature of freshwater lens after 660 s of propagation. Center plane contour plot of a) temperature, b) magnitude of the magnetic signature of the freshwater lens spreading, and c) electric signature of the lens spreading.

#### 5.4 Langmuir circulation and ramp-like structures

Langmuir cells and ramp-like structures are an important feature in the upper ocean turbulent boundary layer. Langmuir cells and ramp-like structures are believed to vertically transfer an appreciable portion of the momentum, heat, gases, pollutants (*e.g.*, oil), and other substances in the upper layer of the ocean. Soloviev and Dean (2015) uses computational fluid dynamics tools to model Langmuir cells and ramp-like structures

coexisting in space, though intermittent in time by injecting shear-free turbulence due to breaking waves by altering the water viscosity as a material property in the near-surface layer of the ocean.

A 3D CFD simulation with an LES turbulence model has been conducted to simulate Langmuir circulation and ramp-like structures for developing seas, including high wind speed conditions (Soloviev and Dean 2015). This model does not include the Stokes drift term and thus is not locked to the wave direction. The domain was 500 m long, 200 m wide, and 80 m deep with 1 m horizontal mesh resolution, and a 0.1 m vertical mesh resolution near the surface, increasing with depth. A periodic boundary condition was set along the numerical domain. Wind stress to the equivalent of approximately  $9 \text{ m s}^{-1}$  wind speed at 10 m height (Fairall et al. 2003). The material viscosity of water in the wave stirred and turbulent diffusion layers corresponding to developing seas were set according to

$$\mu = \begin{cases} \mu_0, & z \geq -0.2H_s \\ \mu_m + (\mu_0 - \mu_m)(z + 2H_s) / (1.8H_s), & -0.2H_s > z > -2H_s \\ \mu_m, & z \leq -2H_s \end{cases} \quad (53)$$

as follows:  $H_s = 1 \text{ m}$ ,  $\alpha = 4.5$ ,  $\mu_0 = 1 \cdot 10^{-6} \text{ m s}^{-2}$ ,  $\mu_m = 1.8 \cdot 10^{-2} \text{ m s}^{-2}$ . A no shear boundary condition was applied at the bottom and side walls of the numerical domain. No stratification effects have been considered in this case. The CFD model is able to reproduce both Langmuir cells and ramp-like structures coexisting in space though intermittent in time (Fig. 53).

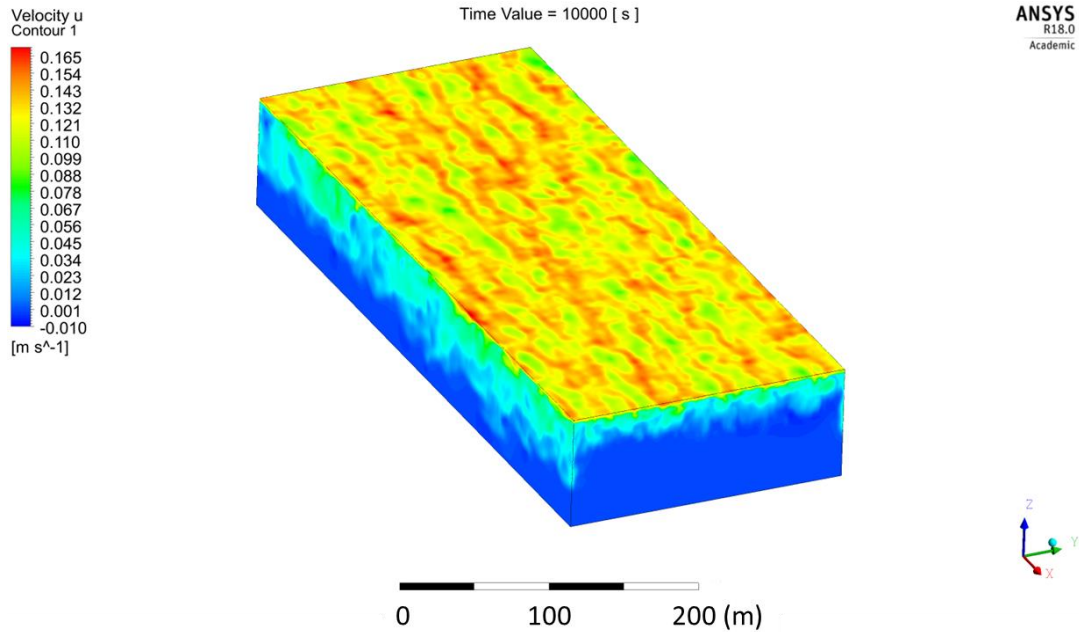


**Figure 53.** CFD simulation of Langmuir cells and ramp-like structures. Contour plots of U velocity after 10,000 s.

The verified MHD model was applied to the “frozen” hydrodynamic solution at 10,000 s once Langmuir circulation had developed. The Earth’s magnetic field for the Dania Beach, FL area was set as follows:  $B_x=2.51 \times 10^{-5}$  T,  $B_y=3 \times 10^{-6}$  T,  $B_z=-3.59 \times 10^{-5}$  T. Electrical conductivity of the water was 4.788 S/m and the bottom boundary was set to be conducting with a conductivity of 0.4 S/m. The coherent structures produced a magnetic signature on the order of 0.07 nT (Fig. 54) (Soloviev et al. 2015a).

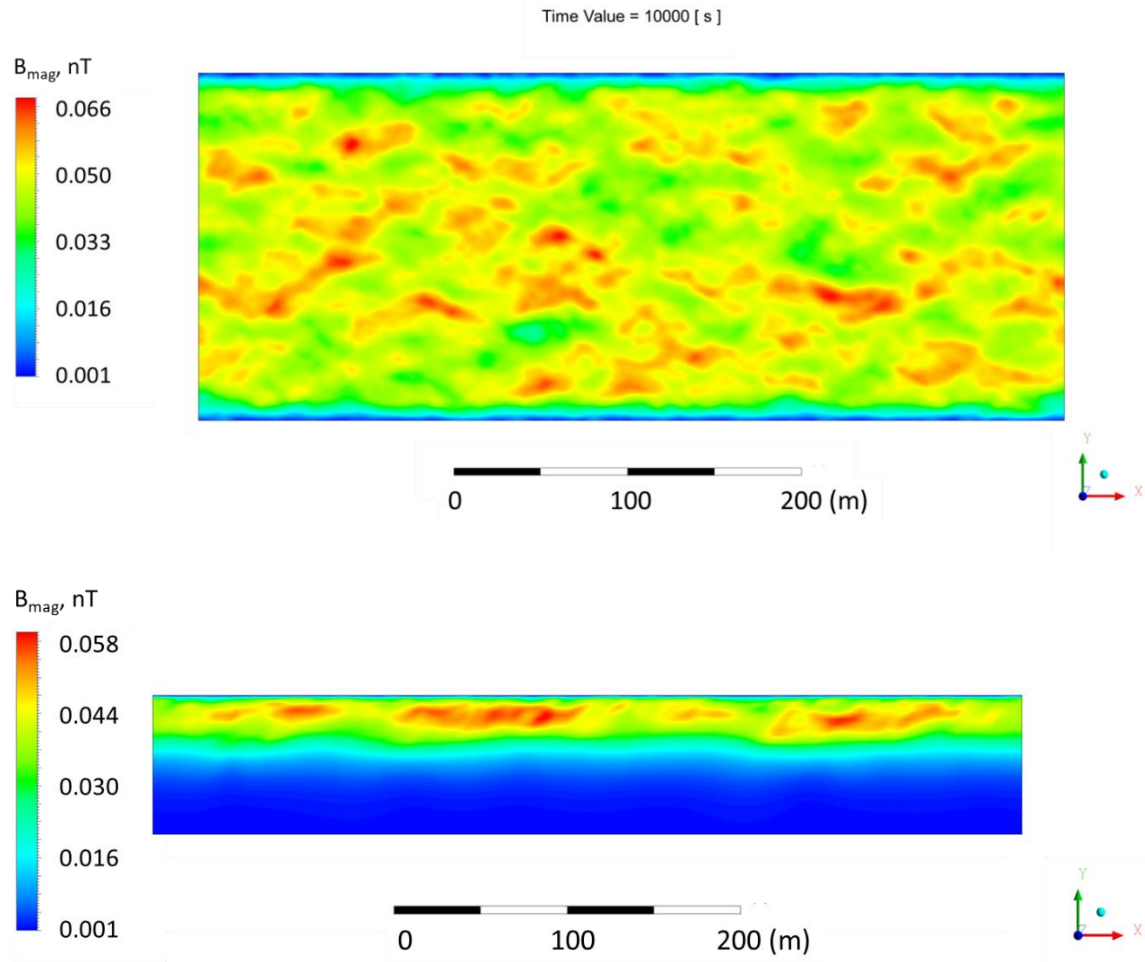


**Figure 54.** Magnetic signature of Langmuir circulation. (Top) Contour plot at 10 m depth (top view) of the magnetic signature of Langmuir circulation. (Bottom) Contour plot in the center plane of the domain (side view) of the magnetic signature of Langmuir circulation.

### 5.5 Comparison of magnetic signature of different processes

The results described in Section 4.4 show that DVM of zooplankton produces a magnetic signature on the order of 0.1 nT. This result indicates that the magnetic signal of DVM of zooplankton is comparable with that produced by Langmuir circulation and ramp-like structures. Internal wave solitons produce the largest signal, on the order of 1-10 nT, of the processes studied in this work. Surface waves produce a magnetic signature on the order of 1 nT, freshwater lenses produce a magnetic signature of approximately

0.5 nT (Table 2). Under different initial conditions the magnetic signature produced by these processes may be somewhat different.

**Table 2.** Comparison of the typical magnetic signature produced by different small-scale oceanographic processes as produced by the verified MHD model.

Oceanographic Process	Maximum Magnetic Signature (nT)
Diel vertical migration of zooplankton	0.07
Surface waves	0.9
Idealized internal wave soliton	10
Internal wave soliton breaking on continental slope	1.4
Freshwater lens	0.5
Langmuir circulation	0.07

## 6. Conclusions

In this work, a computational fluid dynamics (CFD) model was used to determine the magnetic signature of various small- and fine-scale oceanographic processes. These types of processes inherently involve three-dimensional dynamics. Respectively, the model suite included the non-hydrostatic type model *ANSYS Fluent*, coupled with the MHD module, and *ANSYS Maxwell* models.

In this dissertation, substantial effort has been made in the model verification. I have had the opportunity to compare the model results with field and laboratory data. Verifications of the *Fluent* CFD and MHD and *Maxwell* models have been conducted by comparing with the laboratory experiments, and field measurements. One limitation of the MHD module is the assumption of a sufficiently conductive fluid so that the charge density and displacement current terms in Maxwell's equations can be neglected. However, the displacement current term is important for high frequency processes (*e.g.*, radio waves). In this dissertation work, I am focused on the magnetic signature of oceanic processes with relatively low frequencies, and the displacement term does not appear to be prominent, even in the air. I, however, have not been able to verify the MHD model

above the sea surface, due to the lack of proper available field data. The profiles in the air should be treated as non-verified model results.

The verification of the model has been conducted with the SFOMF EM Observatory field measurements during the Ambient Weather Experiment. In this test, the ADCP data were used for the MHD model initialization. The magnetic signature of the ocean circulation including internal wave solitons produced by the model was consistent with the field measurements of the total magnetic field near the seafloor.

The CFD model was also compared with the traditional, analytical models of electromagnetic signatures of surface and internal waves (Weaver 1965, Beal and Weaver 1970, Podney 1975, Lilley et al. 2004). In the case of surface waves, the computational model is close to the analytical solution in water. There is, however, some difference in the air, which is likely because the analytical models incorrectly extend the transverse component of the magnetic field into the air (Beal and Weaver 1970, Podney 1975). Weaver (1965) does not reveal the magnetic model results in the upper few meters of the ocean by setting a logarithmic scale for depth.

In the case of the model verification with the analytical theory of internal waves, I considered three cases including internal waves with 50 m, 500 m, and 1000 m wavelengths. For the 50 m internal waves, the computational model was consistent with the analytical solution. For longer waves, 500 m and 1000 m, there is a significant difference between the computational and traditional models. This difference is explained by the two factors that are not included in the traditional models. The first factor is the effect self-inductance in seawater. The second factor is the structure of the bottom turbulent boundary layer. Both of these factors appear to be significant for the magnetic signature of oceanographic processes. In contrast to the traditional, analytical models, the MHD model is able to account for both of these factors.

The suite of computational models was also verified in the laboratory conditions. For this purpose, we conducted a series of laboratory experiments at the UM RSMAS air-sea interaction facility SUSTAIN including saltwater, freshwater, and an empty tank (Kluge et al. 2018). These experiments revealed another feature, the difference in magnetic permeability between the air and water, which is ignored in the traditional, analytical



models. This feature was modeled using *ANSYS Maxwell* and demonstrated consistency with the observations (Soloviev and Dean 2018).

This suite of models was then applied to evaluate the magnetic signature of DVM of zooplankton, surface waves, internal wave solitons, freshwater lens spreading, and Langmuir circulation. The comparison of the magnetic signature of these processes provided in Table 2 gives a quantification of the magnetic noise induced by hydrodynamic processes. These evaluations have been done for typical environmental conditions. In other environmental conditions, their magnetic signature may be somewhat different. However, the suite of computational models developed in this dissertation allows estimation of the magnetic signature of submesoscale and fine- and small-scale oceanographic processes in virtually any environmental conditions. I anticipate the result of this study will have Naval, environmental, and oil exploration applications.

As a recommendation for future development of the EM Observatory, the velocity measurements in the bottom boundary layer should be made with higher vertical resolution. The cabled ADCPs (3 m vertical resolution with a 7 m gap above the bottom) are not sufficient to resolve convergence/divergence motions of seawater near the bottom, which may affect the simulation of the magnetic signature of the oceanographic processes near the bottom. The vertical resolution of current velocity measurements should be sufficient to resolve the bottom boundary layer (*e.g.*, using a downward-looking ADCP as implemented on the NSU mooring). The local gradients near the bottom are expected to be increased, resulting in a higher magnetic signature. Additionally, the 3D velocity structure should be measured to account for the direction of internal wave soliton propagation. The higher resolution mesh and larger domain needed to incorporate this additional data requires increased computational power, which is expected to be available in the future.

## **Acknowledgements**

I thank my committee members, Professors Alexander Soloviev (NSU), Tracey Sutton (NSU), John Holmes (NSWCCD), and Tamay Ozgökmen (UM) for their assistance in the completion of this dissertation work. I am grateful to Dr. Brian Glover (NSWCCD), Brad Nelson (AS), Eric Nieves (FAU), John Kluge (NSU), Dr. William Venezia (NSWCCD), George Valdes (NSWCCD), Dr. Richard Dodge (NSU), Michael Farrar (NSWCCD), and Jon Wood (ODT) for help in the problem formulation, access to data, data processing, and fruitful discussions of this work. I thank NAVAIR, NSWCCD, ONR, and CARTHE/GoMRI for funding support and effective management of the projects that allowed for this dissertation work.

## References

- Andersen, V., Nival, P., 1991: A model of the diel vertical migration of zooplankton based on euphausiids. *Journal of Marine Research* 49, 153-175.
- Antonia, R.A., Chambers, A.J., Friehe, C.A., Van Atta, C.W., 1979: Temperature ramps in the atmospheric surface layer. *Journal of Atmospheric Science* 36, 99–108.
- ANSYS, Inc., 2013: ANSYS FLUENT 15.0 Theory Guide, Canonsburg, Pa.
- Beal, H.T., Weaver, J.T., 1970: Calculations of magnetic variations induced by internal ocean waves. *Journal of Geophysical Research*. 75, 6846-6852.
- Baumann-Pickering, S., Checkley, D.M., Demer, D.A., 2016: Do top predators cue on sound production by mesopelagic prey? *Oral presentation at Ocean Sciences Meeting in New Orleans, LA*.
- Botsford, L.W., Moloney, C.L., Hastings, A., Largier, J.L., Powell, T.M., Higgins, K., Quinn, J.F., 1994: The influence of spatially and temporally varying oceanographic conditions on meroplanktonic metapopulations. *Deep Sea Research II* 41, 107-145.
- Box, G.E.P., Draper, N.R., 1987: *Empirical model-building and response surface*. John Wiley & Sons, Ltd. P. 424.
- Cacchione, D.A., Drake, D.E., 1986: Nepheloid layers and internal waves over continental shelves and slopes, *Geo-Marine Letters*, 6, 147–152.
- Catton, K.B., Webster, D.R., Kawaguchi, S., Yen, J., 2011: The hydrodynamic disturbances of two species of krill: implications for aggregation structure. *The Journal of Experimental Biology* 214, 1845-1856.
- Chave, A.D., 1984: On the electromagnetic fields induced by oceanic internal waves, *Journal of Geophysical Research* 89, 10 519–10 528.
- Cox, C.S., 1962: Internal waves in *The Sea*, vol. 1, part 2, edited by M. N. Hill, chap. 22, John Wiley, New York, 1962.
- Dean, C.W., Soloviev, A.V., Helber, R., 2016a: Freshwater Lenses, Double Diffusion, and Cabbelling in the Near-Surface Layer of the Ocean. *Presented at the 2016 Ocean Sciences Meeting*, 21-26 February, 2016, New Orleans, LA.
- Dean, C.W., Soloviev, A.V., Hirons, A.C., Frank, T., Wood, J., 2016b: Biomixing due to diel vertical migration of zooplankton: Comparison of computational fluid dynamics model with observations. *Ocean Modelling* 98, 51-64.

- Dean, C.W., Soloviev, A.V., 2018: Modeling the magnetic signature of diel vertical migrations of zooplankton. *Paper presented at OCEANS 2018*, 22-25 October 2015, Charleston, SC.
- Delafosse, A., Line, A., Morchain, J., Guiraud, P., 2008: LES and URANS simulations of hydrodynamics in mixing tank: comparison to PIV experiments. *Chemical Engineering Research and Design* 86, 1322-1330.
- De Robertis, A., Schell, C., Jaffe, J.S., 2003: Acoustic observations of the swimming behavior of the euphausiid *Euphausia pacifica* Hansen. *ICES Journal of Marine Science: Journal du Conseil* 60, 885-898.
- Dewar, W.K., Bingham, R.J., Iverson, R.L., Nowacek, D.P., St. Laurent, L.C., Wiebe, P.H., 2006: Does the marine biosphere mix the ocean? *Journal of Marine Research*, 64, 541-561.
- Diaz, F., Naudin, J.J., Courties, C., Rimmelin, P., Oriol, L., 2008: Biogeochemical and ecological functioning of the low-salinity water lenses in the region of the Rhone River freshwater influence, NW Mediterranean Sea. *Continental Shelf Research* 28, 1511–1526.
- Enright, J.T., 1977: Diurnal vertical migration: adaptive significance and timing. Part1. Selective Advantage: A Metabolic Model. *Limnology & Oceanography* 22, 856-872.
- Eisma, D. (1993), *Suspended Matter in the Aquatic Environment*, 315 pp. Springer-Verlag, New York.
- Fairall, C.W., Bradley, E.F., Hare, J.E., Grachev, A.A, Edson, J.B., 2003: Bulk parametrization of air-sea fluxes: updates and verification for the COARE algorithm. *J. Climate*, 16, 571-591.
- Faraday, M., 1832: Bakerian lecture: Experimental researches in electricity. *Philosophical Transactions Royal Society* London, part 1, 163-194.
- Gliwicz, M.Z., 1986: Predation and the evolution of vertical migration in zooplankton populations. *Nature* 320, 746-748.
- Gregg, M.C., 1975: Oceanic fine and microstructure. *Review of Geophysics and Space Physics* 13:586-591 and 635-636.
- Gregg, M., Winkel, D., MacKinnon, J., Lien, R., 1999: Mixing over shelves and slopes. In: Muller, P., Henderson, D. (Eds.) *Dynamics of Oceanic Internal Gravity Waves II*. Proceedings, Hawaiian Winter Workshop. DTIC Document pp. 35-42.
- Gregg, M.C., Horne, J.K., 2009: Turbulence, acoustic backscatter, and pelagic nekton in Monterey Bay. *Journal of Physical Oceanography* 39, 1097-1114.

- Hamner, W.M., 1984: Aspects of schooling in *Euphausia superba*. *Journal of Crustacean Biology* 4 (Spec. No. 1), 67-74.
- Huntley, M.E., Zhou, M., 2004: Influence of animals on turbulence in the sea. *Marine Ecology Progress Series* 273, 65-79.
- Ianson, D., Jackson, G.A., Angel, M.V., Lampitt, R.S., Burd, A.B., 2004: Effect of net avoidance on estimates of diel vertical migration. *Limnology & Oceanography* 49, 2297-2303.
- Jenkins, W.J., Doney, S.C., 2003: The subtropical nutrient spiral. *Global Biogeochemical Cycles* 17, 1110.
- Kahru, M., 1983: Phytoplankton patchiness generated by long internal waves: A model, *Mar. Ecological Progress Series*, 10, 111 – 117.
- Katija, K., 2012: Biogenic inputs to ocean mixing. *The Journal of Experimental Biology* 215, 1040-1049.
- Kluge, J.A., Soloviev, A.V., Morrison, G., Dean, C.W., Avera, W., Nelson, J.B., Valdes, G., Haus, B.K., 2018: Magnetic Signature of Surface Waves Measured in a Laboratory Experiment. *Paper presented at OCEANS 2018, 22-25 October 2015, Charleston, SC.*
- Korteweg, D.J., de Vries, G., 1895: On the change of form of long waves advancing in a rectangular canal, and on a new type of long stationary waves. *Philosophical Magazine and Journal of Science* 39, 422–443.
- Kudryavtsev, V., Shrira, V., Dulov, V., Malinovsky, V., 2008: On the vertical structure of wind-driven sea currents. *Journal Physical Oceanography* 38, 2121-2144.
- Kunze, E., Dower, J.F., Beveridge, I., Dewey, R., Bartlett, K.P., 2006: Observations of biologically generated turbulence in a coastal inlet. *Science* 313, 1768-1770.
- Kunze, E. 2011: Fluid mixing by swimming organisms in the low-Reynolds-number limit. *Journal of Marine Research*. 69, 591-601.
- Lampert, W., 1989: The adaptive significance of diel vertical migration of zooplankton. *Functional Ecology* 3, 21-27.
- Leibovich, S., 1983: The form and dynamics of Langmuir circulations. *Annual Review of Fluid Mechanics* 15, 391-427.
- Li, S., Li, M., Gerbi, G.P., Song, J.B., 2013: Roles of breaking waves and Langmuir circulation in the surface boundary layer of a coastal ocean. *Journal of Geophysical Research Oceans* 118, 5173–5187.

- Lilley, F.E.M., Hitchman, A.P., Milligan, P.R., Pedersen, T., 2004: Sea-surface observations of the magnetic signals of ocean swells. *Geophysical Journal International* 159, 565-572.
- Longuet-Higgins, M.S., Stern, M.E., Stommel, H., 1954: The electric field induced by ocean currents and waves, with applications to the method of towed electrodes, *Papers in Physical Oceanography and Meteorology* 13, 1–37.
- Lukas, R., Lindstrom, E., 1991: The mixed layer of the western equatorial Pacific Ocean. *Journal of Geophysical Research* 96, 3343-3357.
- MacKenzie, B.R., Leggett, W.C., 1993: Wind-based models for estimating the dissipation rates of turbulent energy in aquatic environments: empirical comparisons. *Marine Ecology Progress Series* 94, 207-216.
- MARELEC 2017. *A world class Marine Electromagnetics conference with an exhibition and poster session*. Retrieved from <https://www.marelec.co.uk/>.
- Massel, S.R. “Internal Gravity Waves in the Shallow Seas.” *Internal Gravity Waves in the Shallow Seas*, by Stanislaw R. Massel, Springer, 2015, 25–43.
- Matt, S., Fujimura, A., Soloviev, A., Rhee, S.H., Romeiser, R., 2014: Fine-scale features on the sea surface in SAR satellite imagery- Part 2: Numerical modeling. *Ocean Science* 110, 427-438.
- Melville, W.K., 1996: The role of surface-wave breaking in air-sea interaction. *Annual Review of Fluid Mechanics* 28, 279-321.
- Miessler, G.L. and Tarr, D.A., 2010: *Inorganic Chemistry* 3rd ed., Pearson/Prentice Hall publisher, ISBN 0-13-035471-6.
- Miles, J.W., 1981: The Korteweg-de Vries equation: a historical essay. *Journal of Fluid Mechanics* 106:131–147.
- Munk, W.H., 1966: Abyssal recipes. *Deep-Sea Research* 13, 707-730.
- Nicolle, A., Garreau, P., Liorzou, B., 2009: Modelling for anchovy recruitment studies in the Gulf of Lions (Western Mediterranean Sea). *Ocean Dynamics*, 59(6), 953-968.
- Nicoud, F., Ducros, F., 1999: Subgrid-scale stress modelling based on the square of the velocity gradient tensor. *Flow Turbulence and Combustion* 62, 183–200.
- NOAA National Centers for Environmental Information. Magnetic field calculators. Retrieved from <http://www.ngdc.noaa.gov/geomag-web>.
- Ocean Networks Canada. Data preview. Retrieved from <https://data.oceannetworks.ca/>.

- Özgökmen, T.M., Fischer, P.F., Duan, J., Iliescu, T., 2004: Three-dimensional turbulent bottom density currents from a high-order nonhydrostatic spectral element model. *Journal of Physical Oceanography* 34, 2006–2026.
- Pendry, J. B., Schurig, D., and Smith, D. R., 2006: Controlling electromagnetic fields, *Science*, 312, 1780-1782.
- PetroWiki, 2015: Oil emulsions. <http://petrowiki.org/> [http://petrowiki.org/Oil\\_emulsions](http://petrowiki.org/Oil_emulsions) (accessed 7 December 2016).
- Phillips, O.M., 1977: *The Dynamics of the Upper Ocean*. Cambridge University Press. 336 p.
- Phong-Anant, D., Antonia, R.A., Chamber, A.J., Rajagopalan, S., 1980: Features of the organized motion in the atmospheric surface layer. *Journal of Geophysical Research* 85, C1, 424–432.
- Podney, W., 1975: Electromagnetic fields generated by ocean waves. *Journal of Geophysical Research* 80: 21, 2977-2990.
- Pollard, R.T., 1977: Observations and theories of Langmuir circulations and their role in near surface mixing. In: Angel M. (ed) *A voyage of discovery: George Deacon 70th anniversary volume*, Pergamon Press, Oxford, 696 pp.
- Rousseau, S., Kunze, E., Dewey, R., Bartlett, K., Dower, J., 2010: On turbulence production by swimming marine organisms in the open ocean and coastal waters. *Journal of Physical Oceanography* 40, 2107-2121.
- Smagin, V.P., S.V. Semkin, V. N. Savchenko, 2014: Geomagnetic Field Variations Induced by Internal and Surface Waves in the Four-Layer Model of the Marine Environment. *Geomagnetism and Aeronomy* 54, 713-719.
- Soloviev, A.V., 1990: Coherent structure at the ocean surface in the convectively unstable conditions. *Nature* 346, 157–160.
- Soloviev, A., Dean, C. W., 2015: Surface Waves and Spatially Coherent Structures in the Near-Surface Layer of the Ocean. *Paper presented at 20th Conference on Atmospheric and Oceanic Fluid Dynamics*, 15-19 June 2015, Minneapolis, MN.
- Soloviev, A., Dean, C., 2018: Evaluation of Magnetic Field Variations Induced by Submesoscale Processes in the Shallow Water Ocean Environment. *Paper presented at OCEANS 2018*, 22-25 October 2015, Charleston, SC.
- Soloviev, A.V., Dean, C.W., Avera, W., 2015a: Magnetic signatures of fine-scale processes in the ocean surface layer. *Oral presentation*. American Geophysical Union Fall meeting, 14-18 December San Francisco, CA.

- Soloviev, A.V., Dean, C.W., Lukas, R., Terray, E., Spatially-coherent organized motion in the upper ocean turbulent boundary layer: Langmuir circulation and ramp-like structures. Manuscript for submission.
- Soloviev, A.V., Lukas, R., 1997: Sharp frontal interfaces in near-surface layer of the ocean in the western equatorial Pacific warm pool. *Journal of Physical Oceanography* 27, 999-1017.
- Soloveiv, A., Lukas, R., 2014: *The Near-Surface Layer of the Ocean: Structure, Dynamics, and Applications. Second Edition.* Springer. 552 p.
- Soloviev, A., Matt, S., Avera, W. 2013: Analysis of the electromagnetic signatures of fine-scale oceanographic features, *Proceedings of MARELEC 2013*, 16–19 July, Hamburg, Germany.
- Soloviev, A.V., Matt, S., Fujimura, A., 2015b: Three-dimensional dynamics of fresh water lenses in the ocean’s near-surface layer. *Oceanography* 28, 142-149.
- Stich, H.-B., Lampert, W., 1981: Predator evasion as an explanation of diurnal vertical migration by zooplankton. *Nature* 293, 396-398.
- Sullivan, P.P., McWilliams, J.C., Melville, W.K., 2007: Surface gravity wave effects in the oceanic boundary layer: large-eddy simulation with vortex force and stochastic breakers. *Journal of Fluid Mechanics* 593, 405-452.
- Terray, E.A., Drennan, W.M., Donelan, M.A., 1999: The vertical structure of shear and dissipation in the ocean surface layer. In: M.L. Banner (ed.) *The Wind-Driven Air-Sea Interface*, School of Mathematics, University of New South Wales, Sydney, Australia, 1999, ISBN 0 7334 0586, pp 239-245
- Terray, E.A., Williams III, A.J., Brumley, B.H., unpublished manuscript: Observation of shear-free turbulence beneath whitecaps in the marine surface layer. 26 pp
- Thorpe, S.A., 1985: Small-scale processes in the upper ocean boundary layer. *Nature* 318, 519-522.
- Thorpe, S.A., Hall, A.J., 1987: Bubble clouds and temperature anomalies in the upper ocean. *Nature* 328, 48–51.
- Thorpe, S.A., Jackson, J.F.E., Hall, A.J., Lueck, R.G., 2003: Measurements of turbulence in the upper ocean mixing layer using Autosub. *Journal of Physical Oceanography* 33, 122–145.
- United States Coast Guard (USCG), 2008: Environmental impact statement for the Calypso LNG Deepwater Port license application. Volumes 1 and 2. 1657.
- Visser, A.W., 2007: Biomixing of the oceans? *Science* 316, 838-839.



- Warburton, F., Caminiti, R., 1964: The induced magnetic field of sea waves. *Journal of Geophysical Research* 69, 4293-4309.
- Weaver, J.T., 1965: Magnetic variations associated with ocean waves and swell. *Journal of Geophysical Research* 70, 1921-1929.
- White, B.L., Neph, H.M., 2003: Scalar transport in random cylinder arrays at moderate Reynolds number. *Journal of Fluid Mechanics* 487, 43-79.
- Wijesekera, H.W, Paulsom, C.A., Huyer, A. 1999: The effect of rainfall on the sea surface layer during a westerly wind burst in the western equatorial Pacific. *Journal of Physical Oceanography* 29, 612–632.
- Wilhelmus, M.M., Dabiri, J.O., 2014: Observations of large-scale fluid transport by laser-guided plankton aggregations. *Physics of Fluids* 26, 101312.
- Youngs, D. L., 1982: Time-dependent multi-material flow with large fluid distortion, in *Numerical Methods for Fluid Dynamics*, edited by K. W. Morton and M. J. Baines, pp. 273–285, Academic, N. Y.

## Appendix

Smagin et al. (2014) have shown that the effect of self-inductance can increase the magnetic signature of internal waves. In Smagin's analytical model, the vertical component of the amplitude of the magnetic field  $B_{0z}$  in the upper layer of the ocean (above the internal wave) is governed by the following equation:

$$B_{0z}'' - \kappa_{21}^2 B_{0z} = D_{11} \cosh kz + D_{12} \sinh kz \quad (\text{A1})$$

where  $\kappa_{21}^2 = k^2 + i\mu_0\sigma_{21}\omega$ ,  $D_{11} = -\mu_0\sigma_{21}k^2 A \left( F_z + i \frac{\omega^2}{gk} F_x \right)$ , and

$$D_{12} = \mu_0\sigma_{21}k^2 A \left( \frac{\omega^2}{gk} F_z + iF_x \right).$$

In the lower layer of the ocean,  $B_{0z}$  is governed by

$$B_{0z}'' - \kappa_{22}^2 B_{0z} = D_{21} \cosh k(D-z) + D_{22} \sinh k(D-z) \quad (\text{A2})$$

where  $\kappa_{22}^2 = k^2 + i\mu_0\sigma_{22}\omega$ ,  $D_{21} = i\mu_0\sigma_{22}k^2 A \frac{\sinh kd - \frac{\omega^2}{gk} \cosh kd}{\sinh k(D-d)} iF_x$ , and

$$D_{22} = \mu_0\sigma_{22}k^2 A \frac{\sinh kd - \omega^2 \cosh kd}{\sinh k(D-d)} iF_x.$$

The solution to these equations in all four layers (air, seafloor, and two seawater layers) is as follows:

$$B_{0z}(z) = \begin{cases} G_1 e^{kz}, & z < 0 \\ G_1 \left( \cosh \kappa_{21} z + \frac{k}{\kappa_{21}} \sinh \kappa_{21} z \right) + N(z), & d > z > 0 \\ G_3 \left( \cosh \kappa_{22} (D-z) + \frac{\kappa_3}{\mu \kappa_{22}} (D-z) \right) + M(z), & D > z > d \\ G_3 e^{\kappa_3(D-z)}, & z > D \end{cases} \quad (\text{A3})$$

$$\text{where } N(z) = S_{11} (\cosh kz - \cosh \kappa_{21} z) + S_{12} \left( \sinh kz - \frac{k}{\kappa_{21}} \sinh \kappa_{21} z \right),$$

$$M(z) = S_{21} (\cosh k(D-z) - \cosh \kappa_{22}(D-z)) + S_{22} \left( \sinh k(D-z) - \frac{k}{\kappa_{22}} \sinh \kappa_{22}(D-z) \right)$$

$$, S_{11} = -i \frac{k^2 A}{\omega} \left( F_z + i \frac{\omega^2}{gk} F_x \right), \quad S_{12} = \frac{k^2 A}{\omega} \left( \frac{\omega^2}{gk} F_z + i F_x \right),$$

$$S_{21} = i \frac{k^2 A}{\omega} \frac{\sinh kd - \frac{\omega^2}{gk} \cosh kd}{\sinh k(D-d)} F_z, \quad S_{22} = -\frac{k^2 A}{\omega} \frac{\sinh kd - \frac{\omega^2}{gk} \cosh kd}{\sinh k(D-d)} F_x, \quad A = -\frac{iag}{\omega},$$

$$\kappa_3 = k^2 + i\mu_0\sigma_3\omega, \text{ and } \delta = D-d$$

G1 and G3 are found from the conditions at the boundaries between the water layers as follows:

$$\begin{pmatrix} \cosh \kappa_{21} d + \frac{k}{\kappa_{21}} \sinh \kappa_{21} & -\cosh \kappa_{22} \delta - \frac{\kappa_3}{\mu \kappa_{22}} \sinh \kappa_{22} \delta \\ \kappa_{21} \sinh \kappa_{21} d + k \cosh \kappa_{21} d & \kappa_{22} \left( \sinh \kappa_{21} \delta + \frac{\kappa_3}{\mu} \cosh \kappa_{22} \delta \right) \end{pmatrix} \begin{pmatrix} G_1 \\ G_3 \end{pmatrix} = \begin{pmatrix} M(d) - N(d) \\ M'(d) - N'(d) \end{pmatrix}.$$

(A4)